



Research on Engineering Structures & Materials

Volume 6 Issue 3 September 2020 P-ISSN: 2148-9807 E-ISSN: 2149-4088

J

R

E

S

M

www.jresm.org



Research Group

The International Journal of **Research on Engineering Structures and Materials (RESM)** is a peer-reviewed open access journal (p-ISSN: 2148-9807; o-ISSN: 2149-4088) published by MIM Research Group. It is published in February, June, September, and December.

The main objective of RESM is to provide an International academic platform for researchers to share scientific results related to all aspects of mechanical, civil and material engineering areas.

RESM aims the publication of original research articles, reviews, short communications technical reports, and letters to the editor on the latest developments in the related fields.

All expenditures for the publication of the manuscripts are most kindly reimbursed by *MIM Research Group*. Thus, authors do not need to pay for publishing their studies in the journal.

The scope of the journal covers (but not limited to) behavior of structures, machines and mechanical systems, vibration, impact loadings and structural dynamics, mechanics of materials (elasticity, plasticity, fracture mechanics), material science (structure and properties of concrete, metals, ceramics, composites, plastics, wood, etc.), nano-materials performances of new and existing buildings and other structural systems, design of buildings and other structural systems, seismic behavior of buildings and other structural systems, repair and strengthening of structural systems, case studies and failure of structural systems, safety and reliability in structural and material engineering, use of new and innovative materials and techniques in energy systems and mechanical aspects of biological systems (biomechanics and biomimetics).

The topics covered in RESM include:

- Structural Engineering
- Mechanical Engineering
- Material Engineering
- Earthquake Engineering
- Nano-technology
- Energy Systems
- Biomechanics and Biomimetics

Abstracting and Indexing

Please visit <http://www.jresm.org> for more information.

Graphics and Design

H. Ersen Balcioglu

ersen.balcioglu@usak.edu.tr

Yunus Demirtas

yunus.demirtas@usak.edu.tr



**RESEARCH on
ENGINEERING STRUCTURES &
MATERIALS**



Published by MIM Research Group

RESEARCH on ENGINEERING STRUCTURES & MATERIALS

Editors in This Issue

Editor in Chief		
Hayri Baytan Özmen	Usak University	Turkey
<hr/>		
Editor (Energy, Thermodynamics)		
Canan Kandilli	Usak University	Turkey
<hr/>		
Editor (Mechanics, Materials)		
H. Ersen Balcioğlu	Usak University	Turkey
<hr/>		
Editor (Structural Eng., Mechanics, Applied Math.)		
Tanmoy Mukhopadhyay	Oxford University	United Kingdom
<hr/>		
Editor (Mechanics, Biosystems, Meta-materials)		
Alp Karakoç	Aalto University	Finland
<hr/>		

Editorial Office

Publishing Manager & Copyeditor		
H. Ersen Balcioğlu	Usak University	Turkey
<hr/>		
Publishing Assistant		
Yunus Demirtaş	Usak University	Turkey
<hr/>		

Editorial Board Members

Farid Abed-Meraim	Arts et Metiers ParisTech	France
P. Anbazhagan	Indian Institute of Science	India
Raffaele Barretta	University of Naples Federico II	Italy
R.S. Beniwal	Council of Scientific and Industrial Research	India
Antonio Caggiano	University of Buenos Aires	Argentina
Noel Challamel	University of South Brittany	France
Abdulkadir Çevik	Gaziantep University	Turkey
J. Paulo Davim	University of Aveiro	Portugal
Hom Nath Dhakal	University of Portsmouth	UK
S. Amir M. Ghannadpour	Shahid Beheshti University	Iran
Ali Goodarzi	Harvard University	USA
Jian Jiang	National Institute of Standards and Technology	USA
Ramazan Karakuzu	Dokuz Eylül University	Turkey
Arkadiusz Kwiecien	Cracow University of Technology	Poland
Stefano Lenci	Universita Politecnica delle Marche	Italy
Yuan Meini	North University of China	China
Stergios A. Mitoulis	University of Surrey	UK
Alaa M. Rashad	Shaqra University	Saudi Arabia
Mohammad Mehdi Rashidi	University of Tongji	China
Pier Paolo Rossi	University of Catania	Italy
Neritan Shkodrani	Polythecnic University of Tirana	Albania
Faris Tarlochan	Qatar University	Qatar
Y.B. Yang	National Taiwan University	Taiwan

Advisory Board Members

Yinusa Amoo Ahmed	University of Lagos	Nigeria
Sevim Alışır	Ondokuz Mayıs University	Turkey
Mustafa Yasin Aslan	Usak University	Turkey
Huseyin Ersen Balcioglu	Usak University	Turkey
Beyhan Bayhan	Bursa Technical University	Turkey
Hektor Cullufi	Polytechnic University of Tirana	Albania
Preeta Datta	North Carolina State University	USA
J. Paulo Davim	University of Aveiro	Portugal
Akar Dogan	Munzur University	Turkey
Hany El-Hamshary	Tanta University	Egypt
Dulce Franco Henriques	Instituto Politécnico de Lisboa	Portugal
Halit Levent Hosgun	Bursa Technical University	Turkey
Ercan Isik	Bitlis Eren University	Turkey
Charles Langston	University of Memphis	USA
Ahmet Meram	KTO Karatay University	Turkey
Masoomeh Mirrashid	Semnan University	Iran
Mehmet Palanci	Istanbul Arel University	Turkey
Alaa M. Rashad	Building Materials Research and Quality Control Institute	Egypt
Fabio Rizzo	University of Chieti-Pescara	Italy
Behnam Rosti	Shiraz University of Technology	Iran
Tamer Saracyakupoglu	Istanbul Gelisim University	Turkey
Rudimylla Septimio Azeredo	Federal University of Southern and Southeastern Pará	Brazil
Anand B. Tapase	Karmaveer Bhaurao Patil College of Engineering	India
Hamide Tekeli	Süleyman Demirel University	Turkey
Onder Yesil	Usak University	Turkey

Advisory Board Members

Ferhat Yıldırım

Çanakkale Onsekiz Mart University

Turkey

In This Issue

Research Article

197 **Melik Ziya Yakut, Sinem Esen**

Impact of energy efficient design parameters on energy consumption in hot-humid climate zones

Research Article

207 **Adeshina Adegoke, Akin Fashanu, Olayinka Adewumi, Ayowole Oyediran**

Nonlinear vibrations of a cantilevered pipe conveying pulsating two phase flow

Research Article

229 **Hayri Baytan Ozmen, Mehmet Inel, Yunus Demirtas**

Evaluation of different cases of soft story formation for mid-rise RC buildings

Research Article

241 **Behçet Dündar, Emriye Çınar, Ahmet Necip Çalışkan**

An investigation of high temperature effect on pumice aggregate light mortars with brick flour

Research Article

257 **Fatoş Koç, Selay Sert Çok, Nilay Gizli**

Tuning the properties of silica aerogels through pH controlled sol-gel processes

Research Article

271 **Ferhat Yıldırım, Mustafa Aydın, Hakan Yetgin**

Tribological properties of PPS/PA46 polymer blends

Technical Note

283 **Ekrem Altuncu, Recep Akyüz**

Applicability investigation of alumina-titania based plasma spray coating on cast iron brake discs for battery electric vehicles

Free access to tables of content, abstracts and full text of papers for web visitors.

Copyright © 2020

Research on Engineering Structures & Materials

MIM Research Group Publications

ISSN 2148-9807

<http://www.jresm.org>

ABSTRACTING / INDEXING

The international journal of Research on Engineering Structures and Materials (RESM) is currently Abstracted/Indexed by CrossRef, Google Scholar, Universal Impact Factor, Scientific Indexing Service, Research Bible, CiteFactor, Electronic Journal Library, Open Academic Journals Index, Global Impact Factor, Directory of Research Journals Indexing, Root Society for Indexing and Impact Factor Service, Cosmos, Materials Science & Engineering Database (ProQuest) Engineering Journals (ProQuest), ULAKBİM TR Index (TUBITAK), International Institute of Organized Research (I2OR), International Scientific Indexing (ISI), Publication Forum, Asos Index and under evaluation by many other respected indexes.

Check web site for current indexing info.





Research Article

Impact of energy efficient design parameters on energy consumption in hot-humid climate zones

Melik Ziya Yakut^{*1,a}, Sinem Esen^{2,b}

¹Department of Mechatronics Engineering, Isparta University of Applied Sciences, Isparta, Turkey

²Department of Energy Systems Engineering, Isparta University of Applied Sciences, Isparta, Turkey

Article Info

Article history:

Received 28 Sep 2019

Revised 23 Jan 2020

Accepted 25 Feb 2020

Keywords:

Energy efficient building;

Energy efficient building design parameters;

BIM; BEM

Abstract

In this study; based on energy-efficient design parameters, the effects of building design parameters on the energy consumption of the building were examined. Accordingly, a reference building has been created as an example of application in the hot-humid climate zone. In the process of modelling the building, BIM (Building Information Modelling) software Autodesk Revit was used. The model has been transferred to Green Building Studio (GBS) for energy performance analysis and evaluation of design alternatives. The parameters evaluated in terms of energy consumption of the building were selected from among the design alternatives produced by GBS, based on energy-efficient design parameters. As a result of the energy performance analysis of the reference building via GBS, the building's annual electricity consumption is 35,137 kWh and the annual fuel consumption is 93,729 MJ. Based on the evaluation of selected design parameters as a result of reference building energy performance analysis; HVAC systems have been found to have the most impact on energy consumption (rates of changes; 36.83% in annual electricity consumption, 90.27% in annual fuel consumption). HVAC systems, selected to be highly efficient and suitable for climate type, have the potential to save significant energy in the amount of energy consumption throughout the life cycle. In addition to this, as of the early design phase, the energy efficient design of the building is of great importance in terms of a holistic evaluation and maximum energy efficiency.

© 2020 MIM Research Group. All rights reserved.

1. Introduction

Today, the growth in energy consumption has spread to all the main sectors of the economy and three quarters of the increase in energy demand is composed of industry and buildings. The building sector consumes 29% of the world's energy consumption [1]. The building sector, which has a substantial share in the increasing energy demand, uses a large rate of the total energy consumed as in the whole world in our country to provide user comfort in buildings. In the building sector, widespread use of energy efficient building design approach and renewable energy resource use is one of the most important issues. Unlike cars or electrical appliances -where the next generation can be more energy efficient than the previous one- buildings have decades of life [2]. For this purpose, the energy analysis process is being included in the design process with increasing regulations in the world. With the energy efficient design criteria to be implemented and the building standards aimed at increasing efficiency, the energy consumption of buildings can be reduced to low levels.

*Corresponding author: ziyayakut@isparta.edu.tr

^a orcid.org/0000-0003-4120-6016; ^b orcid.org/0000-0001-9725-977X

DOI: <http://dx.doi.org/10.17515/resm2019.156ic2809>

Res. Eng. Struct. Mat. Vol. 6 Iss. 3 (2020) 197-206

Energy efficient building design aims to reduce the carbon dioxide emission and provide energy saving by adapting the building to nature with passive strategies and supporting it with renewable energy sources. Energy efficiency building design can be achieved in two stages:

- Minimization of energy consumption rates by optimal application of energy efficient building design parameters,
- Integration of passive and active systems to increase the energy gain to the building.

In order to provide energy efficiency in buildings, the design should be made in a way that is compatible with local climate and geography. While the analysis in building designs is compatible with local environmental conditions, it is possible to use energy effectively with local material selection and passive and active systems integrated into the building. To achieve this goal, design parameters and energy-efficient analysis must be correctly determined. When these analyses are included in the design in the early design phase, energy savings are provided more and implementation costs are reduced to smaller amounts compared to the way they were involved in the later phases of the process.

Remain incapable of computer-aided design tools in some cases have led designers to choose BIM (Building Information Modelling) as an appropriate tool for integrating sustainability in the building sector as a holistic solution into their existing workflows [3]. BIM is specifically designed to support the application of energy analysis to identify possible energy gain or loss for the building, to demonstrate and predict their sustainability during the conceptual design phase [4]. BIM consists of the production and management process of all information corresponding to the building throughout the lifecycle, including the design and implementation phase. BIM software can increase the availability of whole building energy calculation through standard processes and parameters [5]. Among the benefits of incorporating design into the BIM process have included the following:

- To facilitate interdisciplinary (architect, engineer, designer, et al.) integrated work
- The ability to demonstrate the energy consumption trend of the building throughout its life cycle through energy performance analysis,
- Among the alternatives created based on energy performance analysis, the ability to identify alternatives and improvements that can keep the amount of energy consumption to a minimum throughout the lifecycle from the early design stage,
- The ability to easily create optimum design combinations in terms of energy efficiency and to make more effective decisions in the design process.

Through the software, many design alternatives and optimum combinations can be easily created to minimize the amount of energy consumption. The significance of BIM is to integrate the design process and the architectural life cycle of several information. Currently, model data of REVIT and other BIM software have been exported to various analysis software in GBXML format [6].

Another feature of BIM, BEM (Building Energy Modelling), integrates energy analysis with the design, construction, use and maintenance processes of buildings. This program, which deals with the building with a holistic approach, shows the user with quantitative data how effectively the designed building can use energy [7]. However, BEM has not yet fully benefited from the perpetual flow of information in digital modelling. For example, BEM-related information must be manually re-entered into these tools, but this information has already been entered in BIM models [8]. Green Building Studio (GBS) is a web-based software that uses the DOE-2 engine for energy simulation, providing information on a building's energy consumption, carbon footprint, water consumption, material costs and matter such as. Green Building Studio can perform 3D modelling of building design states that affect energy simulation results [9].

Regarding the studies on the subject; the study of Abanda and Byers (2016) [10] has assessed the impact of orientation on energy consumption in small-scale structures and is evaluated how BIM can be used to simplify this process. In the GBS, different building orientations are tackled and the effects of all building energy are enquired. By virtue of an analysis of the energy consumption corresponding to different orientations, they observed that a well-guided structure could provide considerable energy savings over the life cycle. The aim of Kim et al. (2016) [11] is to perform energy analysis with a case study on a residence. With Autodesk Revit, BIMs are created for each scenario, and Green Building Studio is used to calculate the total energy load. The results are shown that if the windows are positioned at medium height in all directions, the building provides the minimum energy load and the positioning of the east window provides the maximum total energy load.

The study of Sorgato et al. (2016) [12] is to evaluate the effectiveness of window opening, ventilation control and building heat mass on energy consumption connected to the HVAC (Heating, Ventilation, and Air Conditioning) system in residences in Brazil. The results show that low thermal permeability and medium thermal capacity, energy consumption in cooling has decreased by 32%. Mujeebu et al. (2016) [13] has presented a simulation study on the energy performance of a prototype office building in Saudi Arabia by changing the conventional polystyrene insulation and double-glazing with nano VIP (Vacuum Insulating Coating) and nano aerogel glazing. The building model was created in Autodesk Revit and the energy simulation was built by ECOTECH using Dhahran's weather data. The results show that nano VIP on the walls and roofs and nanogel windows together can maintain approximately 18% of the building's yearly energy consumption. Buratti et al. (2017) [14] is interested in the potential of high energy saving windows with a granular silica aerogel to save energy in building renovations. Glass systems were examined taking account of two types of granular silica aerogel and several glass layers. Compared to traditional windows, 63% reduction in U-value and a 30% reduction in light transmittance were achieved.

Chel and Kaushik (2017) [15] present solutions and recommendations on renewable energy technologies and energy efficient building development for sustainability. Firstly, they pointed out that proper design of daylight would result in a great reduction in the use of artificial lights while daylight hours, thus reducing energy consumption for lighting. The second is to use low embodied energy building materials for building construction. Third, it's relevant operational energy savings by using energy-efficient equipment in the building. The latter relates to the use of added renewable systems for hot water heating, solar PV electrification and the like. Sahin Çağlı (2018) [16] worked on improving the design of two multi-storey housing projects with dynamic energy simulation and achieving energy efficiency in the hot climate zone of Adana. According to the environmental building shading calculations, the cooling load was reduced from 95.000 kWh to 78.751 kWh, with an energy saving of approximately 17%, with orientation, selection of optimal building components and insulation materials, and minimization of transparent areas. Gonzalo et al. (2019) [17], in their work, intended to develop an effective and repeatable testing method to assess the impact of various on the energy performance and comfort requirements of buildings. After removing all geometric and spatial information of the building from the BIM model, an energy simulation was made using Energy Plus. They found that controlling the natural ventilation ratio could help to decrease 45% of heating and cooling energy consumption in winter.

The aim of this study is to examine the effects of building design parameters determined starting from energy-efficient design parameters on the energy consumption of the building. In this way, the design parameters that prominent in minimizing the energy consumption of the building will be revealed. Distinctly from the literature studies examined in this study, It is aimed to evaluate the design parameters that are thought to

affect the energy performance in GBS, which is the BEM software which stands out day by day in the energy performance analysis. In this way, it will be specified how GBS handles the energy performance analysis process. At the same time, it is the study of the effects of the specified parameters on energy consumption through GBS. In addition to this, the importance of designing the building with an energy efficient design approach from the early design stage will be emphasized.

2. Methodology

Energy-efficient design parameters are divided into three parameters for the user, the external environment and the building. Energy-efficient systems are divided into passive and active systems. Accordingly, a reference building was established as an example of application in the hot-humid climate zone so as to demonstrate the effect of energy-efficient design parameters on energy consumption. The reference building was designed to meet a building's energy requirements at a minimum in terms of the type of climate in which it is located. The parameters considered when creating the reference building are shown in Figure 1.

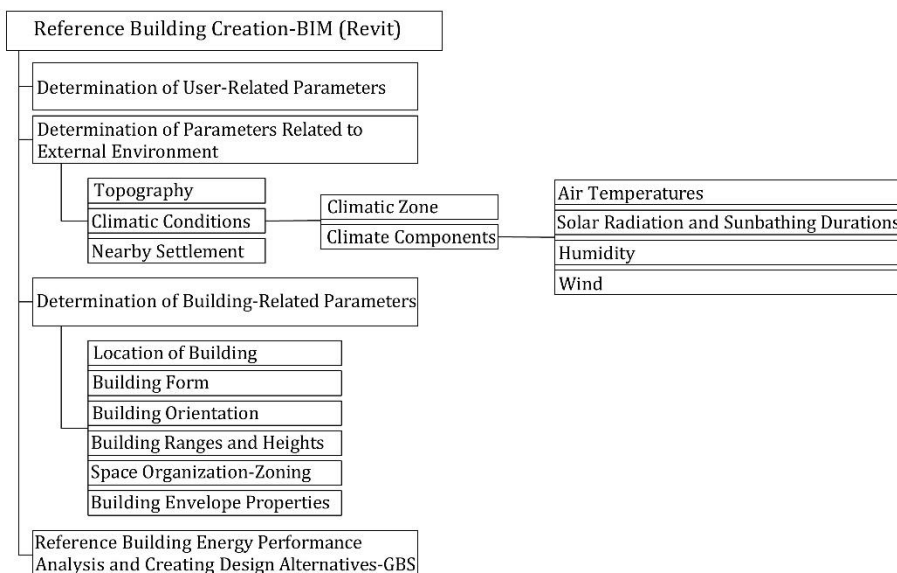


Fig. 1 The flow chart of the creation of the reference building

The reference building is located in a hypothetical topography in Antalya province, which is in the hot-humid climate zone. In this type of climate, the consumption of cooling energy is more important than the consumption of heating energy. It was acted on by accepting that the building, which was located in a field exposed to intense solar radiation throughout the year, was not shaded by other buildings or obstacles. Project details and monthly temperature chart are shown in Figure 2.

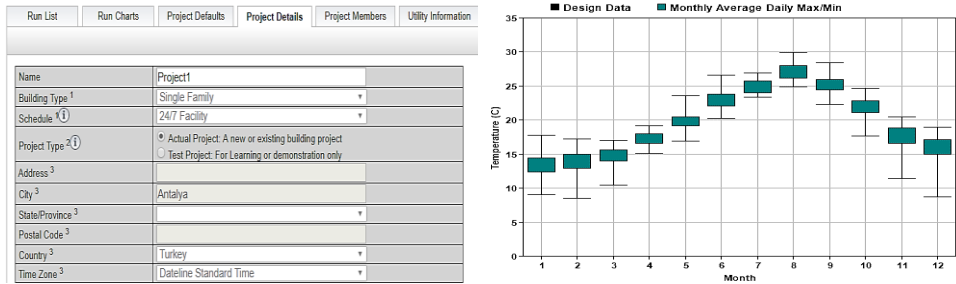


Fig. 2 Project details and monthly temperature chart

The building is located on the top of the land in order to provide maximum benefit from wind effects, reduce the negative effects of humidity and provide sun protection for hot-humid climate type. It is designed as a detached house with a ground floor and a normal floor. The building form is designed in a rectangular form with low depth and long facades to get maximum benefit from the prevailing wind. At the same time, the long facade and living areas of the building are directed to the north (Fig. 3).

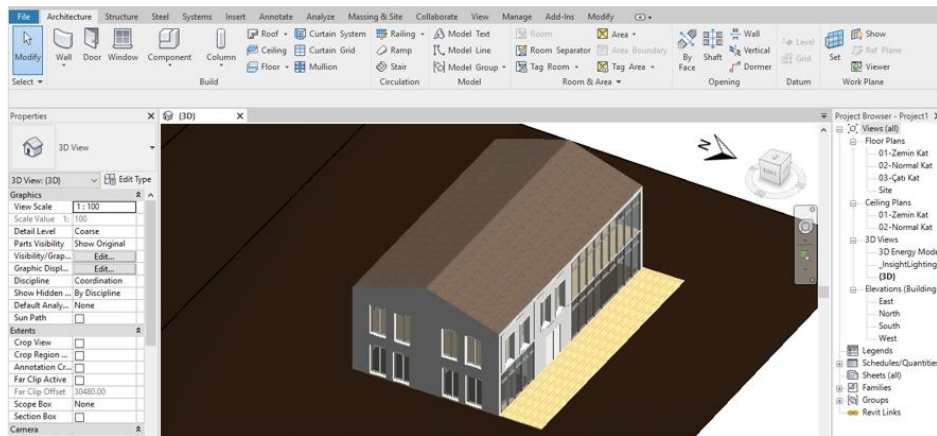


Fig. 3 3D view of the reference building in Revit

The reference building heating system is central hot water system and fuel type natural gas, cooling system is determined as split air conditioning. The WWR (Window-to-Wall Ratio) in the building is 65% of the north facade, 25% of the south facade, 32% of the eastern facade and 28% of the western facade. When determining the thermophysical properties of the opaque and transparent components of the reference building, the requirements of the hot-humid climate type, were taken into consideration. The U values (heat transfer coefficients) of the reference building envelope components are shown in Table 1.

Table 1. U values of reference building envelope components (W/m²K)

	U Values (W/m ² K)
Exterior Wall	0,47
Roof	0,33
Floor	0,46
Window	2,4

Different alternatives of parameters affecting the energy performance of the building were evaluated. In the process of modelling the building, BIM software Autodesk Revit was used. The model was transferred to GBS for the energy performance analysis and evaluation of design alternatives. GBS is one of Revit's web-based energy modelling software. The parameters evaluated in terms of energy consumption of the building were selected from among the design alternatives produced by GBS based on energy-efficient design parameters. While making these elections, were acted with program restrictions. The selected parameters include the following:

- The orientation of the building
- HVAC systems
- Lighting control
- Roof insulation
- Wall insulation
- WWR, Glass type, Sun control.

3. Results and Discussion

As a result of the energy performance analysis of the reference building through GBS, the building annual electricity consumption is 35,137 kWh and the annual fuel consumption is 93,729 MJ (Fig. 4). GBS via was created different design alternatives that have different effects on energy consumption for the reference building. Fig. 5 is shown part of the interface listing design alternatives created by GBS

Annual CO₂ Emissions	
Electric	0.0 Mg
Onsite Fuel	4.7 Mg
Large SUV Equivalent	0.5 SUVs / Year
Annual Energy	
Energy Use Intensity (EUI)	488 MJ / m ² / year
Electric	35,137 kWh
Fuel	93,729 MJ
Annual Peak Demand	8.2 kW
Lifecycle Energy	
Electric	1,054,104 kWh
Fuel	2,811,885 MJ

Fig. 4 Reference building annual energy performance summary

Project1												Weather Station		
Name	Date	User Name	Floor Area (m ²)	Energy Use Intensity (MJ/m ² /year) (C)	Electric Cost (kWh)	Fuel Cost (MJ)	Total Annual Cost ¹			Total Annual Energy ¹			Carbon Emissions (Mg)	Potential Energy Savings
							Electric	Fuel	Energy	Electric (kWh)	Fuel (MJ)			Compare
Project Default Utility Rates														
Project Default Utility Rates														
Base Run														
Project1	1/12/2019 12:28 AM	snemesenTGU3U	198	1,113.2	\$0.17	\$0.02	\$5,798	\$1,849	\$7,646	35,137	93,729	--	--	
Alternate Run(s) of Project1														
Project_ASHRAE 90.1-2010	1/12/2019 12:30 AM	snemesenTGU3U	198	645.0	\$0.17	\$0.02	\$3,810	\$877	\$4,687	23,091	44,485	--	--	
WWR - Northern Walls_95% - Window Shades - North_No change - Window Glass Types - North_No change	1/12/2019 12:30 AM	snemesenTGU3U	198	1,172.4	\$0.17	\$0.02	\$6,040	\$1,976	\$8,015	36,604	100,175	--	--	
WWR - Northern Walls_95% - Window Shades - North_No change - Window Glass Types - North_Sgl Clr	1/12/2019 12:30 AM	snemesenTGU3U	198	1,217.6	\$0.17	\$0.02	\$5,970	\$2,183	\$8,153	36,181	110,679	--	--	
WWR - Eastern Walls_30% - Window Shades - East_2/3 Win Height - Window Glass Types - East_Trp LoE	1/12/2019 12:30 AM	snemesenTGU3U	198	1,041.0	\$0.17	\$0.02	\$5,388	\$1,744	\$7,131	32,652	88,400	--	--	
WWR - Eastern Walls_0% - Window Shades - East_No change - Window Glass Types - East_No change	1/12/2019 12:30 AM	snemesenTGU3U	198	1,025.3	\$0.17	\$0.02	\$5,294	\$1,722	\$7,017	32,086	87,327	--	--	
Building Orientation (Degrees)_0	1/12/2019 12:30 AM	snemesenTGU3U	198	1,116.5	\$0.17	\$0.02	\$5,809	\$1,857	\$7,666	35,206	94,144	--	--	
Building Orientation (Degrees)_45	1/12/2019 12:30 AM	snemesenTGU3U	198	1,275.5	\$0.17	\$0.02	\$6,471	\$2,192	\$8,663	39,219	111,150	--	--	
Building Orientation (Degrees)_90	1/12/2019 12:30 AM	snemesenTGU3U	198	1,312.4	\$0.17	\$0.02	\$6,636	\$2,265	\$8,901	40,218	114,854	--	--	
Building Orientation (Degrees)_135	1/12/2019 12:30 AM	snemesenTGU3U	198	1,328.1	\$0.17	\$0.02	\$6,716	\$2,292	\$9,008	40,701	116,226	--	--	
Building Orientation (Degrees)_180	1/12/2019 12:30 AM	snemesenTGU3U	198	1,189.1	\$0.17	\$0.02	\$6,289	\$1,933	\$8,223	38,117	98,014	--	--	
Building Orientation (Degrees)_225	1/12/2019 12:30 AM	snemesenTGU3U	198	1,288.9	\$0.17	\$0.02	\$6,764	\$2,118	\$8,883	40,995	107,408	--	--	
Building Orientation (Degrees)_270	1/12/2019 12:30 AM	snemesenTGU3U	198	1,302.3	\$0.17	\$0.02	\$6,705	\$2,196	\$8,901	40,635	111,359	--	--	
Building Orientation (Degrees)_315	1/12/2019 12:30 AM	snemesenTGU3U	198	1,303.6	\$0.17	\$0.02	\$6,527	\$2,278	\$8,805	39,556	115,505	--	--	

Fig. 5 Part of the interface listing design alternatives created by GBS

Numerous alternatives have been created through software for parameters such as the orientation of the building, HVAC systems, lighting control, roof insulation, wall insulation, WWR, glass type, sun control. The software evaluated each parameter within its own possibilities. For example, the effect of 360 degree orientation possibilities on energy performance for the orientation of the building has been revealed through software. Alternatives that affect energy performance to a minimum and maximum based on the possibilities of each determined parameter have been evaluated. The selected parameters and the alternatives of these parameters that minimize and maximize energy consumption are as follows:

- The orientation of the building; for minimum energy consumption “0°”, for maximum energy consumption “120°”
- HVAC systems; for minimum energy consumption “Residential 17 SEER/9.6 HSPF Split HP<5.5 ton”, for maximum energy consumption “VAV, COP 3.5 Low Efficiency Chiller, 65% Eff. Gas Boiler, no economizer”
- Lighting control; for minimum energy consumption “Daylighting Controls”, for maximum energy consumption “No change”
- Roof insulation; for minimum energy consumption “Wood Frame Roof with Insulation”, for maximum energy consumption “Wood Frame Roof without Insulation”
- Wall insulation; for minimum energy consumption “Cavity Wall with Insulation”, for maximum energy consumption “Metal Frame Wall without Insulation”
- WWR, Glass type, Sun control; for minimum energy consumption “WWR-Southern Walls_65%, Window Glass Types-South_Trp L, Window Shades-South_1/3 Win Height”, for maximum energy consumption “WWR-Southern Walls_95%, Window Glass Types-South_Sgl Clr, Window Shades-South_No change”.

As a result of the reference building energy performance analysis, among the design parameters created by GBS, annual minimum and maximum energy consumptions of the selected design parameters according to the method, and the rates of change according to the reference building energy consumption are shown in Table 2.

Table 2. Annual minimum and maximum energy consumption of design parameters in hot-humid climate zone according to method, and rates of change according to reference building energy consumption

Reference Building	Electricity Consumption (kWh)				Fuel Consumption (MJ)			
	35,137				93,729			
	Minimum Consumption				Maximum Consumption			
	Electricity Consumption (kWh)	Rate of Change (%)	Fuel Consumption (MJ)	Rate of Change (%)	Electricity Consumption (kWh)	Rate of Change (%)	Fuel Consumption (MJ)	Rate of Change (%)
The Orientation of the Building	35,137	-	93,729	-	40,972	-16.6	118,104	-26
HVAC Systems	22,195	+36.8	9,114	+90.2	60,001	-70.7	116,633	-24.4
Lighting Control	34,206	+2.6	94,905	-1.2	35,206	-0.2	94,144	-0.4
Roof Insulation	35,137	-	93,729	-	35,350	-0.6	94,250	-0.5
Wall Insulation	35,137	-	93,729	-	36,890	-5	120,808	-28.9
WWR, Glass Type, Sun Control	32,366	7.8	83,831	10.5	48,402	-37.7	132,810	-41.6

The reference building is located in a hot-humid climate zone and the design parameters are selected to provide minimum optimization in a holistic way. Numerous alternatives are created by GBS on parametrical basis, which have close results with the consumption amounts in the table. The minimum consumption amounts in the orientation of the building, roof and wall insulation parameters were provided by the choices made when creating the reference building. Therefore, the rate of change according to the reference building is not given. However, the rates of change in maximum consumption are indicated in the table. In the lighting control parameter, while the minimum electricity consumption is achieved, fuel consumption increases slightly. This is due to a slight increase in fuel use to compensate for the heat lost from lighting equipment as a result of efficient use. The most positive change was in HVAC systems (rates of changes; 36.83% in annual electricity consumption, 90.27% in annual fuel consumption). This was followed by WWR, glass type, solar control parameter (rates of changes; 7.88% in annual electricity consumption, 10.56% in annual fuel consumption). The general characteristic of the parameters in the table, which leads to positive changes in energy consumptions, is that they are highly efficient and climate-appropriate choices. Evaluating parameters with a holistic and energy efficient approach as from the design stage will provide maximum energy savings.

4. Conclusions

In this study, the effects of building design parameters determined based on energy efficient design parameters on energy consumption of the building were examined. Accordingly, the importance of designing the building with an energy efficient design approach from the early design stage is emphasized. The parameters that were evaluated in terms of energy consumption of the building were selected among the design alternatives produced by GBS based on energy efficient design parameters. The selection process was carried out in compliance with program constraints. The design parameters selected as a result of the reference building energy performance analysis were evaluated (annual electricity consumption 35,137 kWh, annual fuel consumption 93,729 MJ). The results of the study include the following:

- In this respect, it is determined that HVAC systems have the most effect on energy consumption (rates of changes; 36.83% in annual electricity consumption, 90.27% in annual fuel consumption). This is due to the fact that HVAC systems are selected high efficiency and suitable for climate type.
- It is emphasized that energy-efficient choices have the potential to save significant energy in the amount of energy consumption throughout the life cycle.
- In addition to this, from the early design stage, it has been observed that the holistic energy-efficient design of the building is of great importance in terms of maximum energy efficiency.
- It has experienced that the inclusion of BIM in the design process shortens the energy performance analysis process, which requires considerable effort. Through the software, many design alternatives and optimum combinations can be easily created to minimize the amount of energy consumption.

Considering that the growing energy needs in the face of the rapidly growing world population and sectoral structures are still primarily supplied by fossil fuels, the importance of these solution methods is increasing. At the same time, there is depletion of fuel reserves in the near future, and their use as energy source is increasing the emission values of greenhouse gases such as CO₂ in the atmosphere, resulting in global warming and climate change. For these reasons, the construction sector, which has a large share in global energy consumption, should adopt an energy efficient design approach from the early design stage. Furthermore, the use of renewable energy sources should be taken into account in the design. The researches and developments on this subject will contribute to the increase of knowledge on the subject.

References

- [1] BP Energy. BP Energy Outlook 2019 Edition, 29, 2019.
- [2] Turk Ž, Klinc R, Ma Z. Towards a Parsimonious Information Management for Energy Retrofitting of Buildings. Proceedings of the Creative Construction Conference, Budapest, Hungary, 490 - 495, 2019. <https://doi.org/10.3311/CCC2019-067>
- [3] Khoshdelnezamiha G, Liew SC, Bong VNS, Ong DEL. BIM-based Approach for Green Buildings in Malaysia. Earth and Environmental Science, 2018;268(2019):1-8. <https://doi.org/10.1088/1755-1315/268/1/012052>
- [4] Ebrahim A, Wayal AS, Cook M. BIM Based Building Performance Analysis Of A Green Office Building. International Journal Of Scientific & Technology Research, 2019;8(08):566-573.
- [5] Lu Y, Wu Z, Chang R, Li Y. Building Information Modeling (BIM) for green buildings: A critical review and future directions. Automation in Construction, 2017;83(2017):134-148. <https://doi.org/10.1016/j.autcon.2017.08.024>

- [6] Xu G, He Y. Research on Decoration Design of Green Building Based on BIM Technology. *Earth and Environmental Science*, 2019;242(2019):1-7. <https://doi.org/10.1088/1755-1315/242/6/062073>
- [7] Gerrish K, Ruikar K, Cook M. Using BIM Capabilities to Improve Existing Building Energy Modelling Practices. *Engineering, Construction and Architectural Management*, 2017;24(2):190-208. <https://doi.org/10.1108/ECAM-11-2015-0181>
- [8] Gao H, Koch C, Yupeng W. Building information modelling based building energy modelling: A review. *Applied Energy*, 2019;238(2019):320-343. <https://doi.org/10.1016/j.apenergy.2019.01.032>
- [9] Kim JU, Hadadi OA, Kim H, Kim J. Development of A BIM-Based Maintenance Decision-Making Framework for the Optimization between Energy Efficiency and Investment Costs. *Sustainability*, 2018;10:1-15. <https://doi.org/10.3390/su10072480>
- [10] Abanda FH, Byers L. An Investigation of the Impact of Building Orientation on Energy Consumption in A Domestic Building Using Emerging BIM(Building Information Modelling). *Energy*, 2016;97:517-527. <https://doi.org/10.1016/j.energy.2015.12.135>
- [11] Kim S, Zadeh PA, Staub-French S, Froese T, Terim Cavka B. Assessment of the Impact of Window Size, Position and Orientation on Building Energy Load Using BIM. *Procedia Engineering*, 2016;145:1424-1431. <https://doi.org/10.1016/j.proeng.2016.04.179>
- [12] Sorgato MJ, Melo AP, Lamberts R. The Effect of Window Opening Ventilation Control on Residential Building Energy Consumption. *Energy and Buildings*, 2016;133:1-13. <https://doi.org/10.1016/j.enbuild.2016.09.059>
- [13] Mujeebu MA, Ashraf N, Alsuwayigh AH. Effect of Nano Vacuum Insulation Panel And Nanogel Glazing on The Energy Performance of Office Building. *Applied Energy*, 2016; 173:141-151. <https://doi.org/10.1016/j.apenergy.2016.04.014>
- [14] Buratti C, Moretti E, Zinzi M. High Energy-Efficient Windows with Silica Aerogel for Building Refurbishment: Experimental Characterization and Preliminary Simulations in Different Climate Conditions. *Buildings*, 2017;7(8):1-12. <https://doi.org/10.3390/buildings7010008>
- [15] Chel A, Kaushik G. Renewable Energy Technologies for Sustainable Development of Energy Efficient Building. *Alexandria Engineering Journal*, 2017:1 - 15.
- [16] Çağlı Şahin Z. Enerji Etkin Bina Tasarımı ve Adana Örneği, PhD Thesis, Çukurova University, Adana, Turkey, 149 - 152, 2018.
- [17] Gonzalo FDA, Ferrandiz JA, Moreno B. Building Energy Modeling by means of BIM Software. A Case Study with Water Flow Glazing. 7th European Conference On Renewable Energy Systems, Madrid, Spain, 1 - 10, 2019.



Research Article

Nonlinear vibrations of a cantilevered pipe conveying pulsating two phase flow

Adeshina Adegoke^{1,a}, Akin Fashanu^{2,b}, Olayinka Adewumi^{1,c}, Ayowole Oyediran^{1,d*}

¹Department of Mechanical Engineering, University of Lagos, Akoka-Yaba, Lagos, Nigeria.

²Department of Systems Engineering, University of Lagos, Akoka-Yaba, Lagos, Nigeria.

Article Info

Article history:

Received 02 Sep 2019

Revised 09 Dec 2019

Accepted 26 Dec 2019

Keywords:

*Nonlinear dynamics;
Transverse vibration;
Pulsating two-phase
flow; Parametric
resonance;
Cantilevered pipe*

Abstract

This work studied the nonlinear transverse vibrations of a cantilevered pipe conveying pulsatile two-phase flow. Internal flow induced parametric resonance is expected because of the time varying velocity of the conveyed fluid. This unsteady behaviour of the conveyed two-phase flow is considered in the governing equation as time dependent individual velocities with the harmonically varying components fluctuating about the constant mean velocities. Method of multiple scales analysis is adopted to study the nonlinear parametric resonance of dynamics of the cantilevered pipe. Contrary to the dynamics of pulsating single-phase flow, the assessment shows that if the frequencies of pulsation of the two phases are close, both can resonate with the pipe's transverse or axial frequencies together and both can also independently resonate with the pipe's transverse or axial frequencies distinctively. For the planar dynamics when only transverse frequencies are resonated, in the absence of internal resonance, numerical results show that the system exhibits softening nonlinear behavior. At post critical flow conditions, the system oscillates between subcritical and supercritical pitchfork bifurcation to simulate the nonlinear Mathieu's equation. However, in the presence of internal resonance, a nonlinear anti-resonance property is developed. Hence, the overall dynamics is quasi-periodic.

© 2020 MIM Research Group. All rights reserved.

1. Introduction

Regardless of a floater concept for a deepwater field development, there is always a need of riser system connecting the floater at surface and subsea facility on the seabed as explained by Ruxin et al [1]. However, these riser systems are known to be of different variants. One of which is the single hybrid riser (SHR) system, a free-standing riser pipe decoupled from the floater with the aid of a flexible jumper. Chung et al [2] shows that the rich dynamics of cantilever pipes can be adopted as a paradigm for demonstrating the complex dynamic characteristics of this type of riser pipes in deep ocean mining.

As a result of barometric effects, thermal effects and the composition of the hydrocarbon compounds, these riser pipes sometimes convey fluid that can be a single phase liquid or a single phase gas or a multiple-phase mixture. It is a known fact that dynamics of multiphase flow are much more complex when compared to that of single-phase flows. A very common multiphase flow is the gas and liquid two phase flow. The flow behaviour of a gas and liquid two phase flow brings about the complex interaction of numerous variables which complicates the engineering of the conduits that conveys them.

* Corresponding author: ayooyediran@hotmail.com

^a orcid.org/0000-0003-0678-7951; ^b orcid.org/0000-0003-0958-1641; ^c orcid.org/0000-0002-3545-6679;

^d orcid.org/0000-0003-3482-9063

DOI: <http://dx.doi.org/10.17515/resm2019.145me0902>

Res. Eng. Struct. Mat. Vol. 6 Iss. 3 (2020) 207-227

The fluid elastic instability of pipes conveying fluid is mainly due to the unstable vibration caused by the fluid flow, when the flow velocity surpasses a critical value and also due to harmonically perturbed fluid flow (Pulsating Flows). Nevertheless, the effect of the dynamics of pipes conveying fluids has been widely studied by many authors, with most of the studies focusing on the linear and nonlinear dynamics of pipes conveying steady flow as seen in [3-7]. However, it was highlighted by Ibrahim [8] that an obvious effect of pulsating fluid flow is that it forces the pipeline into sustained vibrations under parametric resonance conditions. Forlornly, flow conveyed by pipes are rarely steady. Luczko and Czerwinski. [9] explains that components of hydraulic systems such as pumps, hydraulic engines, fast valves opening and closing, timely injection of inhibitors, elbows, orifices, flow through reducers and many other sources of perturbations often generate pulsation of fluid flow.

All the same, the studies on the linear and nonlinear dynamics of pipes conveying pulsating flow cannot be seen as new. Earlier works can be dated back to more than four decades for various end conditions. Ginsberg [10] pioneered the work considering pinned-pinned pipes, then Paidoussis and Issid [11] for cantilevered pipes and Paidoussis and Sundararajan [12] for clamped-clamped pipes. Sequel to these early studies, the nonlinear dynamics of the subject captivated the minds of many curious researchers which resulted to various publications; notable among these, are the works of Semler and Paidoussis [13] on the nonlinear analysis of parametric resonance of a planar fluid-conveying cantilevered pipe using four different methods; Centre manifold theory, perturbation method, finite difference method and Increment harmonic balance method to resolve the equation and also comparing the theoretical results with experiments. Namachchivaya and Tien [14] on the nonlinear behaviour of supported pipes conveying pulsating fluid examined the problem in the vicinity of subharmonic and combination resonance using the method of averaging. Pranda and Kar [15] on the nonlinear dynamics of a pipe conveying pulsating flow with a combination, principal parametric and internal resonance, adopting the method of multiple scale to resolve the transverse vibrations and stability of a hinged-hinged pipe, Liangqiang et al [16] adopted the multiple scale and normal form theory to determine the expressions for the critical bifurcations leading to incipient and secondary bifurcations for the transverse vibration of a hinged-hinged pipe, Oz and Boyaci [17] on the transverse vibrations of tensioned pipes conveying fluid with time-dependent velocity, adopting the method of multiple scale to analytically determine the stability boundaries on the system, also considered the cases of fixed-fixed end and fixed-sliding end conditions with a vanishing flexural stiffness. Oz [18] on the analysis of nonlinear vibrations and stability analysis of tensioned pipe conveying fluid with variable velocity studied the pipe with fixed supports and immovable end conditions with the flexural stiffness neglected. Singh and Mallik [19] used the wave propagation approach to determine the parametric instability regions of a periodically supported pipe conveying fluid. Yoshizawa et al. [20] analytically and experimentally studied the lateral vibration of a flexible clamped-hinged pipe parametrically excited by a fluctuating harmonic internal flow, it was shown that as the amplitude of the pipe deflection grows, the nonlinearity of the fluid force acting on the pipe limits the growth, which results in a steady-state vibration.

On the instability behaviour of pipes conveying multiphase flow, Miwa et al. [21] did a review of the extent of existing work on two-phase flow induced vibrations, stating that there exist very few researches on the instability behaviour of pipes due to internal two-phase flow. Some of the few existing publications on this subject are the works of Monette and Pettigrew [22] which experimentally and theoretically reveals the relationship between the void fraction and the dynamics of the pipe for a two-phase liquid-gas flow. Adegoke and Oyediran [23] showed that the attainment of the critical velocities in the axial and transverse direction are delayed for a cantilever pipe conveying two phase flow

compared to when the pipe is conveying single phase flow. In addition, the critical velocity is observed to be increasing as the void fraction of the two-phase flow increases. Adegoke and Oyediran [24] studied the nonlinear vibrations of top-tensioned cantilevered pipes conveying pressurized steady two-phase flow under thermal loading. The multiple-scale assessment reveals that at some frequencies the system is uncoupled, while at other frequencies a 1:2 coupling exists between the axial and the transverse frequencies of the pipe. Wang et al. [25] adapted the linear equation of transverse motion for single phase flow to account for the two phases and resolved the modified equation using finite element method; experiments were also performed to measure the characteristic parameters of the hydrodynamic slugs and the dynamics response of the pipe. Ortiz-Vidal et al [26] on the theoretical study of the dynamic behaviour of pipes conveying Gas-Liquid flow, also adapted the linear equation of transverse motion for single phase flow to account for the two phases and resolved the modified equation using Galerkin's method for a pipe clamped at both ends.

As seen in the review of literature, most of the existing publications focused on pipes conveying pulsating single phase flow while most of the analytical works on the nonlinear problem did not consider the internal coupling between the axial and the transverse vibrations. Also, some of the publications neglected the flexural stiffness and modelled the pipe as a string with internal fluid flow. On the other hand, recent publications on two phase flow worked on establishing the governing equations and the resolution of the linear dynamics. While the publication on the nonlinear dynamics of pipes conveying two phase flow considered the flow to be steady, neglecting the unsteady velocity term while assuming that the flow exhibits a constant flow mixture velocity. However, to the best of our knowledge, there seems to be some gaps on the study of the nonlinear dynamics of cantilever pipes conveying pulsating two phase fluids. This present study investigates the coupled axial and transverse vibrations of a cantilever pipe conveying pulsating two phase flow. Approximate analytical approach will be used to resolve the governing equations by imposing the method of multiple scales perturbation technique directly to the systems equations (direct-perturbation method).

1. Problem formulation and modeling

In this work, we considered and assumed a system of cantilevered cylindrical pipe of length (L), with cross-sectional area (A), mass per unit length (m), flexural rigidity (EI), and conveying multiphase flow. 1. Plug flow velocity profile. 2. The pipe is modelled as Euler-Bernoulli beam. 3. The motion is planar. 4. Pipe deflections are large, but strains are small. 5. Pipe centerline is extensible.

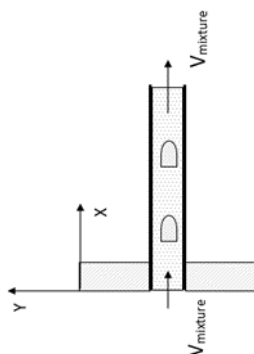


Fig. 1 System's Schematic

1.1. Equation of motion

Adopting the equations of motion of an extensible pipe conveying multi-phase flow as obtained by [24]

$$\begin{aligned} \left(m + \sum_{j=1}^n M_j\right) \ddot{u} + \sum_{j=1}^n M_j \dot{U}_j + \sum_{j=1}^n 2M_j U_j \dot{u}' + \sum_{j=1}^n M_j U_j^2 u'' + \sum_{j=1}^n M_j \dot{U}_j u' - EAu'' \\ - EI(v''''v' + v''v''') + (T_0 - P - EA(\alpha\Delta T) - EA)v'v'' \\ - (T_0 - P - EA(\alpha\Delta T))' + \left(m + \sum_{j=1}^n M_j\right) g = 0, \end{aligned} \tag{1}$$

$$\begin{aligned} \left(m + \sum_{j=1}^n M_j\right) \ddot{v} + \sum_{j=1}^n 2M_j U_j \dot{v}' + \sum_{j=1}^n M_j U_j^2 v'' - \sum_{j=1}^n aM_j U_j^2 v'' + \sum_{j=1}^n M_j \dot{U}_j v' \\ + EIv'''' - (T_0 - P - EA(\alpha\Delta T))v'' \\ - EI(3u''''v'' + 4v''''u'' + 2u'v'''' + v'u'''' + 2v'^2v'''' \\ + 8v'v''v'''' + 2v''^3) \\ + (T_0 - P - EA(\alpha\Delta T) - EA)\left(u'v'' + v'u'' + \frac{3}{2}v'^2v''\right) = 0 \end{aligned} \tag{2}$$

The associated boundary conditions are:

$$v(0) = v'(0), v''(L) = v'''(L) = 0 \text{ and } u(0) = u'(L) = 0 \tag{3}$$

Where x is the longitudinal axis, v is the transverse deflection, u is the axial deflection, n is the number of phases which is 2 in this study. In the fluid, M_j is the mass of the j^{th} phase and U_j is its corresponding speed. m is the mass of the pipe, T_0 is tension, P is the pressure, α is the thermal expansivity term, ΔT relates to the temperature difference and a relates to the Poisson ration (r) as $a=1-2r$.

Using these dimensionless quantities and notations:

$$\begin{aligned} \bar{u} = \frac{u}{L}, \quad \bar{v} = \frac{v}{L}, \quad \bar{t} = \left[\frac{EI}{\sum M_j + m}\right]^{1/2} \frac{t}{L^2}, \quad \bar{U}_j = \left[\frac{M_j}{EI}\right]^{1/2} U_j L, \gamma = \frac{\sum M_j + m}{EI} L^3 g, \\ \Psi_j = \frac{M_j}{\sum M_j}, \Pi_0 = \frac{T_0 L^2}{EI}, \Pi_1 = \frac{EAL^2}{EI}, \Pi_2 = \frac{PL^2}{EI}, \beta_j = \frac{M_j}{\sum M_j + m}, \end{aligned}$$

Notations:

$$\begin{aligned} C11 = \sqrt{\Psi_1}\sqrt{\beta_1}, \quad C12 = \sqrt{\Psi_2}\sqrt{\beta_2}, \quad C21 = 2\sqrt{\Psi_1}\sqrt{\beta_1}, \quad C22 = 2\sqrt{\Psi_2}\sqrt{\beta_2}, \quad C31 = \Psi_1, \\ C32 = \Psi_2, \quad C5 = \Pi_1, \quad C6 = (\Pi_0 - \Pi_2 - \Pi_1(\alpha\Delta T) - \Pi_1), \quad C7 = \Pi_0 - \Pi_2 - \Pi_1(\alpha\Delta T). \end{aligned}$$

The equation is reduced to that of a two-phase flow as:

$$\begin{aligned} \ddot{\bar{u}} + \bar{U}_1 C11 + \bar{U}_2 C12 + \bar{U}_1 C21 \dot{\bar{u}}' + \bar{U}_2 C22 \dot{\bar{u}}' + C31 \bar{U}_1^2 \bar{u}'' + C32 \bar{U}_2^2 \bar{u}'' + \\ \bar{U}_1 C11 \bar{u}' + \bar{U}_2 C12 \bar{u}' - C5 \bar{u}'' - (\bar{v}''''\bar{v}' + \bar{v}''\bar{v}''') + C6 \bar{v}'\bar{v}'' - C7' + \gamma = 0 \end{aligned} \tag{4}$$

$$\ddot{v} + \bar{U}_1 C21 \dot{v}' + \bar{U}_2 C22 \dot{v}' + C31 \bar{U}_1^{-2} \bar{v}'' + C32 \bar{U}_2^{-2} \bar{v}'' - aC31 \bar{U}_1^{-2} \bar{v}'' - aC32 \bar{U}_2^{-2} \bar{v}'' + \bar{U}_1^{-1} C11 \bar{v}' + \bar{U}_2^{-1} C12 \bar{v}' - C8 \bar{v}'' + \bar{v}'''' - (3\bar{u}''' \bar{v}'' + 4\bar{v}''' \bar{u}'' + 2\bar{u}' \bar{v}'''' + \bar{v}' \bar{u}'''' + 2\bar{v}'^2 \bar{v}'''' + 8\bar{v}' \bar{v}'' \bar{v}''' + 2\bar{v}''^3) + C6 (\bar{u}' \bar{v}'' + \bar{v}' \bar{u}'' + \frac{3}{2} \bar{v}'^2 \bar{v}'') = 0 \tag{5}$$

For the purpose of this analysis, two novel driving functions U_1 and U_2 are introduced to pulsate the two phases such that their velocities fluctuate harmonically at frequencies (Ω_1 and Ω_2) about constant mean values (U_{01} and U_{02}). This differs from the steady velocities considered in [24]. Precisely, the driving functions are expressed as;

$$U_1 = U_{01} (1 + \mu_1 \sin(\Omega_1 T_0)) \text{ and } U_2 = U_{02} (1 + \mu_2 \sin(\Omega_2 T_0)) \tag{6}$$

For the two-phase flow, the empirical relationship is obtained by expressing the component's velocities in terms of the superficial velocities as:

$$V_g = U_g v_f, \quad V_l = U_l (1 - v_f) \tag{7}$$

Where U_g and U_l are the superficial flow velocities.

Adopting the Chisholm empirical relations as presented in [27],

Void fraction:

$$v_f = \left[1 + \sqrt{1 - x \left(1 - \frac{\rho_l}{\rho_g} \right) \left(\frac{1-x}{x} \right) \left(\frac{\rho_g}{\rho_l} \right)} \right]^{-1} = \frac{\text{Volume of gas}}{\text{Volume of gas} + \text{Volume of Liquid}} \tag{8}$$

$$\text{Slip Ratio: } S = \frac{V_g}{V_l} = \left[1 - x \left(1 - \frac{\rho_l}{\rho_g} \right) \right]^{1/2} \tag{9}$$

The vapour quality: (x)

The densities of the liquid and gas phases respectively: (ρ_l and ρ_g)

$$\text{Mixture Velocity: } V_T = U_g v_f + U_l (1 - v_f) \tag{10}$$

Individual Velocities:

$$V_l = \frac{V_T}{S+1}, \quad V_g = \frac{S V_T}{S+1} \tag{11}$$

For various void fractions (0.1, 0.3, and 0.5) and a series of mixture velocities, the corresponding slip ratio and individual velocities are estimated and used for calculations.

2. Method of Solution

We seek an approximate solution for \bar{u} and \bar{v} in the form:

$$\bar{u} = \bar{u}_0(T_0, T_1) + \varepsilon \bar{u}_1(T_0, T_1) + \varepsilon^2 \bar{u}_2(T_0, T_1) + O(\varepsilon) \tag{12}$$

$$\bar{v} = \bar{v}_0(T_0, T_1) + \varepsilon \bar{v}_1(T_0, T_1) + \varepsilon^2 \bar{v}_2(T_0, T_1) + O(\varepsilon) \tag{13}$$

For this purpose, two time scales are needed $T_0 = t$ and $T_1 = \varepsilon t$. Where ε is used as a bookkeeping parameter. Perturbing the non-dimensional form of the governing equations and the pulsation of the phases, equations (14, 15 and 16) are realized;

$$\ddot{\bar{u}} + \bar{U}_1^{-1} C11 \dot{\bar{u}} + \bar{U}_2^{-1} C12 \dot{\bar{u}} + \bar{U}_1 C21 \ddot{\bar{u}} + \bar{U}_2 C22 \ddot{\bar{u}} + C31 \bar{U}_1^{-2} \bar{u}'' + C32 \bar{U}_2^{-2} \bar{u}'' + \bar{U}_1^{-1} C11 \bar{u}' + \bar{U}_2^{-1} C12 \bar{u}' - C5 \bar{u}'' + \varepsilon (-\bar{v}'''' \bar{v}' + \bar{v}'' \bar{v}''') + C6 \bar{v}' \bar{v}'' - C7' + \gamma) = 0 \tag{14}$$

$$\begin{aligned} & \ddot{v} + \bar{U}_1 C21 \dot{v}' + \bar{U}_2 C22 \dot{v}' + C31 \bar{U}_1^2 \ddot{v}'' + C32 \bar{U}_2^2 \ddot{v}'' - aC31 \bar{U}_1^2 \ddot{v}'' - \\ & aC32 \bar{U}_2^2 \ddot{v}'' + \bar{U}_1' C11 \dot{v}' + \bar{U}_2' C12 \dot{v}' - C7 \ddot{v}'' + \ddot{v}'''' + \varepsilon \left(-(3\bar{u}'' \ddot{v}'' + 4\ddot{v}'' \bar{u}'' + \right. \\ & 2\bar{u}' \ddot{v}'''' + \ddot{v}' \bar{u}'''' + 2\ddot{v}'^2 \ddot{v}'''' + 8\ddot{v}' \ddot{v}'' \ddot{v}'''' + 2\ddot{v}''^3) + C6 \left(\bar{u}' \ddot{v}'' + \ddot{v}' \bar{u}'' + \right. \\ & \left. \left. \frac{3}{2} \ddot{v}'^2 \ddot{v}'' \right) \right) = 0 \end{aligned} \tag{15}$$

$$\bar{U}_1 = \bar{U}_1 (1 + \varepsilon \mu_1 \sin(\Omega_1 T_0)) \text{ and } \bar{U}_2 = \bar{U}_2 (1 + \varepsilon \mu_2 \sin(\Omega_2 T_0)) \tag{16}$$

Sorting the perturbed equations in orders of (ε), we have:

U-equation:

$$O(\varepsilon^0): D_0^2 \bar{u}_0 + C21 D_0 \bar{u}_0' \bar{U}_1 + C22 D_0 \bar{u}_0'' \bar{U}_2 + C31 \bar{u}_0'' \bar{U}_1^2 + C32 \bar{u}_0'' \bar{U}_2^2 - C5 \bar{u}_0'' = 0 \tag{17}$$

$$\begin{aligned} O(\varepsilon^1): & D_0^2 \bar{u}_1 + C21 D_0 \bar{u}_1' \bar{U}_1 + C22 D_0 \bar{u}_1'' \bar{U}_2 + 2D_0 D_1 \bar{u}_0 + C31 \bar{u}_1'' \bar{U}_1^2 + \\ & C32 \bar{u}_1'' \bar{U}_2^2 + C21 D_0 \bar{u}_1' \bar{U}_1 + C22 D_0 \bar{u}_1'' \bar{U}_2 - C5 \bar{u}_1'' - \bar{v}_0'''' \bar{v}_0' - C7' + \gamma - \\ & \bar{v}_0'' \bar{v}_0'''' + C6 \bar{v}_0' \bar{v}_0'' + C21 D_1 \bar{u}_0' \bar{U}_1 + C22 D_1 \bar{u}_0'' \bar{U}_2 + C11 \Omega_1 \mu_1 \cos(\Omega_1 T_0) \bar{U}_1 + \\ & C12 \Omega_2 \mu_2 \cos(\Omega_2 T_0) \bar{U}_2 + 2C31 \mu_1 \sin(\Omega_1 T_0) \bar{U}_1^2 \bar{u}_0'' + \\ & 2C32 \mu_2 \sin(\Omega_2 T_0) \bar{U}_2^2 \bar{u}_0'' + C21 \mu_1 \sin(\Omega_1 T_0) D_0 \bar{U}_1 \bar{u}_0' + \\ & C22 \mu_2 \sin(\Omega_2 T_0) D_0 \bar{U}_2 \bar{u}_0' + C41 \Omega_1 \mu_1 \cos(\Omega_1 T_0) \bar{U}_1 \bar{u}_0' + \\ & C42 \Omega_2 \mu_2 \cos(\Omega_2 T_0) \bar{U}_2 \bar{u}_0' = 0 \end{aligned} \tag{18}$$

V-equation:

$$O(\varepsilon^0): D_0^2 \bar{v}_0 - C7 \bar{v}_0'' + \bar{v}_0'''' + C21 D_0 \bar{v}_0' \bar{U}_1 + C22 D_0 \bar{v}_0'' \bar{U}_2 + C31 \bar{v}_0'' \bar{U}_1^2 + C32 \bar{v}_0'' \bar{U}_2^2 - aC31 \bar{v}_0'' \bar{U}_1^2 - aC32 \bar{v}_0'' \bar{U}_2^2 = 0 \tag{17}$$

$$\begin{aligned} O(\varepsilon^1): & D_0^2 \bar{v}_1 - C7 \bar{v}_1'' + \bar{v}_1'''' - \bar{u}_0'''' \bar{v}_0' - 2\bar{u}_0' \bar{v}_0'''' - 4\bar{u}_0'' \bar{v}_0'''' - \\ & 3\bar{v}_0'' \bar{v}_0'''' - 2\bar{v}_0'''^2 - 2\bar{v}_0'''' \bar{v}_0' + 2D_0 D_1 \bar{v}_0 + C31 \bar{v}_1'' \bar{U}_1^2 + C32 \bar{v}_1'' \bar{U}_2^2 - \\ & 8\bar{v}_0' \bar{v}_0'' \bar{v}_0'''' + C6 \bar{u}_0' \bar{v}_0'' + C6 \bar{u}_0'' \bar{v}_0' + \frac{3}{2} C6 \bar{v}_0^2 \bar{v}_0'' + C21 D_0 \bar{v}_0' \bar{U}_1 + \\ & C22 D_0 \bar{v}_0'' \bar{U}_2 + C21 D_1 \bar{v}_0' \bar{U}_1 + C22 D_1 \bar{v}_0'' \bar{U}_2 - aC31 \bar{v}_1'' \bar{U}_1^2 - aC32 \bar{v}_1'' \bar{U}_2^2 + \\ & 2C31 \mu_1 \sin(\Omega_1 T_0) \bar{U}_1^2 \bar{v}_0'' + 2C32 \mu_2 \sin(\Omega_2 T_0) \bar{U}_2^2 \bar{v}_0'' + \\ & C21 \mu_1 \sin(\Omega_1 T_0) D_0 \bar{U}_1 \bar{v}_0' + C22 \mu_2 \sin(\Omega_2 T_0) D_0 \bar{U}_2 \bar{v}_0' - \\ & 2aC31 \mu_1 \sin(\Omega_1 T_0) \bar{U}_1^2 \bar{v}_0'' - 2aC32 \mu_2 \sin(\Omega_2 T_0) \bar{U}_2^2 \bar{v}_0'' + \\ & C41 \Omega_1 \mu_1 \cos(\Omega_1 T_0) \bar{U}_1 \bar{v}_0' + C42 \Omega_2 \mu_2 \cos(\Omega_2 T_0) \bar{U}_2 \bar{v}_0' = 0 \end{aligned} \tag{18}$$

The planar natural frequencies and mode shapes can be obtained by solving the leading order equations. The homogeneous solution of the leading order equations (17) and (19) can be expressed as:

$$\bar{u}(x, T_0, T_1)_0 = \phi(x)_n \exp(i\omega_n T_0) + CC \tag{19}$$

$$\bar{v}(x, T_0, T_1)_0 = \eta(x)_n \exp(i\lambda_n T_0) + CC \tag{20}$$

Where (CC) is the complex conjugate, $\phi(x)_n$ and $\eta(x)_n$ are the complex modal functions for the axial and transverse vibrations for each mode (n) and, ω_n and λ_n are the eigenvalues for the axial and transverse vibrations for each mode (n).

3.1 Principal parametric resonance

Substituting the homogeneous solution of the leading order equations into the equations (18) and (20) gives;

$$\begin{aligned}
 & D_0^2 \bar{u}_1 - C5\bar{u}_1'' + C21D_0\bar{u}_1'\bar{U}_1 + C22D_0\bar{u}_1'\bar{U}_2 + C31\bar{u}_1''\bar{U}_1^2 + C32\bar{u}_1''\bar{U}_2^2 = \\
 & - \left(C21 \frac{\partial X(T_1)}{\partial T_1} \frac{\partial \phi(x)}{\partial x} \bar{U}_1 + C22 \frac{\partial X(T_1)}{\partial T_1} \frac{\partial \phi(x)}{\partial x} \bar{U}_2 + 2i \frac{\partial X(T_1)}{\partial T_1} \omega \right) \exp(i\omega T_0) + \\
 & Y(T_1)^2 \left(\frac{\partial \eta(x)}{\partial x} \frac{\partial^4 \eta(x)}{\partial x^4} + \frac{\partial^2 \eta(x)}{\partial x^2} \frac{\partial^3 \eta(x)}{\partial x^3} - C6 \frac{\partial \eta(x)}{\partial x} \frac{\partial^2 \eta(x)}{\partial x^2} \right) \exp(2i\lambda T_0) + \\
 & \left[C32\mu_2 \frac{\partial^2 \phi(x)}{\partial x^2} \exp(i\Omega_2 T_0) \bar{U}_2^2 i - \frac{1}{2} \left(C21\mu_1 \frac{\partial \phi(x)}{\partial x} \exp(-i\Omega_1 T_0) \bar{U}_1 \omega \right) + \right. \\
 & \frac{1}{2} \left(C21\mu_1 \frac{\partial \phi(x)}{\partial x} \exp(i\Omega_1 T_0) \bar{U}_1 \omega \right) - \frac{1}{2} \left(C22\mu_2 \frac{\partial \phi(x)}{\partial x} \exp(-i\Omega_2 T_0) \bar{U}_2 \omega \right) + \\
 & \frac{1}{2} \left(C22\mu_2 \frac{\partial \phi(x)}{\partial x} \exp(i\Omega_2 T_0) \bar{U}_2 \omega \right) - \frac{1}{2} \left(C41\Omega_1\mu_1 \frac{\partial \phi(x)}{\partial x} \exp(-i\Omega_1 T_0) \bar{U}_1 \right) - \\
 & \frac{1}{2} \left(C41\Omega_1\mu_1 \frac{\partial \phi(x)}{\partial x} \exp(i\Omega_1 T_0) \bar{U}_1 \right) - \frac{1}{2} \left(C42\Omega_2\mu_2 \frac{\partial \phi(x)}{\partial x} \exp(-i\Omega_2 T_0) \bar{U}_2 \right) - \\
 & \left. \frac{1}{2} \left(C42\Omega_2\mu_2 \frac{\partial \phi(x)}{\partial x} \exp(i\Omega_2 T_0) \bar{U}_2 \right) - C32\mu_2 \frac{\partial^2 \phi(x)}{\partial x^2} \exp(-i\Omega_2 T_0) \bar{U}_2^2 i - \right. \\
 & \left. C31\mu_1 \frac{\partial^2 \phi(x)}{\partial x^2} \exp(-i\Omega_1 T_0) \bar{U}_1^2 i + C31\mu_1 \frac{\partial^2 \phi(x)}{\partial x^2} \exp(i\Omega_1 T_0) \bar{U}_1^2 i \right] X(T_1) \exp(i\omega T_0) + \\
 & \left[C32\mu_2 \frac{\partial^2 \bar{\phi}(x)}{\partial x^2} \exp(i\Omega_2 T_0) \bar{U}_2^2 i + \frac{1}{2} \left(C21\mu_1 \frac{\partial \bar{\phi}(x)}{\partial x} \exp(i\Omega_1 T_0) \bar{U}_1 \omega \right) + \right. \\
 & \frac{1}{2} \left(C22\mu_2 \frac{\partial \bar{\phi}(x)}{\partial x} \exp(i\Omega_2 T_0) \bar{U}_2 \omega \right) - \frac{1}{2} \left(C41\Omega_1\mu_1 \frac{\partial \bar{\phi}(x)}{\partial x} \exp(i\Omega_1 T_0) \bar{U}_1 \right) - \\
 & \left. \frac{1}{2} \left(C42\Omega_2\mu_2 \frac{\partial \bar{\phi}(x)}{\partial x} \exp(i\Omega_2 T_0) \bar{U}_2 \right) + \right. \\
 & \left. C31\mu_1 \frac{\partial^2 \bar{\phi}(x)}{\partial x^2} \exp(i\Omega_1 T_0) \bar{U}_1^2 i \right] \bar{X}(T_1) \exp(-i\omega T_0) + NST + CC = 0
 \end{aligned} \tag{23}$$

$$\begin{aligned}
 & D_0^2 \bar{v}_1 - C7\bar{v}_1'' + \bar{v}_1'''' + C21D_0\bar{v}_1'\bar{U}_1 + C22D_0\bar{v}_1'\bar{U}_2 + C31\bar{v}_1''\bar{U}_1^2 + \\
 & C32\bar{v}_1''\bar{U}_2^2 - aC31\bar{v}_1''\bar{U}_1^2 - aC32\bar{v}_1''\bar{U}_2^2 = \left(-\frac{\partial Y(T_1)}{\partial T_1} \left(C21 \frac{\partial \eta(x)}{\partial x} \bar{U}_1 + \right. \right. \\
 & C22 \frac{\partial \eta(x)}{\partial x} \bar{U}_2 + 2\eta(x)\lambda i \Big) + 6Y(T_1)^2 \bar{Y}(T_1) \left(\frac{\partial \eta(x)}{\partial x} \right)^2 \frac{\partial \bar{\eta}(x)}{\partial x} + \\
 & 2Y(T_1)^2 \bar{Y}(T_1) \left(\frac{\partial \eta(x)}{\partial x} \right)^2 \frac{\partial^4 \bar{\eta}(x)}{\partial x^4} + 4Y(T_1)^2 \bar{Y}(T_1) \frac{\partial \eta(x)}{\partial x} \frac{\partial \bar{\eta}(x)}{\partial x} \frac{\partial^4 \eta(x)}{\partial x^4} + \\
 & 8Y(T_1)^2 \bar{Y}(T_1) \frac{\partial \eta(x)}{\partial x} \frac{\partial^2 \eta(x)}{\partial x^2} \frac{\partial^3 \eta(x)}{\partial x^3} + 8Y(T_1)^2 \bar{Y}(T_1) \frac{\partial \eta(x)}{\partial x} \frac{\partial^2 \eta(x)}{\partial x^2} \frac{\partial^3 \eta(x)}{\partial x^3} - \\
 & 3C6.Y(T_1)^2 \bar{Y}(T_1) \frac{\partial \eta(x)}{\partial x} \frac{\partial \bar{\eta}(x)}{\partial x} \frac{\partial^2 \eta(x)}{\partial x^2} + 8Y(T_1)^2 \bar{Y}(T_1) \frac{\partial \eta(x)}{\partial x} \frac{\partial^2 \eta(x)}{\partial x^2} \frac{\partial^3 \eta(x)}{\partial x^3} - \\
 & \frac{3}{2} C6.Y(T_1)^2 \bar{Y}(T_1) \left(\frac{\partial \eta(x)}{\partial x} \right)^2 \frac{\partial^2 \eta(x)}{\partial x^2} \Big) \exp(i\lambda T_0) + \left(2X(T_1) \bar{Y}(T_1) \frac{\partial \Phi(x)}{\partial x} \frac{\partial^4 \eta(x)}{\partial x^4} + \right. \\
 & 4X(T_1) \bar{Y}(T_1) \frac{\partial^2 \Phi(x)}{\partial x^2} \frac{\partial^3 \eta(x)}{\partial x^3} + \\
 & \left. 3X(T_1) \bar{Y}(T_1) \frac{\partial^2 \bar{\eta}(x)}{\partial x^2} \frac{\partial^3 \Phi(x)}{\partial x^3} \right) \exp(i\omega T_0) \exp(-i\lambda T_0) - \\
 & \left(C6X(T_1) \bar{Y}(T_1) \frac{\partial \Phi(x)}{\partial x} \frac{\partial^2 \eta(x)}{\partial x^2} + \right. \\
 & C6X(T_1) \bar{Y}(T_1) \frac{\partial \eta(x)}{\partial x} \frac{\partial^2 \Phi(x)}{\partial x^2} \Big) \exp(i\omega T_0) \exp(-i\lambda T_0) + \left[\left(\frac{1}{2} \left(C22\mu_2 \frac{\partial \eta(x)}{\partial x} \bar{U}_2 \lambda \right) - \right. \right. \\
 & \frac{1}{2} \left(C42\Omega_2\mu_2 \frac{\partial \eta(x)}{\partial x} \bar{U}_2 \right) + aC32\mu_2 \frac{\partial^2 \eta(x)}{\partial x^2} \bar{U}_2^2 i - \\
 & C32\mu_2 \frac{\partial^2 \eta(x)}{\partial x^2} \bar{U}_2^2 i \Big) \exp(-i\Omega_2 T_0) + \left(\frac{1}{2} \left(C21\mu_1 \frac{\partial \eta(x)}{\partial x} \bar{U}_1 \lambda \right) - \right. \\
 & \frac{1}{2} \left(C41\Omega_1\mu_1 \frac{\partial \eta(x)}{\partial x} \bar{U}_1 \right) + aC31\mu_1 \frac{\partial^2 \eta(x)}{\partial x^2} \bar{U}_1^2 i - \\
 & C31\mu_1 \frac{\partial^2 \eta(x)}{\partial x^2} \bar{U}_1^2 i \Big) \exp(-i\Omega_1 T_0) - \left(\frac{1}{2} \left(C21\mu_1 \frac{\partial \eta(x)}{\partial x} \bar{U}_1 \lambda \right) - \right. \\
 & \frac{1}{2} \left(C41\Omega_1\mu_1 \frac{\partial \eta(x)}{\partial x} \bar{U}_1 \right) + aC31\mu_1 \frac{\partial^2 \eta(x)}{\partial x^2} \bar{U}_1^2 i - C31\mu_1 \frac{\partial^2 \eta(x)}{\partial x^2} \bar{U}_1^2 i \Big) \exp(i\Omega_1 T_0) - \\
 & \left. \left(\frac{1}{2} \left(C22\mu_2 \frac{\partial \eta(x)}{\partial x} \bar{U}_2 \lambda \right) - \frac{1}{2} \left(C42\Omega_2\mu_2 \frac{\partial \eta(x)}{\partial x} \bar{U}_2 \right) + aC32\mu_2 \frac{\partial^2 \eta(x)}{\partial x^2} \bar{U}_2^2 i - \right. \right.
 \end{aligned} \tag{24}$$

$$\begin{aligned}
 & C32\mu_2 \frac{\partial^2 \eta(x)}{\partial x^2} \bar{U}_2^2 i) \exp(i\Omega_2 T_0) \Big] Y(T_1) \exp(i\lambda T_0) + \left[\left(\frac{1}{2} \left(C21\mu_1 \frac{\partial \bar{\eta}(x)}{\partial x} \bar{U}_1 \lambda \right) - \right. \right. \\
 & \left. \frac{1}{2} \left(C41\Omega_1 \mu_1 \frac{\partial \bar{\eta}(x)}{\partial x} \bar{U}_1 \right) - aC31\mu_1 \frac{\partial^2 \bar{\eta}(x)}{\partial x^2} \bar{U}_1^2 i + C31\mu_1 \frac{\partial^2 \bar{\eta}(x)}{\partial x^2} \bar{U}_1^2 i \right) \exp(i\Omega_1 T_0) + \\
 & \left(\frac{1}{2} \left(C22\mu_2 \frac{\partial \bar{\eta}(x)}{\partial x} \bar{U}_2 \lambda \right) - \frac{1}{2} \left(C42\Omega_2 \mu_2 \frac{\partial \bar{\eta}(x)}{\partial x} \bar{U}_2 \right) - aC32\mu_2 \frac{\partial^2 \bar{\eta}(x)}{\partial x^2} \bar{U}_2^2 i + \right. \\
 & \left. \left. C32\mu_2 \frac{\partial^2 \bar{\eta}(x)}{\partial x^2} \bar{U}_2^2 i \right) \exp(i\Omega_2 T_0) \Big] \bar{Y}(T_1) \exp(-i\lambda T_0) + NST + CC = 0
 \end{aligned}$$

Here NST denotes non-secular terms. Examining the equations for expressions that will lead to secular terms, it can be observed that various scenarios exist. However, unlike pulsating single-phase flow, three fundamental parametric resonance problems that are solely associated with the planar dynamics of pipes with pulsating two-phase flow are identified:

- Parametric resonance case with Ω_1 and Ω_2 close to 2λ but far from 2ω
- Parametric resonance case with Ω_1 and Ω_2 close to 2ω but far from 2λ
- Parametric resonance case with Ω_1 close to 2ω and Ω_2 close to 2λ

ω and λ are the axial and transverse natural frequencies. As reported in [4], there is 1:2 internal resonance relationships between the axial and transverse frequencies. However, this study only considers the transverse vibrations with parametric resonance case where Ω_1 and Ω_2 are equal and close to 2λ but far from 2ω for both the internal resonance condition and ($\omega = 2\lambda$) away from the internal resonance condition ($\omega \neq 2\lambda$).

The proximity of nearness is expressed as: $\Omega_1 = 2\lambda + \varepsilon\sigma_2$ and $\Omega_2 = 2\lambda + \varepsilon\sigma_2$, (Where σ_2 is the detuning parameter between the forcing frequency and transverse natural frequency).

3.1.1 When ω is far from 2λ (Away from Internal resonance condition)

The inner product defined for complex functions on $\{0, 1\}$ as: $\langle f, g \rangle = \int_0^1 f \bar{g} dx$.

Solvability criterion demands that the coefficient of $\exp(i\omega T_0)$ and $\exp(i\lambda T_0)$ should vanish [5]. This implies that, $X(T_1)$ and $Y(T_1)$ should satisfy the following relation:

$$\frac{\partial X(T_1)}{\partial T_1} = 0 \tag{21}$$

$$\frac{\partial Y(T_1)}{\partial T_1} + NY(T_1)^2 \bar{Y}(T_1) + M\bar{Y}(T_1) \exp(i\sigma_2 T_1) = 0 \tag{22}$$

Where: $N = \frac{\int_0^1 [B2] \bar{\eta}(x) dx}{-\int_0^1 [B1] \bar{\eta}(x) dx}$, $M = \frac{\int_0^1 [B4+B5] \bar{\eta}(x) dx}{-\int_0^1 [B1] \bar{\eta}(x) dx}$.

B1, B2, B4 and B5 are defined in the appendix.

Expressing the solutions of equations (18) and (19) in polar form as:

$$Y(T_1) = \frac{1}{2} \alpha y(T_1) e^{i\beta y(T_1)} \quad \text{and} \quad \bar{Y}(T_1) = \frac{1}{2} \alpha y(T_1) e^{-i\beta y(T_1)} \tag{23}$$

$$X(T_1) = \frac{1}{2} \alpha x(T_1) e^{i\beta x(T_1)} \quad \text{and} \quad \bar{X}(T_1) = \frac{1}{2} \alpha x(T_1) e^{-i\beta x(T_1)} \tag{24}$$

Solving equation (25) for $X(T_1)$, gives a constant amplitude solution up to the 1st order approximation:

$$X(T_1) = \alpha x_0 \tag{25}$$

Adopting the assumed solutions in equation (28), the modulation equations are formed. With 'R' the real parts and 'I' the imaginary parts of M and N. The stationary solutions are obtained as:

$$\psi = \tan^{-1} \left(\frac{NI\alpha y(T_1)^2 + 2\sigma_2}{NR\alpha y(T_1)^2} \right) - \tan^{-1} \left(\frac{MI}{MR} \right) \tag{26}$$

$$(NI^2 + NR^2)\alpha y(T_1)^4 + 4NI\sigma_2\alpha y(T_1)^2 - 16MR^2 - 16MI^2 + 4\sigma_2^2 = 0 \tag{27}$$

With $A = NI^2 + NR^2$, $B = 4NI\sigma_2$, $C = 4\sigma_2^2 - 16MR^2 - 16MI^2$

The solution of equation (24) will produce four roots of $\alpha y(T_1)$:

$$\alpha y(T_1) = \pm \sqrt{\frac{-\frac{2(B+\sqrt{B^2-4AC})}{A}}{2}} \text{ or } \pm \sqrt{\frac{-\frac{2(B-\sqrt{B^2-4AC})}{A}}{2}} \tag{32}$$

However, the acceptable solution of $\alpha y(T_1)$ is the root of the quartic equation (31) that is real and positive. Considering: $T_0 = t$, $\alpha y(T_1)_n = \alpha y_n$, $\beta y(T_1)_n = \frac{\sigma_{2n}T_1 - \psi_n}{2}$, $\Omega_1 = \Omega_2 = \Omega$.

With the stability condition fulfilled, the particular solution of equation (24) away from internal resonance condition is obtained as:

$$v_1 = \frac{G1\alpha y(T_1)^3}{4} \cos(3(\beta y(T_1) + T_0\lambda)) + G2\alpha y(T_1) \cos(\beta y(T_1) + T_0(\Omega + \lambda)) \tag{33}$$

The first order approximate solution of $\bar{v}(x, t)$ without internal resonance is expressed as:

$$\bar{v}(x, t) = \sum_{n=1}^{\infty} \alpha y_n |\eta(x)_n| \cos\left(\frac{(t\Omega - \psi)}{2} + \phi y_n\right) + O(\epsilon) \tag{34}$$

The phase angles (ϕy_n) are given by: $\tan(\phi y_n) = \frac{Im\{\eta(x)_n\}}{Re\{\eta(x)_n\}}$.

The stability of the solutions is determined by examining the eigenvalues of the Jacobian of the modulation equations. The Jacobian is expressed as:

$$J = \begin{bmatrix} -\frac{NR\alpha y(T_1)}{2} & MI \cos(\psi) + MR \sin(\psi) \\ -\frac{NR\alpha y(T_1)}{2} MI \sin(\psi) & MI \sin(\psi) - MR \cos(\psi) \end{bmatrix} \tag{35}$$

The characteristics equation is obtained by solving for the eigenvalues of the Jacobian,

$$|J - \vartheta I| = 0, \text{ where } \vartheta \text{ are the eigenvalues.}$$

However, to assess the stability of the nonlinear solution (nontrivial solution), we substitute the solutions of $\alpha y(T_1)$ as obtained from equation (32) into the characteristic equation:

$$\vartheta^2 + C1\vartheta + C2 = 0 \tag{36}$$

$$C1 = MR \cos(\psi) - MI \sin(\psi) + \frac{NR\alpha y(T_1)}{2},$$

$$C2 = \frac{MINI\alpha y(T_1) \cos(\psi)}{2} + \frac{MRNR\alpha y(T_1) \cos(\psi)}{2} - \frac{MINR\alpha y(T_1) \sin(\psi)}{2} + \frac{MRNI\alpha y(T_1) \sin(\psi)}{2},$$

Adopting the Routh-Hurwitz criteria, the nonlinear fixed point solution of $\alpha y(T_1)$ is stable only if:

$$C1 > 0 \text{ and } C2 > 0.$$

1.1.1 When ω is close to 2λ (Internal resonance condition)

When $\omega = 2\lambda$, another detuning parameter σ_1 , is introduced: $\omega = 2\lambda + \varepsilon\sigma_1$, therefore; $2\lambda T_0 = \omega T_0 - \sigma_1 T_1$ and $(\omega - \lambda)T_0 = \lambda T_0 + \sigma_1 T_1$, with $\varepsilon T_0 = T_1$.

In this case, solvability condition demands that, $X(T_1)$ and $Y(T_1)$ satisfy the following relation:

$$\frac{\partial X(T_1)}{\partial T_1} - J2Y(T_1)^2 \exp(-\sigma_1 T_1 i) = 0 \tag{37}$$

$$\frac{\partial Y(T_1)}{\partial T_1} + K2Y(T_1)^2 \overline{Y(T_1)} + K3\overline{Y(T_1)} \exp(i\sigma_2 T_1) + K4\overline{Y(T_1)} \exp(i\sigma_2 T_1) = 0 \tag{38}$$

Where: $J2 = \frac{\int_0^1 |A2|\overline{\phi(x)} dx}{-\int_0^1 |A1|\overline{\phi(x)} dx}$, $K2 = \frac{\int_0^1 |B2|\overline{\eta(x)} dx}{-\int_0^1 |B1|\overline{\eta(x)} dx}$, $K3 = \frac{\int_0^1 |B3|\overline{\eta(x)} dx}{-\int_0^1 |B1|\overline{\eta(x)} dx}$, $K4 = \frac{\int_0^1 |B4+B5|\overline{\eta(x)} dx}{-\int_0^1 |B1|\overline{\eta(x)} dx}$.

A1, A2, B1, B2, B3, B4 and B5 are defined in the appendix.

To derive the corresponding modulation equations, the assumed solutions in equations (27) and (28) are adopted. From the stationary solutions of the modulation equations, the linear solutions are obtained as; $\alpha x(T_1) = \alpha y(T_1) = 0$. Representing ‘R’ as the real parts and ‘I’ as the imaginary parts of J2, K2, K3 and K4, the stationary solutions are obtained for the coupled system as:

$$\psi1 = -\tan^{-1} \left(\frac{J2R}{J2I} \right) \tag{39}$$

$$\psi2 = \tan^{-1} \left(\frac{K2I\alpha y(T_1)^2 + 2\sigma_2 + 2K3I\alpha x(T_1)\cos(\psi1) + 2K3R\alpha x(T_1)\sin(\psi1)}{K2R\alpha y(T_1)^2 + 2K3R\alpha x(T_1)\cos(\psi1) + 2K3I\alpha x(T_1)\sin(\psi1)} \right) - \tan^{-1} \left(\frac{K5I}{K5R} \right) \tag{40}$$

Where $CS = \cos(\psi1)$, $SS = \sin(\psi1)$, and other notations in appendix, a quartic equation is obtained in terms of $\alpha y(T_1)$ as:

$$A. \alpha y(T_1)^4 + B. \alpha y(T_1)^2 + C = 0 \tag{41}$$

Where:

$$A = J2I^2 K3I^2 + J2I^2 K3R^2 + J2R^2 K3I^2 + J2R^2 K3R^2 + K2I^2 \sigma_1^2 + K2I^2 \sigma_2^2 + K2R^2 \sigma_1^2 + K2R^2 \sigma_2^2 - 2K2I^2 \sigma_1 \sigma_2 - 2K2R^2 \sigma_1 \sigma_2 + 2K2IK3I\sigma_1 CS \sqrt{J2I^2 + J2R^2} - 2K2IK3I\sigma_2 CS \sqrt{J2I^2 + J2R^2} + 2K2RK3R\sigma_1 CS \sqrt{J2I^2 + J2R^2} -$$

$$2K2RK3R\sigma_2CS\sqrt{J2I^2 + J2R^2} + 2K2IK3R\sigma_1SS\sqrt{J2I^2 + J2R^2} - 2K3IK2R\sigma_1SS\sqrt{J2I^2 + J2R^2} - 2K2IK3R\sigma_2SS\sqrt{J2I^2 + J2R^2} + 2K3IK2R\sigma_2SS\sqrt{J2I^2 + J2R^2}.$$

$$B = 4K2I\sigma_2^3 - 8K2I\sigma_1\sigma_2^2 - 4K2I\sigma_1^2\sigma_2 - 4K3I\sigma_2^2CS\sqrt{J2I^2 + J2R^2} - 4K3R\sigma_2^2SS\sqrt{J2I^2 + J2R^2} + 4K3I\sigma_1\sigma_2CS\sqrt{J2I^2 + J2R^2} + 4K3R\sigma_1\sigma_2SS\sqrt{J2I^2 + J2R^2},$$

$$C = 4\sigma_2^4 - 8\sigma_1\sigma_2^3 - 16K4I^2\sigma_1^2 - 16K4I^2\sigma_1^2 - 16K4R^2\sigma_2^2 + 4\sigma_1^2\sigma_2^2 + 32K4I^2\sigma_1\sigma_2 + 32K4R^2\sigma_1\sigma_2.$$

The solution of equation (41) will produce four roots of $\alpha y(T_1)$:

$$\alpha y(T_1) = \pm \frac{\sqrt{-\frac{2(B+\sqrt{B^2-4AC})}{A}}}{2} \text{ or } \pm \frac{\sqrt{-\frac{2(B-\sqrt{B^2-4AC})}{A}}}{2} \tag{42}$$

However, the acceptable solution of $\alpha y(T_1)$ is the root of the quartic equation (41) that is real and positive. The expression for estimating $\alpha x(T_1)$ is obtained as a function of $\alpha y(T_1)$ as:

$$\alpha x(T_1) = \sqrt{\frac{\alpha y(T_1)^4(J2I^2 + J2R^2)}{4(\sigma_2 - \sigma_1)}} \tag{43}$$

Considering: $T_0 = t$, $\alpha x(T_1)_n = \alpha x_n$, $\alpha y(T_1)_n = \alpha y_n$, and $\Omega_1 = \Omega_2 = \Omega$.

With the solvability condition fulfilled, the particular solution of equation (17) is obtained as:

$$v_1 = \frac{G1\alpha y(T_1)^3}{4} \cos(3(\beta y(T_1) + T_0\lambda)) + G2\alpha y(T_1) \cos(\beta y(T_1) + T_0(\Omega + \lambda)) + \frac{G3\alpha x(T_1)\alpha y(T_1)}{2} \cos(\beta x(T_1) + \beta y(T_1) + T_0(\omega + \lambda)) \tag{44}$$

The first order approximate solution of $\bar{v}(x, t)$ with internal resonance is expressed as:

$$\bar{v}(x, t) = \sum_{n=1}^{\infty} \alpha y_n |\eta(x)_n| \cos\left(\frac{t\Omega}{2} - \frac{\psi 2_n}{2} + \varphi y_n\right) + O(\varepsilon) \tag{45}$$

The phase angles φx_n and φy_n are given by:

$$\tan(\varphi x_n) = \frac{Im\{\phi(x)_n\}}{Re\{\phi(x)_n\}}, \quad \tan(\varphi y_n) = \frac{Im\{\eta(x)_n\}}{Re\{\eta(x)_n\}}.$$

The stability of the solutions is determined by examining the eigenvalues of the Jacobian of the modulation equations. The Jacobian is expressed as:

$$J = \begin{bmatrix} \frac{K3P2}{2} - \frac{K2Q1^2}{4} - K4 - \frac{3K2P1^2}{4} & \frac{K3Q2}{2} - \frac{\sigma_2}{2} - \frac{K2P1Q1}{2} & \frac{K3P1}{2} & \frac{K3Q1}{2} \\ \frac{\sigma_2}{2} + \frac{K3Q2}{2} - \frac{K2P1Q1}{2} & K4 - \frac{3K2Q1^2}{4} - \frac{K2P1^2}{4} - \frac{K3P2}{2} & -\frac{K3Q1}{2} & \frac{K3P1}{2} \\ -J2P1 & J2Q1 & 0 & \sigma_1 - \sigma_2 \\ -J2Q1 & -J2P1 & \sigma_2 - \sigma_1 & 0 \end{bmatrix} \tag{46}$$

The characteristics equation is obtained by solving for the eigenvalues of the Jacobian, $|J - \vartheta I| = 0$, where ϑ are the eigenvalues.

To assess the stability of the linear solution (trivial solution), we substitute $P_n = Q_n = 0$ in the characteristic equation:

$$\vartheta^4 + \left(\sigma_1^2 - K4^2 + 2\sigma_1\sigma_2 + \frac{5\sigma_2^2}{14} \right) \vartheta^2 + 2K4^2\sigma_1\sigma_2 - K4^2\sigma_1 - K4^2\sigma_2 + \frac{(\sigma_1\sigma_2)^2}{4} - \frac{\sigma_1\sigma_2^3}{2} + \frac{\sigma_2^4}{4} = 0 \tag{47}$$

The trivial solution of $\alpha x(T_1)$ and $\alpha y(T_1)$, is unstable if at least one eigenvalue has a positive real part, otherwise it is stable. However, to analyze the stability of the nonlinear solution (nontrivial solution), we substitute the solutions of αy and αx as obtained from equations (42) and (43) into the characteristic equation:

$$\vartheta^4 + C1\vartheta^3 + C2\vartheta^2 + C3\vartheta + C4 = 0 \tag{48}$$

$$C1 = K2\alpha y(T_1)^2,$$

$$C2 = \frac{K2^2\alpha y(T_1)^4}{4} + \sigma_1^2 - 2\sigma_1\sigma_2 + \sigma_2^2 - J2K3\alpha y(T_1)^2,$$

$$C3 = \frac{K2\alpha y(T_1)(2\sigma_1^2 - 2J2K3\alpha y(T_1)^2 - 4\sigma_1\sigma_2 + 2\sigma_2^2)}{2},$$

$$C4 = \frac{J2^2J3K2\alpha y(T_1)^4}{4} - \frac{J2K3\alpha y(T_1)^2\sigma_1\sigma_2}{2} + \frac{J2K3\alpha y(T_1)^2\sigma_2^2}{2} + \frac{K2^2\alpha y(T_1)^4\sigma_1^2}{4} - \frac{K2^2\alpha y(T_1)^4\sigma_1\sigma_2}{2} + \frac{K2^2\alpha y(T_1)^4\sigma_2^2}{4}.$$

Adopting the Routh-Hurwitz criteria, the nonlinear fixed point solution of αx and αy is stable only if:

$$C1 > 0, C3 > 0, C4 > 0 \text{ and } C1C2C3 > (C3^2 + C1^2C4)$$

3. Results and Discussion

The numerical simulation considered a cantilever pipe with external diameter of 11.38mm, internal diameter of 9.25mm and length of 146.7mm. Its density is 7800 kg/m³. The pipe conveys air/water two-phase flow with void fractions of 0.1, 0.3, and 0.5. Critical mixture flow velocities of 11.5, 12.5 and 14.6 for the respective void fractions are obtained from Argand diagram. Pre-critical velocity of 2, and a post-critical velocity of 16 are simulated to assess the pre-buckling and post-buckling behaviour of the pipe as it responds to parametric forced vibrations of the pulsating flow.

4.1 Results for ω far from 2λ (Away from internal resonance condition)

In the absence of internal resonance, the near resonant frequency response of the system is identical to a Duffing system with parametric excitation or the nonlinear Mathieu's equation. Figure 2 shows that in all cases, the peak of the response tilts to the left; this indicates the presence of nonlinear restoring forces of the softening type in the dynamics. In addition, at post-critical flow condition, higher void fractions of 0.3 and 0.5 resulted to a transition between subcritical and supercritical pitchfork bifurcation compared with lower void fraction and the pre-critical flow condition results. The transverse response when the pulsation frequency is perfectly tuned to the transverse natural frequency for all the void fractions as depicted in Figure 5 of Appendix 1 are observed to be with beating time series and dense phase plane orbits which fills up the phase plane. The spectra density

plots exhibited two concentrated peak which is confirms a quasiperiodic motion with two dominating frequencies.

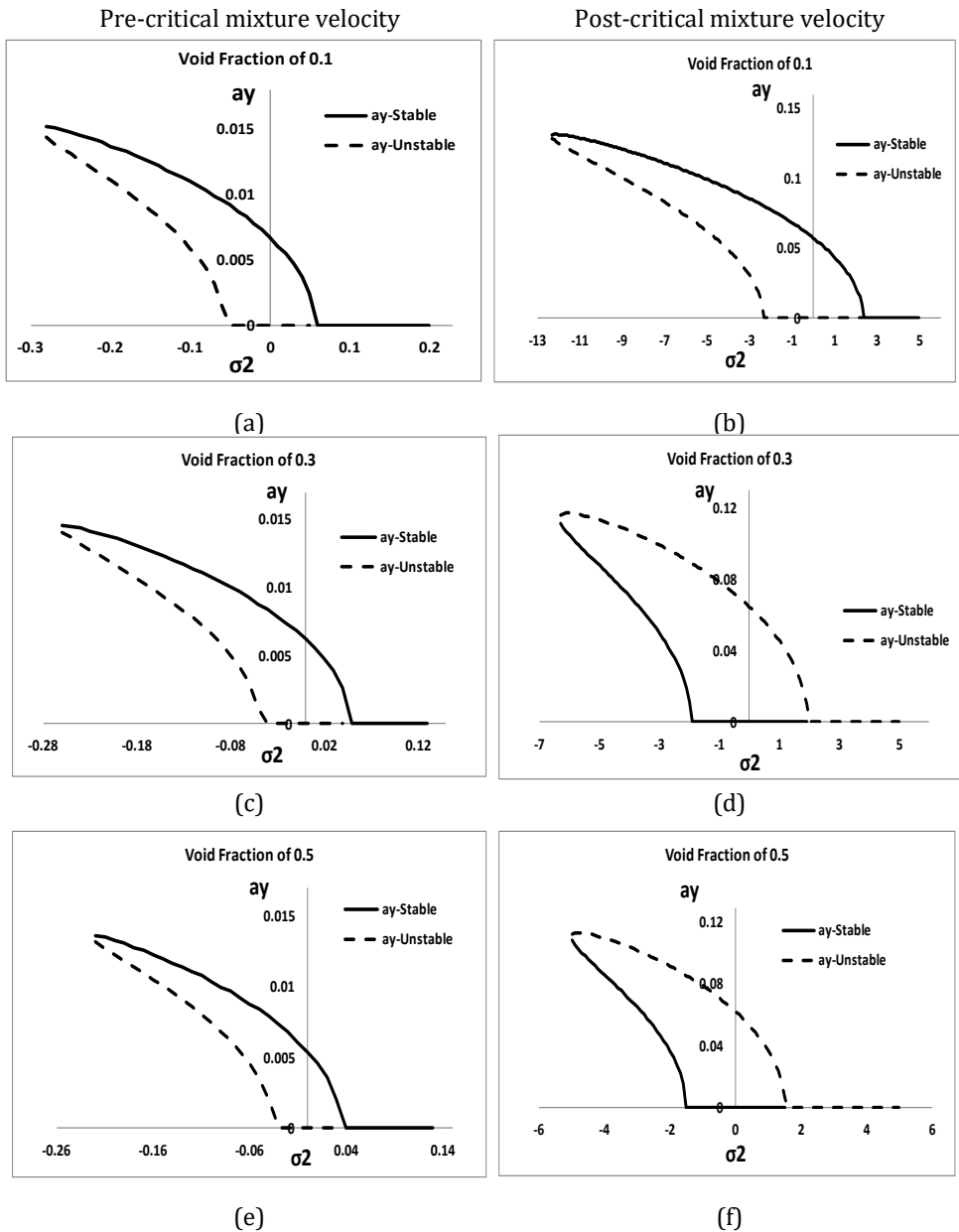


Fig. 2 Frequency response plots of the transverse parametric resonance of the second

4.2 Results for ω close to 2λ (Internal resonance condition)

Figure 3 show that when the pulsation frequency is coincident with the transverse natural frequency, the axial response peaks at infinity with no vibrations in the transverse plane. Apparently due to the nonlinear internal coupling between the axes, the absence of the transverse oscillations when the axial peaks to infinity will aid in neutralizing the axial

resonance peaks. The time traces of the tip motions for a perfectly tuned internal resonance with the pulsation frequency slightly detuned by 0.5 for all the void fractions as depicted in Figure 6 of Appendix 1 are observed to be with beating time series and dense phase plane orbits which fills up the phase plane. The spectra density plots exhibited four concentrated peak which is confirms a quasiperiodic motion with four dominating frequencies.

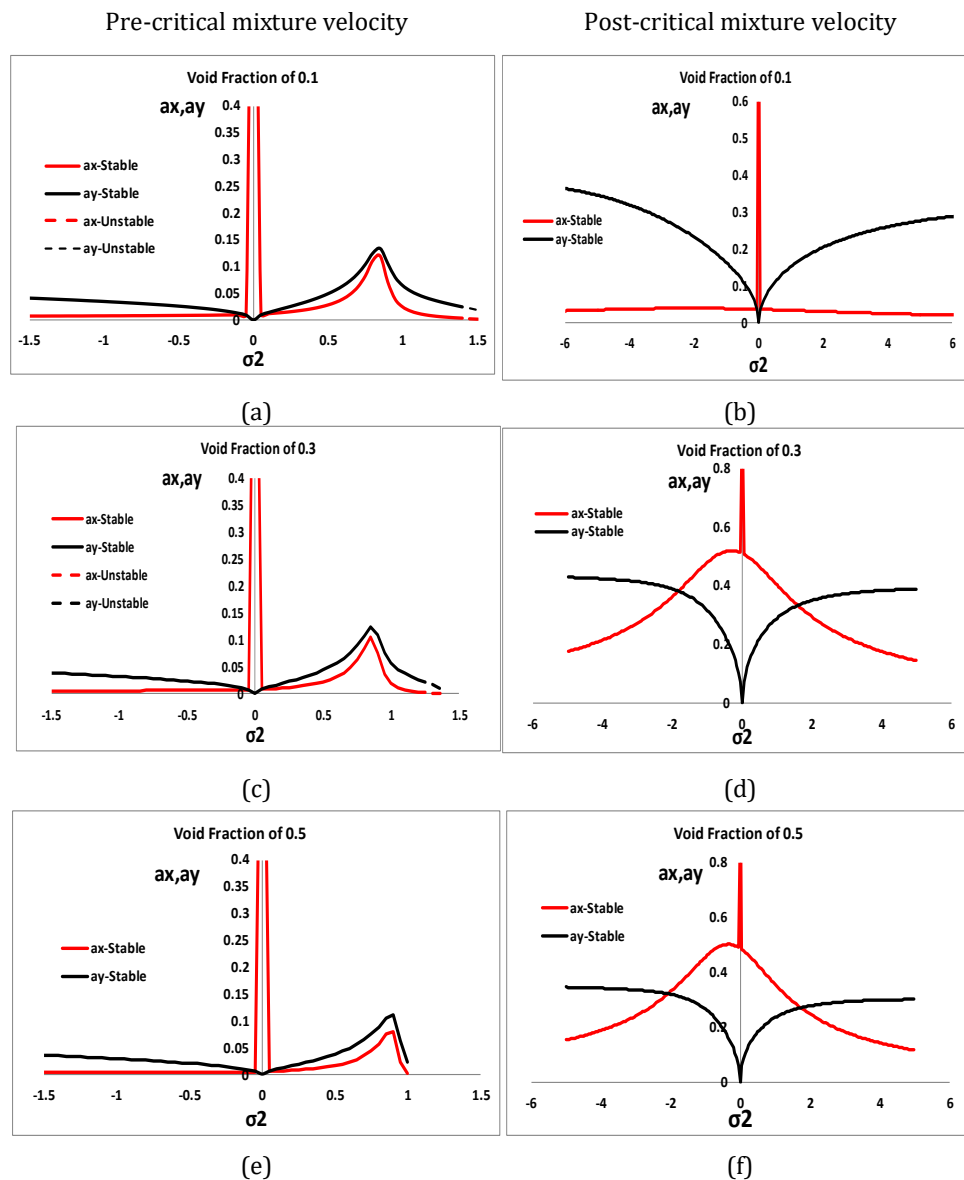


Fig. 2 Frequency response plots of the perfectly tuned ($\sigma_1 = 0$) internal resonance of

4. Conclusion

This work advanced the knowledge of nonlinear dynamics of parametric forced vibrations of cantilever pipe with pulsating two-phase flow. Contrary to the dynamics of pulsating

single-phase flow, the pulsating two-phase flow system presents three principal parametric resonance regimes. Obviously, these are exclusive characteristics of the planar dynamics of pulsating two-phase flow in pipes. With respect to practical applications, low void fractions would be enough for the analysis of two-phase flow systems. However, the 2:1 oscillatory pattern of the resonance response in the neighbourhood of the critical points motivated the extension of this analysis to flow conditions with high void fractions. In the absence of internal resonance, the frequency response exhibits softening nonlinear behaviour for the void fractions considered in this analysis. This is valid for pre- and post-critical flow conditions. At higher void fraction, the post-critical flow dynamics indicated continuous interchange between subcritical and supercritical pitchfork bifurcations. Meanwhile, in the presence of internal resonance, the system exhibits nonlinear anti-resonance properties.

Nomenclature

ε	Dimensionless book-keeping parameter
u	Displacement in pipe's axial direction (m)
v	Displacement in pipe's transverse direction (m)
Ω_1, Ω_2	Pulsation frequencies for the phases
μ_1, μ_2	Pulsation amplitudes for the phases
U_j	Flow velocity of individual phases (m/s)
M_j	Flow mass of individual phases (Kg)
m_p	Mass of pipe (Kg)
ν	Poisson ratio
E	Modulus of Elasticity (N/m ²)
I	Mass moment of Inertia (kgm ²)
L	Length of pipe (m)
V_T	Mixture velocity (m/s)
U_g, U_l	Superficial velocities (m/s)
S	Slip ratio
v_f	Void ratio
α	Pipe linear expansivity (°C ⁻¹)
ΔT	Temperature difference (°C)
ρ_g, ρ_l	Densities (Kg/m ³)
t	Time (s)

Appendix I: Time trace, Phase plot and spectral density plots of the pipe's tip transverse motions.

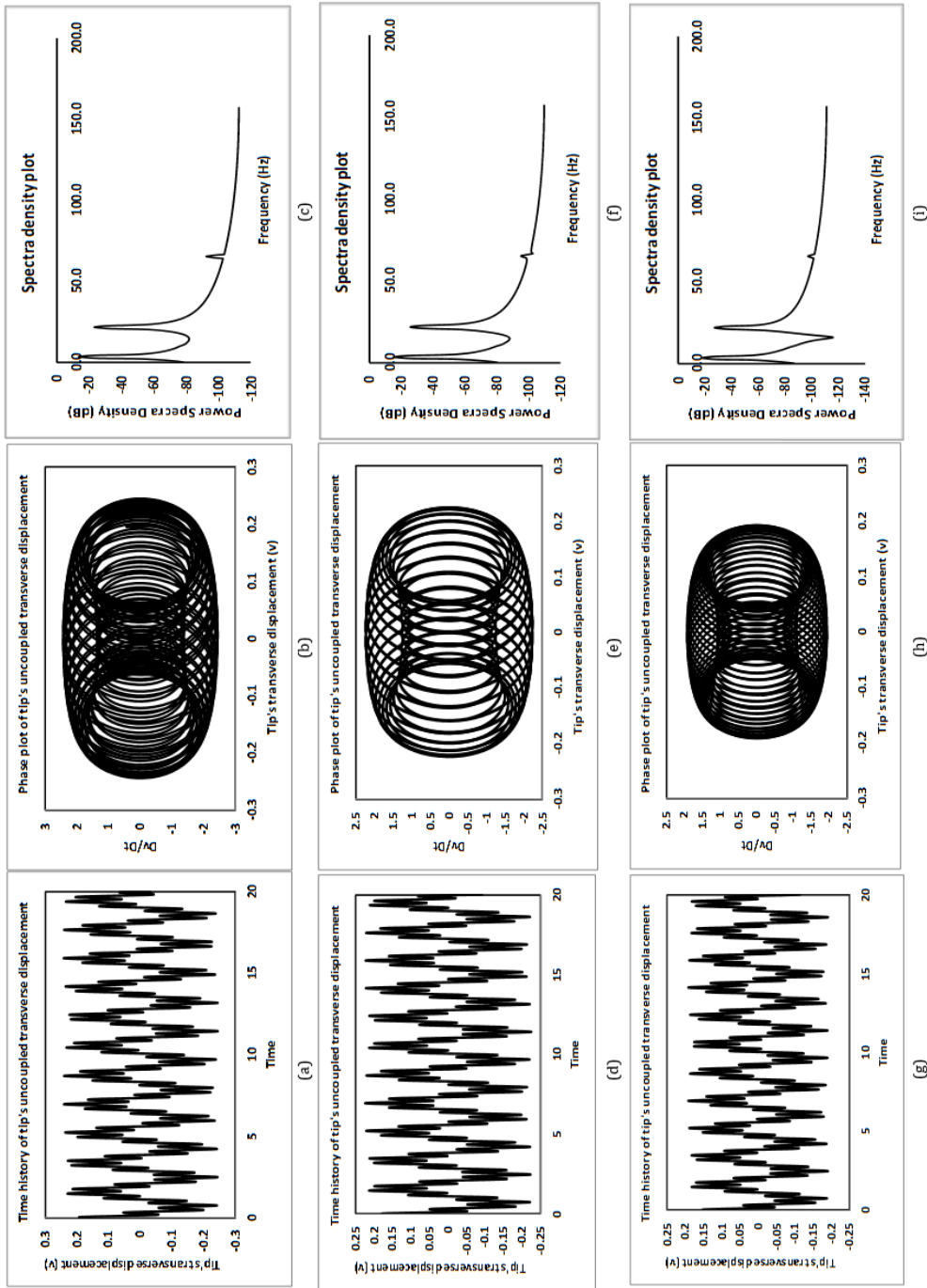


Fig. 4 Uncoupled time history, phase plots and spectral density plots of the pipe's tip transverse vibrations at pre-critical mixture velocity

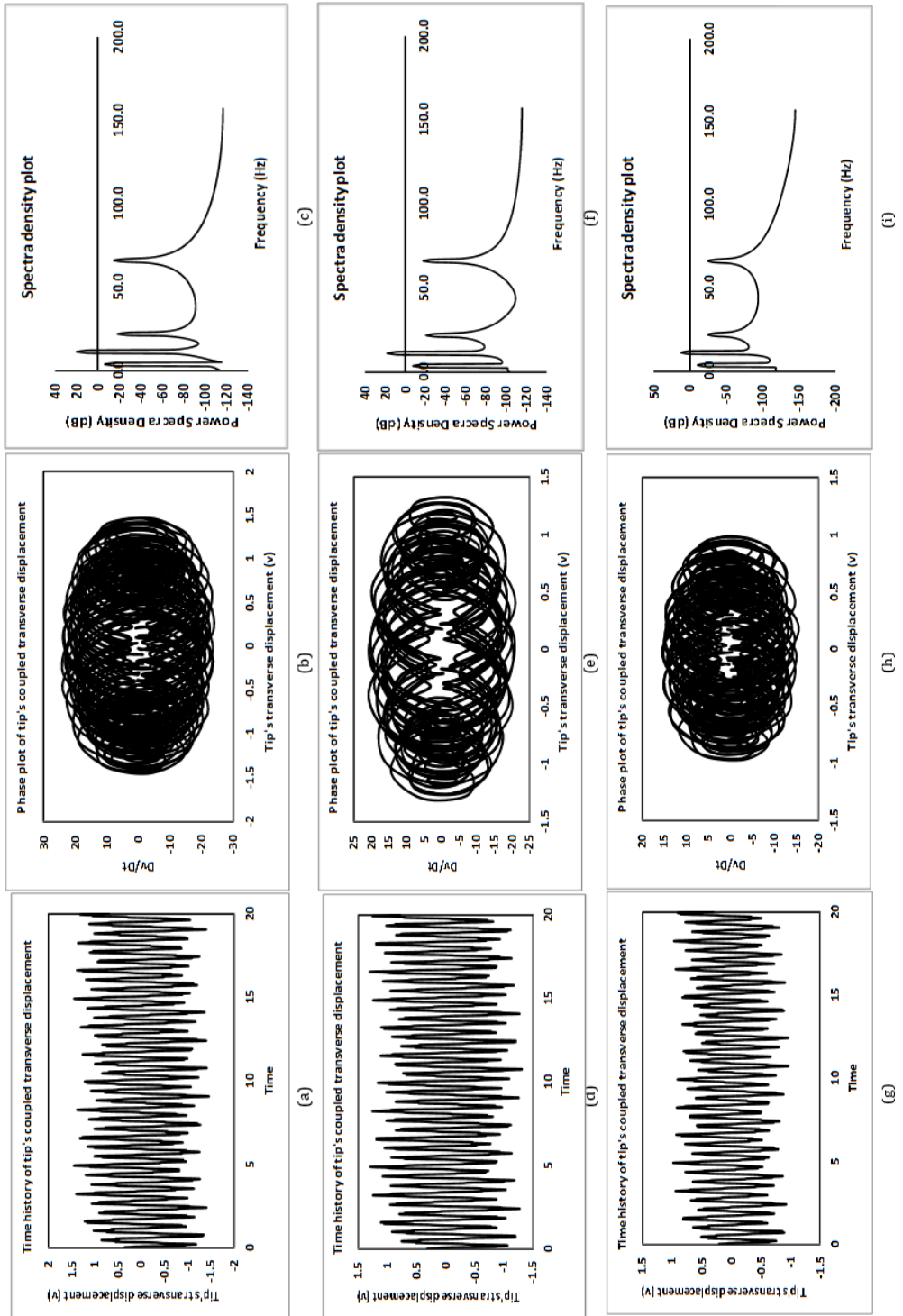


Fig. 5 Coupled time history, phase plots and spectral density plots of the pipe's tip transverse vibrations at pre-critical mixture velocity

Appendix II: Abbreviations

$$A1 = \left(C21 \frac{\partial \phi(x)}{\partial x} \bar{U}_1 + C22 \frac{\partial \phi(x)}{\partial x} \bar{U}_2 + 2\phi(x)\omega i \right)$$

$$A2 = \left(\frac{\partial \eta(x)}{\partial x} \frac{\partial^4 \eta(x)}{\partial x^4} + \frac{\partial^2 \eta(x)}{\partial x^2} \frac{\partial^3 \eta(x)}{\partial x^3} - C6 \frac{\partial \eta(x)}{\partial x} \frac{\partial^2 \eta(x)}{\partial x^2} \right) \varepsilon \sigma_2$$

$$B1 = \left(C21 \frac{\partial \eta(x)}{\partial x} \bar{U}_1 + C22 \frac{\partial \eta(x)}{\partial x} \bar{U}_2 + 2\eta(x)\lambda i \right)$$

$$B2 = 6 \left(\frac{\partial \eta(x)}{\partial x} \right)^2 \frac{\partial \eta(x)}{\partial x} + 2 \left(\frac{\partial \eta(x)}{\partial x} \right)^2 \frac{\partial^4 \eta(x)}{\partial x^4} + 4 \frac{\partial \eta(x)}{\partial x} \frac{\partial \eta(x)}{\partial x} \frac{\partial^4 \eta(x)}{\partial x^4} + 8 \frac{\partial \eta(x)}{\partial x} \frac{\partial^2 \eta(x)}{\partial x^2} \frac{\partial^3 \eta(x)}{\partial x^3} + 8Y(T_1)^2 \bar{Y}(T_1) \frac{\partial \eta(x)}{\partial x} \frac{\partial^2 \eta(x)}{\partial x^2} \frac{\partial^3 \eta(x)}{\partial x^3} - 3C6 \frac{\partial \eta(x)}{\partial x} \frac{\partial \eta(x)}{\partial x} \frac{\partial^2 \eta(x)}{\partial x^2} + 8 \frac{\partial \eta(x)}{\partial x} \frac{\partial^2 \eta(x)}{\partial x^2} \frac{\partial^3 \eta(x)}{\partial x^3} - \frac{3}{2} C6 \left(\frac{\partial \eta(x)}{\partial x} \right)^2 \frac{\partial^2 \eta(x)}{\partial x^2}$$

$$B3 = \left(2 \frac{\partial \Phi(x)}{\partial x} \frac{\partial^4 \eta(x)}{\partial x^4} + \frac{\partial \eta(x)}{\partial x} \frac{\partial^4 \Phi(x)}{\partial x^4} + 4 \frac{\partial^2 \Phi(x)}{\partial x^2} \frac{\partial^3 \eta(x)}{\partial x^3} + 3 \frac{\partial^2 \eta(x)}{\partial x^2} \frac{\partial^3 \Phi(x)}{\partial x^3} - C6 \frac{\partial \Phi(x)}{\partial x} \frac{\partial^2 \eta(x)}{\partial x^2} - C6 \frac{\partial \eta(x)}{\partial x} \frac{\partial^2 \Phi(x)}{\partial x^2} \right)$$

$$B4 = \left(\frac{1}{2} \left(C22\mu_2 \frac{\partial \eta(x)}{\partial x} \bar{U}_2 \lambda \right) - \frac{1}{2} \left(C42\varepsilon\sigma_2\mu_2 \frac{\partial \eta(x)}{\partial x} \bar{U}_2 \right) + aC32\mu_2 \frac{\partial^2 \eta(x)}{\partial x^2} \bar{U}_2^2 i - C32\mu_2 \frac{\partial^2 \eta(x)}{\partial x^2} \bar{U}_2^2 i \right)$$

$$B5 = \left(\frac{1}{2} \left(C21\mu_1 \frac{\partial \eta(x)}{\partial x} \bar{U}_1 \lambda \right) - \frac{1}{2} \left(C41\varepsilon\sigma_2\mu_1 \frac{\partial \eta(x)}{\partial x} \bar{U}_1 \right) + aC31\mu_1 \frac{\partial^2 \eta(x)}{\partial x^2} \bar{U}_1^2 i - C31\mu_1 \frac{\partial^2 \eta(x)}{\partial x^2} \bar{U}_1^2 i \right)$$

G1 =

$$\frac{2\left(\frac{d\eta(x)}{dx}\right)^3 + 2\left(\frac{d\eta(x)}{dx}\right)^2 d^4\eta(x) + 3C6\left(\frac{d\eta(x)}{dx}\right)\frac{d^2\eta(x)}{dx^2} + 8\frac{d\eta(x)}{dx}\frac{d^2\eta(x)}{dx^2}\frac{d^3\eta(x)}{dx^3}}{\int_0^1 \eta(x) \left[2C31 \frac{d^2\eta(x)}{dx^2} (\bar{U}_1)^2 - C7 \frac{d^2\eta(x)}{dx^2} + 2C32 \frac{d^2\eta(x)}{dx^2} (\bar{U}_2)^2 - C31\alpha \frac{d^2\eta(x)}{dx^2} (\bar{U}_1)^2 - C32\alpha \frac{d^2\eta(x)}{dx^2} (\bar{U}_2)^2 + 3C21 \frac{d\eta(x)}{dx} \bar{U}_1 \lambda_{n1} t + 3C22 \frac{d\eta(x)}{dx} \bar{U}_2 \lambda_{n1} t \right] dx + [(\lambda_{n1})^2 - 9(\lambda_{n1})^2]}$$

G2 =

$$\frac{C6 \frac{d\phi(x)}{dx} d^2\eta(x) - 4 \frac{d^2\phi(x)}{dx^2} d^3\eta(x) - 3 \frac{d^2\eta(x)}{dx^2} d^3\phi(x) - 2 \frac{d\phi(x)}{dx} d^4\eta(x)}{\int_0^1 \eta(x) \left[2C31 \frac{d^2\eta(x)}{dx^2} (\bar{U}_1)^2 - C7 \frac{d^2\eta(x)}{dx^2} + 2C32 \frac{d^2\eta(x)}{dx^2} (\bar{U}_2)^2 - C31\alpha \frac{d^2\eta(x)}{dx^2} (\bar{U}_1)^2 - C32\alpha \frac{d^2\eta(x)}{dx^2} (\bar{U}_2)^2 + C21 \frac{d\eta(x)}{dx} \bar{U}_1 \lambda_{n1} t + C22 \frac{d\eta(x)}{dx} \bar{U}_2 \lambda_{n1} t \right] dx}$$

G3 =

$$\frac{2C32\mu_2 \frac{d^2\eta(x)}{dx^2} (\bar{U}_2)^2 - C32\alpha\mu_2 \frac{d^2\eta(x)}{dx^2} (\bar{U}_2)^2 - \left(\frac{C42\Omega\mu_2}{2} \frac{d\eta(x)}{dx} \bar{U}_2 \right) t + \frac{1}{2} C22\mu_2 \frac{d\eta(x)}{dx} \bar{U}_2 \lambda_{n1} t + 2C31\mu_1 \frac{d^2\eta(x)}{dx^2} (\bar{U}_1)^2 - C32\alpha\mu_1 \frac{d^2\eta(x)}{dx^2} (\bar{U}_1)^2 - \left(\frac{C41\Omega\mu_2}{2} \frac{d\eta(x)}{dx} \bar{U}_1 \right) t + \frac{1}{2} C21\mu_1 \frac{d\eta(x)}{dx} \bar{U}_1 \lambda_{n1} t}{\int_0^1 \eta(x) \left[2C31 \frac{d^2\eta(x)}{dx^2} (\bar{U}_1)^2 - C7 \frac{d^2\eta(x)}{dx^2} + 2C32 \frac{d^2\eta(x)}{dx^2} (\bar{U}_2)^2 - C31\alpha \frac{d^2\eta(x)}{dx^2} (\bar{U}_1)^2 - C32\alpha \frac{d^2\eta(x)}{dx^2} (\bar{U}_2)^2 + C21 \frac{d\eta(x)}{dx} \bar{U}_1 \lambda_{n1} t + C22 \frac{d\eta(x)}{dx} \bar{U}_2 \lambda_{n1} t \right] dx}$$

References

- [1] Song R, Streit P. Design of the world's deepest hybrid riser system for cascade and chinook development. Offshore Technological Conference (OTC). 2011. <https://doi.org/10.4043/21338-MS>
- [2] Chung J, Whitney AK, Loden WA. Nonlinear Transition Motion of Deep Ocean Mining Pipe. ASME J. Energy Resources Technology. 1981; 103: 2 - 10. <https://doi.org/10.1115/1.3230811>
- [3] Gregory RW, Païdoussis MP. Unstable Oscillation of Tubular Cantilevers Conveying Fluid. I. Theory. Proceedings of the Royal Society of London Series A Mathematical and Physical Sciences. 1966; 293: 512 - 527. <https://doi.org/10.1098/rspa.1966.0187>
- [4] Païdoussis MP, Issid NT. Dynamic Stability of Pipes Conveying Fluid. Journal of Sound and Vibration. 1974; 33(3): 267 - 294. [https://doi.org/10.1016/S0022-460X\(74\)80002-7](https://doi.org/10.1016/S0022-460X(74)80002-7)
- [5] Shilling R, Lou YK. An Experimental Study on the Dynamic Response of a Vertical Cantilever Pipe Conveying Fluid. Journal of Energy Resource Technology. 1980; 102(3): 129 - 135. <https://doi.org/10.1115/1.3227862>
- [6] Semler C, Li GX, Païdoussis MP. The Nonlinear Equations of Motion of Pipes Conveying Fluid. Journal of Sound and Vibration. 1994; 169: 577 - 599. <https://doi.org/10.1006/jsvi.1994.1035>
- [7] Ghayesh MH, Païdoussis MP, Amabili M. Nonlinear Dynamics of Cantilevered Extensible Pipes Conveying Fluid. Journal of Sound and Vibration. 2013; 332: 6405 - 6418. <https://doi.org/10.1016/j.jsv.2013.06.026>
- [8] Ibrahim RA. Mechanics of Pipes Conveying Fluids-Part 1 Fundamental Studies. Journal of Pressure Vessel Technology. 2010; 113. <https://doi.org/10.1115/1.4001271>
- [9] Łuczko J, Czerwiński A. Parametric Vibrations of Pipes Induced by Pulsating Flows in Hydraulic Systems. Journal of Theoretical and Applied Mechanics. 2014; 52(3): 719 - 730.
- [10] Ginsberg JH. The Dynamic Stability of a Pipe Conveying a Pulsatile flow. International Journal of Engineering Science. 1973; 11: 1013 - 1024. [https://doi.org/10.1016/0020-7225\(73\)90014-1](https://doi.org/10.1016/0020-7225(73)90014-1)
- [11] Paidoussis MP, Issid NT. Experiments on Parametric Resonance of Pipes Containing Pulsatile Flow, Journal of Applied Mechanics, 1976; 43: 198 - 202. <https://doi.org/10.1115/1.3423807>
- [12] Paidoussis MP, Sundararajan C. Parametric and combination resonances of a pipe conveying pulsating fluid. Journal of Applied Mechanics. 1975; 42: 780 - 784. <https://doi.org/10.1115/1.3423705>
- [13] Semler C, Païdoussis MP. Nonlinear Analysis of the Parametric Resonance of a Planar Fluid-Conveying Cantilevered Pipe. Journal of Fluids and Structures. 1996; 10: 787 - 825. <https://doi.org/10.1006/jfls.1996.0053>
- [14] Namachchivaya NS, Tien WM. Bifurcation Behaviour of Nonlinear Pipes Conveying Pulsating Flow. Journal of Fluids and Structures. 1989; 3: 609 - 629. [https://doi.org/10.1016/S0889-9746\(89\)90157-6](https://doi.org/10.1016/S0889-9746(89)90157-6)
- [15] Panda LN, Kar RC. Nonlinear Dynamics of a Pipe Conveying Pulsating Fluid with Combination. Principal Parametric and Internal Resonances. Journal of Sound and Vibration. 2008; 309: 375 - 406. <https://doi.org/10.1016/j.jsv.2007.05.023>
- [16] Liangqiang Z, Fangqi C, Yushu C. Stability and Bifurcation Analysis of a Pipe Conveying Pulsating Fluid with Combination Parametric and Internal Resonance. Mathematical and Computational Applications. 2016; 20: 200 - 216. <https://doi.org/10.19029/mca-2015-017>
- [17] Oz HR, Boyaci H. Transverse Vibrations of Tensioned Pipes Conveying Fluid with Time-dependent Velocity. Journal of Sound and Vibration. 2000; 236(3): 259 - 276. <https://doi.org/10.1006/jsvi.2000.2985>

- [18] Oz HR. Nonlinear Vibrations and Stability Analysis of Tensioned Pipes Conveying Fluid with Variable Velocity. *International Journal of Nonlinear Mechanics*. 2001; 36: 1031 - 1039. [https://doi.org/10.1016/S0020-7462\(00\)00065-2](https://doi.org/10.1016/S0020-7462(00)00065-2)
- [19] Singh K, Mallik AK. Parametric Instabilities of a Periodically Supported Pipe Conveying Fluid. *Journal of Sound and Vibration*. 1979; 62: 379 - 397. [https://doi.org/10.1016/0022-460X\(79\)90631-X](https://doi.org/10.1016/0022-460X(79)90631-X)
- [20] Yoshizawa M, Nao H, Hasegawa E, Tsujioka Y. Lateral Vibration of a Flexible Pipe Conveying Fluid with Pulsating Flow. *Bulleting of Japan Society of Mechanical Engineers*. 1986; 29: 2243 - 2250. <https://doi.org/10.1299/jsme1958.29.2243>
- [21] Miwa S, Mori M, Hibiki T. Two-phase Flow Induced Vibration in Piping Systems. *Progress in Nuclear Energy*. 2015; 78: 270 - 284. <https://doi.org/10.1016/j.pnucene.2014.10.003>
- [22] Monette C, Pettigrew MJ. Fluidelastic Instability of Flexible Tubes Subjected to Two - phase Internal Flow. *Journal of Fluids and Structures*. 2004; 19: 943 - 956. <https://doi.org/10.1016/j.jfluidstructs.2004.06.003>
- [23] Adegoke AS, Oyediran AA. Natural Frequencies, Modes and Critical Velocities of Top Tensioned Cantilever Pipes Conveying Pressurized Steady Two-phase Flow Under Thermal Loading. *Research on Engineering Structures and Materials Journal*. 2018; 4(4): 297 - 323. <https://doi.org/10.17515/resm2017.16en0301>
- [24] Adegoke AS, Oyediran AA. The Analysis of Nonlinear Vibrations of Top-Tensioned Cantilever Pipes Conveying Pressurized Steady Two-Phase Flow under Thermal Loading. *Mathematical and Computational Applications*. 2017; 22: 44. <https://doi.org/10.3390/mca22040044>
- [25] Wang L, Yang Y, Li Y, Wang Y. Dynamic Behaviours of Horizontal gas-Liquid Pipes Subjected to Hydrodynamic Slug Flow: Modelling and experiments. *International Journal of Pressure Vessels and Piping*. 2018; 161: 50 - 57. <https://doi.org/10.1016/j.ijpvp.2018.02.005>
- [26] Enrique Ortiz-Vidal L, Castillo DG, Valverde Q. Theoretical Study on the Dynamic Behavior of Pipes Conveying Gas-Liquid Flow. *MATEC Web of Conference*. 2018; 148. <https://doi.org/10.1051/mateconf/201814801004>
- [27] Woldesemayat MA, Ghajar AJ. Comparison of Void Fraction Correlations for Different Flow Patterns in Horizontal and Upward Inclined Pipes. *International Journal of Multiphase Flow*. 2007; 33: 347 - 370. <https://doi.org/10.1016/j.ijmultiphaseflow.2006.09.004>

Blank Page



Research Article

Evaluation of different cases of soft story formation for mid-rise RC buildings

Hayri Baytan Ozmen^{1,a}, Mehmet Inel^{2,b}, Yunus Demirtas^{*1,c}

¹Department of Civil Engineering, Usak University, Usak, Turkey.

²Department of Civil Engineering, Pamukkale University, Denizli, Turkey.

Article Info

Article history:

Received 04 Dec 2019

Revised 22 Jan 2020

Accepted 29 Jan 2020

Keywords:

Infill-wall;

Nonlinear;

Performance

evaluation;

Reinforced concrete;

Soft story

Abstract

Soft story irregularity is one of the main reasons of the building damage during past earthquakes and has been mentioned in almost all reconnaissance reports. Soft story due to increased story height is a recognized subject but soft story may also arise due to abrupt changes in amount of infill walls between stories, which are usually not considered as a part of load bearing system. This study investigates soft story behavior due to increased story height, lack of load bearing infill walls at ground story and existence of both cases using nonlinear static and dynamic response history analyses. Mid-rise reinforced concrete buildings are considered due to their high portion in existing building stock. Displacement capacities at Immediate Occupancy, Life Safety and Collapse Prevention performance levels and story drift demands of the regular and soft story models are determined. Soft story behavior due to change in story height and/or infill amount is evaluated in view of displacement capacities, drift demands and structural behavior. It is observed that, soft story due to infill walls may be as damaging as soft story due to increased story height.

© 2020 MIM Research Group. All rights reserved.

1. Introduction

Soft story irregularity is one of the main reasons of building damages during recent earthquakes in the world as mentioned in almost all reconnaissance reports and studies [1-6]. Previous studies have shown that infill walls have also an important influence on the formation of structural irregularities such as soft floors, weak floors, torsional irregularity and short columns [7-10]. Soft story may arise not only because of sudden changes in structural system (like height of the stories) but also due to abrupt changes in amount of infill walls between stories. Although they are not included in the load bearing system, infill walls affect the seismic behavior of the structure [11-13]. Inappropriate placed infill walls may also adversely affect the dynamic characteristics of the structures [14]. Furthermore, the infill walls may increase the base shear capacity while reducing the fragility of the structure [15, 16, 17].

This study aims to investigate soft story behavior using nonlinear static and dynamic response history analyses for mid-rise RC buildings which are thought to be the most vulnerable in existing building stock. The 4- and 7-storey 3-D building models are designed per premodern earthquake codes to reflect existing mid-rise building stock [18]. Soft story models of the reference buildings are obtained considering increased floor story height, less amount of infill at floor story and both cases. Capacity curves are obtained using nonlinear static analyses. Displacement capacities of the reference and soft story models

*Corresponding author: yunus.demirtas@usak.edu.tr

^a orcid.org/0000-0001-6750-8632; ^b orcid.org/0000-0002-8323-259X; ^c orcid.org/0000-0002-7992-493X;
DOI: [http://dx.doi.org/10.17515/resm2019.168ea1204](https://dx.doi.org/10.17515/resm2019.168ea1204)

are determined at Immediate Occupancy, Life Safety and Collapse Prevention performance levels according to 2018 Turkish Building Earthquake Code [19]. Building models are reduced to "Equivalent" Single-Degree-of-Freedom systems. These models are subjected to 83 different earthquake records and then inter-story drift demands at the ground story (soft story) are determined by using mode shape of the buildings. Nonlinear static analyses are performed using SAP2000 [20]. Beam and column elements are modeled as nonlinear frame elements with lumped plasticity by defining plastic hinges at both ends of beams and columns. Effect of infill walls is modeled through diagonal struts as suggested in FEMA-356 [21]. Shear hinges take into account possible shear failures in existing reinforced concrete buildings. All buildings are modeled with two different transverse steel amounts to investigate the effect of transverse steel on the behavior. Soft story behavior due to change in story height and/or infill amount is evaluated in view of displacement demands, capacities and structural behavior. The outcomes are useful to better understand soft story damages during past earthquakes and to emphasize the effect of infill walls on the behavior.

2. Aim and Scope

Soft story behavior due to increased story height is a well-known subject among civil engineering professionals. But soft-story problems may arise due to many different reasons like changes in load carrying [22] and slab system [2] between stories. Among others, one of the most frequent reasons of the soft story behavior is the abrupt change in the amount of the infill walls between stories. As the infill walls are not regarded as a part of load carrying system, generally civil engineers do not consider their effects on the structural behavior. Therefore, many civil engineers are not conscious enough about soft story occurrence because of infill walls, and required attention is not provided. In this study, effect of infill walls on structural behavior, especially for the soft story, is investigated in order to increase the level of knowledge and awareness on the subject.

The major portion of the building stock of many developing countries consists of deficient mid-rise reinforced concrete buildings. In scope of the study, soft story behavior in existing mid-rise reinforced concrete buildings below code requirements are investigated. Two sets of RC buildings 4-story and 7-story are selected to represent mid-rise buildings located in the high seismicity region of Turkey, five buildings in each set. The selected buildings are typical beam-column RC frame buildings with no shear walls. Since in Turkey still the majority of buildings were constructed according to 1975 Turkish Earthquake Code, the 4- and 7-story buildings are designed according this code considering both gravity and seismic loads (a design ground acceleration of 0.4 g and soil class Z3 that is similar to class C soil of FEMA-356 is assumed [21]. Material properties are assumed to be 16 MPa for the concrete compressive strength and 220 MPa for the yield strength of both longitudinal and transverse reinforcement. Strain-hardening of longitudinal reinforcement has been taken into account and the ultimate strength of the reinforcement is taken as 330 MPa [23]. One of the important deficiencies in the existing building stock is insufficient amount of transverse reinforcement. The transverse reinforcement amount may be considered to represent construction and workmanship. Two different spacings are considered as 100 mm and 200 mm to investigate soft story behavior with different ductility.

3. Building Models

The selected 4- and 7-story buildings have the same plan view as shown in Fig. 1, with 4 bays in X and Y direction as 4 m and 3 m, respectively. Regular story height is 2.8 m. In the figure, the infill walls that meet the requirements of FEMA 356 to form diagonal struts are shown with shaded areas. More detailed information about models are given in [24]. The

other infill walls with openings that prevent diagonal strut formation are considered as dead loads, only. The 4- and 7-story buildings have symmetrical floor plans to avoid any irregularity effects.

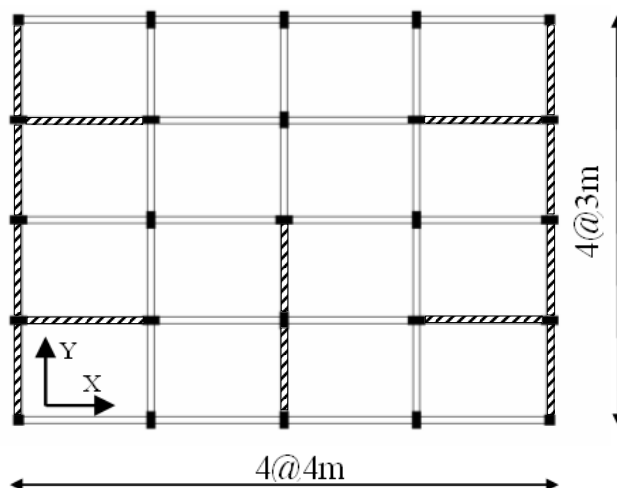


Fig. 1 Plan view of the selected 4- and 7-story buildings

Soft story effect in this study is considered by (i) increasing story height (4 m instead of 2.8 m) at the ground floor, (ii) assuming less amount of infill walls at the ground floor and the existence of the issues (i) and (ii) at the same time is also considered. Source of soft story, model identifier, period of first mode considering cracked section stiffness (T), ratio of yield lateral strength to the seismic weight of building (C_y) values of the building models is given in Table 1. Note that RefNW buildings (reference buildings with no infill effect) are modeled to better understand the effect of neglecting walls as load carrying elements on the building behavior. The last letters in the model identifier express the considered principal direction.

Table 1 Properties of building models

Source of Soft Story	Model	4-story		7-story	
		T (s)	C_y	T (s)	C_y
Reference regular building	Ref-X	0.57	0.17	0.89	0.15
	Ref-Y	0.47	0.25	0.75	0.18
Reference regular building without diagonal struts at any story	RefNW-X	0.84	0.14	1.12	0.12
	RefNW-Y	0.81	0.15	1.1	0.13
Soft story due to increased ground story height (2.8 m to 4 m)	SSH-X	0.67	0.16	0.97	0.13
	SSH-Y	0.54	0.21	0.83	0.16
Soft story due to absence of walls at ground story	SSW-X	0.63	0.17	0.91	0.14
	SSW-Y	0.55	0.2	0.79	0.17
Soft story due to increased height and absence of walls at ground story	SSHW-X	0.84	0.13	1.05	0.12
	SSHW-Y	0.77	0.14	0.94	0.13

3.1. Modeling Approach

Nonlinear static analyses have been performed using SAP2000 Nonlinear Version 8 that is a general-purpose structural analysis program [20]. Three-dimensional model of each structure is created in SAP2000 to carry out nonlinear static analysis. Beam and column elements are modeled as nonlinear frame elements with lumped plasticity by defining plastic hinges at both ends of beams and columns. SAP2000 implements the plastic hinge properties described in FEMA-356 (or ATC-40) [21, 25]. As shown in Figure 2, five points labeled A, B, C, D, and E define force-deformation behavior of a plastic hinge.

The definition of user-defined hinge properties requires moment–curvature analysis of each element. Modified Kent and Park model [26] for unconfined and confined concrete and typical steel stress–strain model with strain hardening [27] for steel are implemented in moment–curvature analyses. The points B and C on Fig. 2 are related to yield and ultimate curvatures. The point B is obtained from SAP2000 using approximate component initial effective stiffness values as per TEC-2007; $0.4EI$ for beams and values depending on axial load level for columns: $0.4EI$ for $N/(Acfc) \leq 0.1$ and $0.8EI$ for $N/(Acfc) \geq 0.4$. f_c is concrete compressive strength, N is axial load, Ac is area of section. For the $N/(Acfc)$ values between 0.1 and 0.4 linear interpolation is made [28].

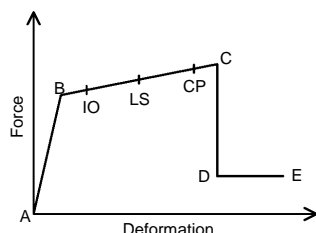


Fig. 2 Force-Deformation relationship of a typical plastic hinge

The ultimate curvature is defined as the smallest of the curvatures corresponding to (1) a reduced moment equal to 80% of maximum moment, determined from the moment–curvature analysis, (2) the extreme compression fiber reaching the ultimate concrete compressive strain as determined using the simple relation provided by Priestley et al. [29] given in Eqn. 1, and (3) the longitudinal steel reaching a tensile strain of 50% of ultimate strain capacity that corresponds to the monotonic fracture strain. Ultimate concrete compressive strain is given as:

$$\epsilon_{cu} = 0.004 + \frac{1.4 \rho_s f_{yh} \epsilon_{su}}{f_{cc}} \tag{1}$$

where ϵ_{cu} is the ultimate concrete compressive strain, ϵ_{su} is the steel strain at maximum tensile stress, ρ_s is the volumetric ratio of confining steel, f_{yh} is the yield strength of transverse reinforcement, and f_{cc} is the peak confined concrete compressive strength.

The input required for SAP2000 is moment–rotation relationship instead of moment–curvature. Also, moment rotation data have been reduced to five-point input that brings some inevitable simplifications. Plastic hinge length is used to obtain ultimate rotation values from the ultimate curvatures. Several plastic hinge lengths have been proposed in

the literature [29, 30]. In this study plastic hinge length definition given in Eqn. 3.2 which is proposed by Priestley et al. is used.

$$L_p = 0.08L + 0.022f_{yh}d_{b1} \geq 0.044f_{yh}d_{b1} \quad (2)$$

In Eqn. 2, L_p is the plastic hinge length, L is the distance from the critical section of the plastic hinge to the point of contraflexure, d_{b1} is the diameter of longitudinal reinforcement.

Following the calculation of the ultimate rotation capacity of an element, acceptance criteria are defined as labeled IO, LS, and CP on Fig. 2. IO, LS, and CP stand for Immediate Occupancy, Life Safety, and Collapse Prevention, respectively. This study defines these three points corresponding to 10%, 60%, and 90% use of plastic hinge deformation capacity. In existing reinforced concrete buildings, especially with low concrete strength and/or insufficient amount of transverse steel, shear failures of members should be taken into consideration. For this purpose, shear hinges are introduced for beams and columns. Because of brittle failure of concrete in shear, no ductility is considered for this type of hinges. Shear hinge properties are defined such that when the shear force in the member reaches its strength, member fails immediately. The shear strength of each member (V_r) is calculated according to TS 500 [23] that is similar to UBC [31]:

$$V_r = 0182bd\sqrt{f_c} \left(1 + 0.07 \frac{N}{A_c} \right) + \frac{A_{sh}f_{yh}d}{s} \quad (3)$$

In Eq. (3), b is section width, d is effective section depth, f_c is concrete compressive strength, N is compression force on section, A_c is area of section, A_{sh} , f_{yh} and s are area, yield strength and spacing of transverse reinforcement, respectively.

Effect of infill walls are modeled through diagonal struts as suggested in TBEC-2018 and FEMA-356. Nonlinear behavior of infill walls is reflected by assigned axial load plastic hinges on diagonal struts whose characteristics are determined as given in FEMA-356. Material properties are taken from TBEC-2018 to reflect characteristics of infill walls in Turkey; 1000 MPa, 1 MPa and 0.15 MPa were assumed as modulus of elasticity, compressive strength and shear strength values, respectively.

It may be noted that the conducted analyses are unidirectional, the out-of plane behaviour of infill walls and bidirectional effects of dynamic loading are not considered in scope of the study. The slip possibility of the longitudinal steel bars is not taken into account, as well.

4. Nonlinear Static Analysis and Performance Evaluation

In order to obtain capacity curves and displacement capacity values of the building models for different performance levels, nonlinear static analyses are carried out using SAP2000. The lateral forces applied at center of mass were proportional to the product of mass and the first mode shape amplitude at each story level under consideration. P-Delta effects were taken into account. Performance evaluation of the investigated buildings is conducted using Turkish Building Earthquake Code (2018). Three damage states as given in Figure 3, Immediate Occupancy (IO), Life Safety (LS), and Collapse Prevention (CP) are considered as specified in this code and several other international guidelines such as FEMA-356, ATC-40.

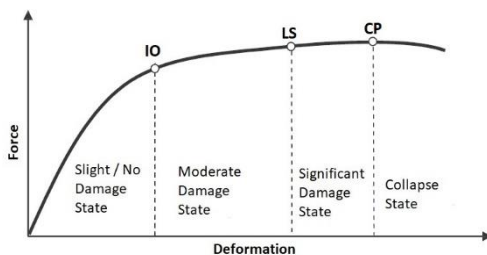


Fig. 3 Damage states

5. Nonlinear Response History Analyses

In order to investigate the soft story behavior on the drift demands nonlinear response history analyses are carried out. The capacity curve of each building obtained from pushover analysis was approximated with a bilinear curve using guidelines given in ATC-40 and FEMA-440 and reduced to equivalent SDOF systems [21, 25]. Then these SDOF systems are subjected to nonlinear response history analysis by using ground motion record sets. USGS site classification based on the average shear wave velocity to a depth of 30 m is used for soil site classification of the selected records. Four site classifications include 83 different records, approximately 20 records for each soil type. Soil type A is the stiffest soil type with highest shear wave velocity and D is the weakest soil with the lowest shear wave velocity. All earthquake records are taken from PEER website [32]. Average values for some properties of selected ground motion records are given in Table 2.

Table 2 Average values for some properties of used ground motion records

Soil Type	Number of records	Magnitude	PGA (g)	PGV (m/s)	PGD (m)
A	20	7.00	0.40	0.30	0.11
B	23	6.71	0.39	0.36	0.11
C	20	7.02	0.40	0.43	0.19
D	20	7.05	0.26	0.36	0.20

6. Analyses Results

The capacity curves are obtained from the pushover analysis. Figure 4 shows capacity curves of the 7-story buildings. Also figure 5 shows the effect of amount of transverse reinforcement for 4-story buildings.

The global drift (GD) capacities (roof displacement/building height) of the building models for Immediate Occupancy (IO), Life Safety (LS), and Collapse Prevention (CP) performance levels are listed in 3 and 4 for 4- and 7-story buildings, respectively. The “s100” and “s200” terms in the model name express the spacing of the transverse reinforcement in mm. The ratio of the given values in tables to the corresponding value for the reference building is presented in the “/Ref” column. The ratio of lateral strength of the building to the weight of the building at the given capacity is provided in the column denoted by “C”. For the evaluation of the soft story behavior on the drift demands, results of nonlinear response analyses are used. The ratio of average drift demands of the soft story models to the corresponding reference model demands at the ground story for each soil type is given in Table 5. Since post-yield stiffness of the buildings was considerably small, the effect of transverse reinforcement amount only changes the ultimate displacement point and don’t

affect the SDOF idealization. Thus, drift demand evaluation is carried out regardless of transverse reinforcement spacing.

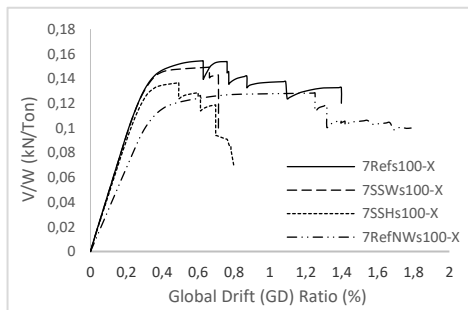


Fig. 4 Capacity curves of 7-story buildings

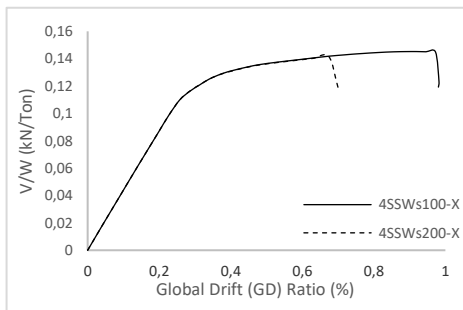


Fig. 5 Capacity curves of 4-story buildings for different transverse reinforcement amount

Table 3 Global drift capacities (%) at given performance levels for the building models for 4-story buildings

Model	IO				LS				CP			
	GD	/Ref	C	/Ref	GD	/Ref	C	/Ref	GD	/Ref	C	/Ref
Refs100-X	0.53	1.00	0.18	1.00	1.08	1.00	0.17	1.00	1.45	1.00	0.17	1.00
Refs100-Y	0.23	1.00	0.20	1.00	0.59	1.00	0.22	1.00	0.84	1.00	0.17	1.00
Refs200-X	0.50	1.00	0.18	1.00	0.68	1.00	0.18	1.00	1.15	1.00	0.17	1.00
Refs200-Y	0.20	1.00	0.18	1.00	0.40	1.00	0.25	1.00	0.63	1.00	0.22	1.00
RefNWs100-X	0.51	0.96	0.14	0.76	0.90	0.83	0.14	0.84	1.36	0.94	0.14	0.85
RefNWs100-Y	0.30	1.32	0.12	0.58	0.78	1.33	0.15	0.70	1.21	1.44	0.15	0.89
RefNWs200-X	0.44	0.89	0.13	0.74	0.68	1.00	0.14	0.75	0.99	0.86	0.14	0.83
RefNWs200-Y	0.25	1.28	0.10	0.56	0.57	1.42	0.15	0.59	0.86	1.36	0.15	0.69
SSHs100-X	0.33	0.62	0.16	0.87	0.81	0.74	0.16	0.97	1.22	0.84	0.12	0.73
SSHs100-Y	0.22	0.96	0.17	0.85	0.49	0.84	0.16	0.73	0.69	0.82	0.15	0.85
SSHs200-X	0.30	0.61	0.15	0.85	0.46	0.68	0.17	0.91	0.82	0.72	0.16	0.97
SSHs200-Y	0.19	0.98	0.16	0.86	0.37	0.94	0.22	0.86	0.47	0.74	0.22	1.00
SSWs100-X	0.28	0.52	0.16	0.87	0.68	0.63	0.17	0.99	1.15	0.79	0.15	0.90
SSWs100-Y	0.16	0.71	0.13	0.66	0.38	0.64	0.20	0.94	0.69	0.82	0.20	1.17
SSWs200-X	0.24	0.48	0.15	0.81	0.37	0.54	0.17	0.92	0.83	0.72	0.15	0.88
SSWs200-Y	0.13	0.67	0.11	0.61	0.24	0.61	0.18	0.72	0.44	0.69	0.21	0.93
SSHWs100-X	0.26	0.48	0.12	0.64	0.55	0.50	0.14	0.82	0.88	0.60	0.14	0.86
SSHWs100-Y	0.17	0.74	0.10	0.47	0.42	0.72	0.15	0.69	0.65	0.78	0.15	0.84
SSHWs200-X	0.23	0.46	0.11	0.61	0.37	0.54	0.13	0.71	0.61	0.53	0.14	0.84
SSHWs200-Y	0.15	0.73	0.08	0.46	0.28	0.70	0.14	0.54	0.45	0.71	0.15	0.68

Table 4 Global drift capacities (%) at given performance levels for the building models for 7-story buildings

Model	IO				LS				CP			
	GD	/Ref	C	/Ref	GD	/Ref	C	/Ref	GD	/Ref	C	/Ref
Refs100-X	0.43	1.00	0.15	1.00	0.65	1.00	0.15	1.00	1.40	1.00	0.13	1.00
Refs100-Y	0.36	1.00	0.18	1.00	0.48	1.00	0.19	1.00	0.68	1.00	0.19	1.00
Refs200-X	0.38	1.00	0.15	1.00	0.59	1.00	0.15	1.00	0.83	1.00	0.14	1.00
Refs200-Y	0.31	1.00	0.17	1.00	0.46	1.00	0.18	1.00	0.58	1.00	0.19	1.00
RefNWs100-X	0.52	1.19	0.12	0.82	0.95	1.45	0.13	0.87	1.25	0.89	0.13	0.97
RefNWs100-Y	0.51	1.40	0.13	0.73	0.89	1.86	0.14	0.74	1.28	1.87	0.14	0.73
RefNWs200-X	0.48	1.25	0.12	0.83	0.81	1.36	0.13	0.83	1.02	1.24	0.13	0.91
RefNWs200-Y	0.43	1.40	0.13	0.75	0.62	1.35	0.13	0.72	0.74	1.26	0.13	0.71
SSHs100-X	0.30	0.69	0.12	0.83	0.48	0.73	0.14	0.93	0.61	0.44	0.13	0.95
SSHs100-Y	0.27	0.74	0.15	0.83	0.41	0.87	0.17	0.88	0.60	0.88	0.17	0.88
SSHs200-X	0.27	0.70	0.11	0.79	0.37	0.63	0.13	0.87	0.49	0.59	0.14	0.97
SSHs200-Y	0.24	0.79	0.14	0.81	0.36	0.78	0.16	0.85	0.46	0.79	0.15	0.82
SSWs100-X	0.33	0.77	0.14	0.92	0.54	0.83	0.15	1.01	0.66	0.47	0.15	1.12
SSWs100-Y	0.25	0.68	0.14	0.81	0.38	0.80	0.17	0.91	0.54	0.80	0.18	0.92
SSWs200-X	0.30	0.78	0.13	0.89	0.43	0.72	0.15	0.95	0.57	0.69	0.15	1.05
SSWs200-Y	0.22	0.71	0.13	0.77	0.31	0.69	0.16	0.85	0.39	0.66	0.16	0.87
SSHWs100-X	0.25	0.58	0.11	0.71	0.40	0.61	0.12	0.85	0.60	0.43	0.13	0.96
SSHWs100-Y	0.19	0.52	0.10	0.57	0.32	0.67	0.14	0.72	0.47	0.69	0.14	0.76
SSHWs200-X	0.23	0.60	0.10	0.69	0.32	0.54	0.12	0.78	0.44	0.54	0.12	0.87
SSHWs200-Y	0.18	0.58	0.10	0.57	0.25	0.54	0.12	0.66	0.36	0.62	0.12	0.66

Table 5 Ratio of average story drift demands at ground story for the building models subjected to ground motion record sets

	4-story					7-story				
	Drift Demand Ratio					Drift Demand Ratio				
	A	B	C	D	Ave.	A	B	C	D	Ave.
Ref-X	1.00	1.00	1.00	1.00	1.00	1.00	1.00	1.00	1.00	1.00
Ref-Y	1.00	1.00	1.00	1.00	1.00	1.00	1.00	1.00	1.00	1.00
SSH-X	1.34	1.17	1.26	1.35	1.28	1.34	1.33	1.37	1.41	1.33
SSH-Y	1.14	1.26	1.23	1.34	1.28	1.41	1.43	1.32	1.45	1.41
SSW-X	1.60	1.59	1.55	1.63	1.58	1.24	1.21	1.22	1.25	1.23
SSW-Y	1.69	1.89	1.83	2.00	1.90	1.55	1.55	1.43	1.55	1.51
SSHW-X	1.95	1.78	1.91	2.02	1.93	1.78	1.75	1.86	1.78	1.75
SSHW-Y	2.23	2.21	2.21	2.66	2.38	2.05	2.07	2.04	2.18	2.06
Average	1.49	1.49	1.50	1.63		1.42	1.42	1.41	1.45	

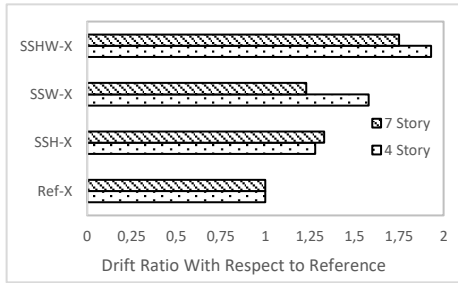


Fig. 6 Average drift demand ratios for ground story at X axis

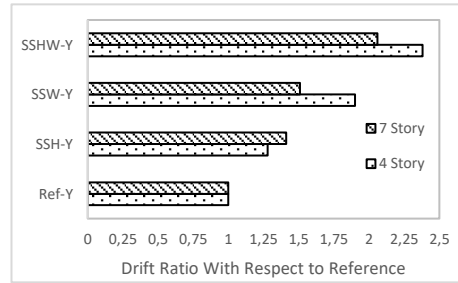


Fig. 7 Average drift demand ratios for ground story at Y axis

7. Results and Discussion

In this study, soft story behavior due to increased story height, lack of load bearing infill wall at ground story and existence of both cases are investigated using nonlinear static and dynamic response history analyses for mid-rise reinforced concrete buildings. Based on 40 nonlinear static analyses and 1328 nonlinear response history analyses the following observations are made:

- Although, transverse steel amount has limited effect on lateral strength, it significantly affects the displacement capacities (Table 3 and 4). Even though s100 and s200 models have the same yield strength, the displacement capacities of the s200 models are considerably lower (Fig. 5).
- Consideration of infill walls in the building model as diagonal struts increases the yield strength of the 4- and 7-story models by 45% and %32, respectively (Fig. 5 and Table 1). Modeling of infill walls seems to be more effective on the lateral strength of the buildings with less number of stories, because the properties of the walls are not affected by the number of stories but the floor plan. Structural elements with larger dimension and strength in the buildings with more number of stories decrease the effect of walls.
- In general, the lateral strength of the building increases, and displacement capacity decreases when infill walls are regarded as load carrying elements (Fig. 5, Table 3 and 4).
- When Table 3 is examined, it is observed that for some instances, the displacement capacities of the Soft Story due to Height and Wall (SSHW) model is higher than that of Soft Story due to Wall (SSW) ones on the contrary of the expectations. This is due to the increase in plastic hinge length, hence rotation capacity, because of increased column length at ground story (Eqn. 2). In view of the values used in the study, elongation of column length from 2.8 m to 4 m increases plastic rotation capacity of the columns by 35% on the average. Even though this increase, no such instance is encountered in the 7-story models.
- In order to determine which soft story case has the most negative effect on the displacement capacity, the ratio of the irregular model capacities to the regular ones (“/Ref” column) is considered. For Life Safety performance level: average values are 0.80 for SSH, 0.60 for SSW, 0.62 for SSHW models. Therefore, the most detrimental case for the 4-story buildings is the SSW with slight difference with SSHW due to the above explained reasons. These figures for the 7-story buildings

are, SSH: 0.75, SSW: 0.76, SSHW: 0.59. Therefore, SSHW case is the most unfavorable one (Table 3 and 4).

- SSHW case is the most unfavorable one for both 4- and 7-story buildings for Collapse Prevention level (Table 3 and 4). The average values are; SSH: 0.78, SSW: 0.76, SSHW: 0.66 for 4-story, and SSH: 0.67, SSW: 0.66, SSHW: 0.57 for 7-story, for the Collapse Prevention level.
- Soft story which is especially due to height and wall increased the story drift ratios considerably as shown in Figure 6 and 7. The demands due to soft story may increase up to 100%.
- Although there is no obvious effect of ground motion records on different soil types in story drift demands for 7-story buildings, the demands of the 4-story buildings are observed to be affected for soil type D.

After the results of this study and the studies of Arteta et al [10] , Bozyigit and Yesilce [14] are accounted, it is seen that the infill walls significantly changed the behavior of the structure. If infill walls are regarded as load carrying elements, the lateral strength of the building increases, and displacement capacity decreases as reported in Harsoor and Shreenath's study [12] and Santhi's study [13]. When the obtained displacement capacity and drift demand results are evaluated, in scope of the values considered in the study, it is observed that soft story due to increased height (SSH) and due to lack of infill walls (SSW) have close values to each other. As a result, it should be kept in mind that soft story may arise not only because of increased story height, but because of abrupt changes in amount of infill walls which are not thought to be a part of structural system. As observed in this study, soft story due to increased height and lack of infill wall at ground story (both at the same time) is the most detrimental case in view of drift capacities and demands.

Acknowledgement

The authors acknowledge support provided by Scientific and Technical Research Council of Turkey (TUBITAK) under Project No: 105M024.

References

- [1] Adalier K, Aydingun O. Structural engineering aspects of the June 27, 1998 Adana-Ceyhan (Turkey) earthquake, *Engineering Structures*, 2001; 23:343–55. [https://doi.org/10.1016/S0141-0296\(00\)00046-8](https://doi.org/10.1016/S0141-0296(00)00046-8)
- [2] Dogangun A. Performance of reinforced concrete buildings during the May 1 2003 Bingöl earthquake in Turkey, *Engineering Structures*, 2004; 26:6; 841 – 856. <https://doi.org/10.1016/j.engstruct.2004.02.005>
- [3] Kaplan H. Yilmaz S. Binici H. Yazar E. Cetinkaya N. May 1, 2003 Turkey—Bingöl Earthquake: Damage in Reinforced Concrete Structures, *Engineering Failure Analysis*, 2004; 11: 279 – 291. <https://doi.org/10.1016/j.engfailanal.2003.08.005>
- [4] Ozcebe G. Seismic assessment and rehabilitation of existing buildings. Tubitak Research Report; Report No: ICTAG YMAU I574: Ankara, Turkey, 2004.
- [5] Sezen H. Whittaker AS. Elwood KJ. Mosalam KM. Performance of reinforced concrete buildings during the August 17, 1999 Kocaeli, Turkey earthquake, and seismic design and construction practice in Turkey, *Engineering Structures*, 2003; 25:1, 103 – 114. [https://doi.org/10.1016/S0141-0296\(02\)00121-9](https://doi.org/10.1016/S0141-0296(02)00121-9)
- [6] Sucuoglu H. Yilmaz T. Duzce, Turkey: a city hit by two major earthquakes in 1999 within three months, *Seismological Research Letters*, 2001; 72:6 679 – 689. <https://doi.org/10.1785/gssrl.72.6.679>

- [7] Dolsek M. Fajfar P. Soft storey effects in uniformly infilled reinforced concrete frames, *Journal of Earthquake Engineering*, 2000; 5:1 1 – 12. <https://doi.org/10.1080/13632460109350383>
- [8] Negro P. Colombo A. Irregularities induced by nonstructural masonry panels in framed buildings, *Engineering Structures*, 1997; 19:7 576 – 585. [https://doi.org/10.1016/S0141-0296\(96\)00115-0](https://doi.org/10.1016/S0141-0296(96)00115-0)
- [9] Aşar Ö. Aksoy HB. Dolgu Duvarların Betonarme Çerçeve Davranışına Etkisinin Basitleştirilmiş Bir Yöntemle Dikkate Alınması, *Pamukkale Üniv. Müh. Bilim Derg.*, 2015; 21:3 115 – 122. [in Turkish]
- [10] Arteta CA. Carrillo J. Archbold J. Gaspar D. Pajaro C. Araujo G. Torregroza A. Bonett R. Blandon C. Fernandez-Sola LR. Correal JF. Mosalam KM. Response of Mid-Rise Reinforced Concrete Frame Buildings to the 2017 Puebla Earthquake, *Earthquake Spectra*, 2019; 35:4 1763 – 1793. <https://doi.org/10.1193/061218EQS144M>
- [11] Ozmen HB. Inel M. Strength reduction factors for existing mid-rise RC buildings for different performance levels. *Res. Eng. Struct. Mat.*, 2018; 4(4): 241-255. <https://doi.org/10.17515/resm2018.60ea3107>
- [12] Shreenath Harsoor R. Effect of infill wall on vertical irregular tall structure, *International Journal of Innovative Technology and Exploring Engineering*, 2019; 9(1): 1488-1495. <https://doi.org/10.35940/ijitee.A4303.119119>
- [13] Santhi MH. Evaluation of earthquake load resistance of masonry infilled RC frames using linear and non-linear dynamic analysis, 14th International Conference on Concrete Engineering and Technology, 2018; Kuala Lumpur; Malaysia. <https://doi.org/10.1088/1757-899X/431/12/122010>
- [14] Bozyigit B. Yesilce Y. Effects Of Infill Walls On Free Vibration Characteristics Of Multi-Storey Frames Using Dynamic Stiffness Method, *Sigma J Eng & Nat Sci*, 2019; 37:3 885 – 902. <https://doi.org/10.1002/eqe.2555>
- [15] Jeon JS., Park JH. DesRoches R. Seismic fragility of lightly reinforced concrete frames with masonry infills, *Earthquake Engng Struct. Dyn.* 2015; 44:1783 – 1803
- [16] Quayyum S. Alam MS. Rteil A. Seismic behavior of soft storey mid-rise steel frames with randomly distributed masonry infill, *Steel and Composite Structures*, 2013; 14:6 523 – 545. <https://doi.org/10.12989/scs.2013.14.6.523>
- [17] Serenaj A. Garevski M. The required ductility reduction of soft storey buildings through application of base isolation. *Res. Eng. Struct. Mat.*, 2018; 4(1): 49-60.
- [18] Turkish Earthquake Code (TEC), Specifications for buildings to be built in seismic areas, Ministry of Public Works and Settlement, Ankara, Turkey, 1975. [in Turkish]
- [19] Turkish Earthquake Code (TEC), Specifications for buildings to be built in seismic areas, Ministry of Public Works and Settlement, Ankara, Turkey, 2018. [in Turkish]
- [20] SAP2000 V-8, CSI. Integrated finite element analysis and design of structures basic analysis reference manual; Berkeley (CA, USA); Computers and Structures Inc.
- [21] Federal Emergency Management Agency (FEMA). Prestandard and Commentary for Seismic Rehabilitation of Buildings. Rep. FEMA-356, Washington D.C., USA, 2000.
- [22] Watanabe F. Behaviour of Reinforced Concrete Buildings during Hyougoken-Nanbu Earthquake, *Cement and Concrete Composites*, 1997; 19: 203 – 211. [https://doi.org/10.1016/S0958-9465\(97\)00013-9](https://doi.org/10.1016/S0958-9465(97)00013-9)
- [23] TS500, Design and Construction Specifications for Reinforced Concrete Structures, Turkish Standards Institute, Ankara, Turkey, 2000. [in Turkish]
- [24] Inel, M., Ozmen, H. B., & Bilgin, H. (2008). Re-evaluation of building damage during recent earthquakes in Turkey. *Engineering Structures*, 30(2), 412-427. <https://doi.org/10.1016/j.engstruct.2007.04.012>
- [25] Applied Technology Council (ATC). Seismic Evaluation and Retrofit of Concrete Buildings, Rep. No. ATC-40, Redwood City, California, USA, 1996.

- [26] Scott BD. Park R. Priestley MJN. Stress-strain behavior of concrete confined by overlapping hoops at low and high strain rates, *ACI Structural Journal*, 1982; 76:1 13 – 27.
- [27] Mander JB. (1984). *Seismic Design of Bridge Piers*, Ph.D. Dissertation, University of Canterbury, New Zealand.
- [28] Turkish Earthquake Code (TEC), Specifications for buildings to be built in seismic areas, Ministry of Public Works and Settlement, Ankara, Turkey, 2007. [in Turkish]
- [29] Priestley MJN. Seible F. Calvi GMS. *Seismic Design and Retrofit of Bridges*, John Wiley & Sons, New York, NY, USA, 1996. <https://doi.org/10.1002/9780470172858>
- [30] Park R. Paulay T. *Reinforced Concrete Structures*, John Wiley & Sons, New York, NY, USA, 1975. <https://doi.org/10.1002/9780470172834>
- [31] Uniform Building Code (UBC), Int. Conf. of Building Officials, Whittier, California, USA, 1997.
- [32] PEER, Pacific Earthquake Engineering Research Center, <http://peer.berkeley.edu/smcat/index.html>.



An investigation of high temperature effect on pumice aggregate light mortars with brick flour

Behçet Dündar ^a, Emriye Çınar ^{*.b}, Ahmet Necip Çalışkan ^c

Civil Engineering Department, University of Osmaniye Korkut Ata, Osmaniye, Turkey

Article Info

Article history:

Received 21 Nov 2019

Revised 10 Feb 2020

Accepted 12 Feb 2020

Keywords:

Light Mortar;

Pumice;

Brick Flour;

High Temperature

Abstract

In this study, physical and mechanical properties of pumice aggregate substituted with brick flour as mineral additive and light mortars were investigated. At the preparation of mortars, pumice (0-4mm) as a fine aggregate and CEM I 42.5R Portland Cement were used. Standard mortar mixing ratios were taken as fine aggregate/Cement/Water=3/1/0.5 and pumice aggregate is used as a fine aggregate. Brick flour, which is used as mineral additive, is substituted with 0%, 10%, 20% and 30% by weight of cement. The flow values of produced mortars were determined while they were in fresh form. Mortar samples were cured in standard cure pool for 28 days. Flexural and compressive strengths of the mortar samples which were cured for 7 days, were measured. Physical properties such as water absorption, porosity and unit volume weight of 28 days cured mortars were determined and flexural and compressive strengths were calculated. At the end of 28th day samples which were reached its final strength, were exposed to 200 °C, 400 °C, 600 °C and 800 °C heats in High Temperature Oven. With determining of flexural and compressive strengths after heating, strength loss between before and after heating was designated. It is observed that the flexural and compressive strengths were decreased with increasing the ratio of Brick Flour. At all temperatures, it is occurred that the ultrasound speed was decreased. With increasing of temperatures, ultrasound speed values were reduced.

© 2020 MIM Research Group. All rights reserved.

1. Introduction

Nowadays, to solve housing and transportation problems effectively due to population increasing and limitation of land, Highrise buildings and underground construction needs are increasing rapidly. With developing technologies, it is observed that buildings provide more comfort and qualitative service. Thanks to this technology new equipment, systems and materials such as electrical applications and gas usage, are more preferred. However, in our daily life, these preferences may be increased of the fire possibility in buildings. Fire can be caused on structure elements even though it was not a risk for life, and it can directly effect on structure safety and service life [1]. Cement is one of other binding materials which is used the most in Civil Engineering Sector. Cement consumption is increasing as well as the rapidly increasing of building sector. Although fully domestic raw materials are used in cement industry, production is negatively affected by high energy cost and due to process causes CO₂ production, this has a big role in global warming. Because of this reason, used energy of cement industry and environmental impacts are one of the constantly debated topics of both scientific and world agenda. In addition to this, rehabilitation of cement process is continued, and search of raw materials which lead to make better quality, efficient and economic cement, is ongoing [2-3]. The use of doped cements in the construction sector has become more preferable today due to the economic and technical advantages they provide, as well as the indirect benefits in reducing CO₂ emissions by reducing clinker production. Most of these

*Corresponding author: emriyecinar@osmaniye.edu.tr

^a orcid.org/0000-0003-0724-9469; ^b orcid.org/0000-0002-9435-2968; ^c orcid.org/0000-0002-9497-5209

DOI: <http://dx.doi.org/10.17515/jresm2019.163ma1121>

Res. Eng. Struct. Mat. Vol. 6 Iss. 3 (2020) 241-255

materials are mineral additives with pozzolanic properties [4]. Pozzolans; with its advantages such as economic efficiency in cement, reduction of permeability, control of alkali aggregate development, chemical resistance, lightness, utilization of wastes, reduction of drying shrinkage of concrete and increase of strength, it is added to the concrete as a direct contribution to cement or to be added to a part of cement[5]. In recent years, to provide high temperature resistance, mineral additives are used in mixtures. Fly ashes, blast furnace slag and silica fume are among them and commons [6-7]. Also it is known that pozzolanic materials provides resistance of fire to cement based materials [8]. In world history, the first produced construction material brick, is used on essential buildings through history. Brick that is produced by using clay, is mostly used construction materials thanks to its positive properties such as durability and strength, low sound and heat permeability and fire resistance [9]. Brick is widely used and produced in agricultural structures in rural areas as well as in cities due to the fact that suitable soil is abundant and this material enables cheap and easy production [10]. In Turkey, some buildings such as animal shelters and agricultural product storages are mostly built as one story and by using prefabricated materials. Brick is the one of these prefabricated materials and commonly used [11-12]. Brick flour is one of the pozzolanic additives added to both mortar and concrete. Increasing the production of brick in industry, has brought many problems with itself. Important one of these problems is remained product waste after production. Breaks occur during brick production and transportation and these broken bricks are separated as waste [13]. To remove out brick wastes outside causes harming on efficient farm areas and negative impact on country economy. Moreover, it takes thousand years.to recover these harmed farm areas itself and this leads disruption of ecological balance on soil [14]. Investigations and researches show that brick waste consists %10 of total production [15]. Researches are done in many countries for how to use these product wastes due to increasing of production wastes. By reducing the amount of waste materials, the main materials are tried to be minimized by substituting the main materials for environmental damage. Thus, natural resources will be better used and environmental pollution will be reduced with the use of waste materials [16]. The reason for the loss of strength at high temperatures is the decomposition of hydration products. The researchers stated that the decomposition of the cemented matrix started above 105 ° C. The first step of chemical and physical separation is to release water in the pores and chemically bound water in the structure of calcium silicate hydrate (C-S-H) gels. This process is called dehydration [17]. In this step, other hydrates and ettringite also begin to decompose. Also, depending on the origin and type, aggregates may begin to be affected [18]. At about 300-400 ° C, the chemically bonded intermediate layer water in the C-S-H gel evaporates. In addition, the first microfractures begin to appear in Ca (OH) 2 and anhydrite cement regions [19]. At this stage Ca (OH) 2 decomposes into CaO and H2O. In the heating step, the decomposition of Ca (OH) 2 is not a critical reaction in terms of power. In the cooling process, however, CaO can be rehydrated to Ca (OH) 2 and this rehydration produces a significant volume expansion of about 44% [20-21]. At 500-600 ° C, the carbonates begin to decompose and are known to cause irreversible damage to concrete. This is because an important part of the main binder phase of concrete, namely C-S-H gels, is decomposed. In general, above 800 ° C, almost all constituents of concrete break down, leading to significant strength and weight loss [22]. As the thermal properties of cement paste and aggregates are not exactly the same, it creates internal stresses and generally results in cracking [23]. The use of mineral admixtures has been investigated in order to increase the durability of cement-based materials both in the evaluation of waste products and in the face of a fire disaster that may be encountered at any time. In addition to the usual mineral additives, the usability of Brick Flour in mortar samples was investigated and the effect of physical and mechanical properties on mortar properties were investigated. In this study, pumice aggregate mortar samples were produced by replacing 10%, 20% and 30% by weight of brick flour to cement. The produced mortar samples were removed from the mold after 24 hours and left to stand in the curing pool. Fresh processability of mortar samples, 7 and 28 days bending and compressive strength tests,

ultrasound, water absorption, porosity, unit volume weight and high temperature tests were performed. The mortar samples, which were filled for 28 days, were kept at 200 °C, 400 °C, 600 °C and 800 °C for one hour while high temperature test was performed. After the 0%, 10%, 20%, 30% Brick Flour samples were removed from the high temperature furnace, bending and pressure values, water absorption, porosity, unit volume weight tests were performed and the data were taken.

2. Experimental Studies

2.1. Used Materials

Cement is one of the mortar components, is taken from ÇİMSA cement factory as CEM I 42.5 R type and produced according to TS EN 197-1 [24]. Chemical analysis of used cement is taken from producer cement factory and physical and chemical properties were given in Table 1.

Table 1 Physical and Chemical properties of CEM I 42.5 R type cement and Brick Flour

Chemical Analysis (%)	CEM I 42.5R	BF
CaO (%)	64.7	3.50
SiO ₂ (%)	20.7	58.50
Al ₂ O ₃ (%)	5.55	16.50
Fe ₂ O ₃ (%)	2.9	8.00
MgO (%)	2.68	0.15
SO ₃ (%)	2.76	0.00
Na ₂ O (%)	0,25	1.00
K ₂ O (%)	0,46	2.41
Loss on ignition (%)	3.26	-
Fineness (m ² /kg)	31020	29700
Volume Expansion (mm)	1	-
Beginning of Set (min)	260	-
Ending of Set (min)	300	-

In the experimental study, city network water of Osmaniye province complying with TS EN 1008 was used in the mixture of mortar samples produced [25]. pumice deposits in Turkey are concentrated in Urgup Avanos and Kayseri's Talas-Tomarza-Devel and Osmaniye. It contains numerous pores from the macro scale to the micro scale due to the sudden release of the gases during pumice formation and sudden cooling. As the pores are generally unconnected, they are lightweight, can swim for a long time in water, have low permeability and have high insulation. It has a chemical content of up to 75% silica. The SiO₂ content of the rock gives the rock abrasive properties. Al₂O₃ composition gives high resistance to fire and heat [26]. Pumice which is used to produce mortar is given in Fig. 1, is obtained from Osmaniye province Toprakkale district Tüysüz municipality.



Fig. 1 Osmaniye Pumice

Chemical analysis of maximum 4 mm grain diameter Pumice Aggregate, is given in Table 2.

Table 2 Chemical analysis of used Pumice

Composition	Average
SiO	45.95
Al ₂ O	19.95
Fe ₂ O	7.53
CaO	13.23
MgO	6.24
Na ₂ O+K: O	6.69
Other	0.41
Total	100.00

In this study, firstly standard brick is formed to 4mm size by using crusher then by using ringed grinder, 4mm sized brick is formed to 24-40 μ and brick flour was used as mineral additive and given in Fig. 2.



Fig. 2 Brick Flour

Inside brick, there is no chemical material which can harm human health or environment. Therefore some bricks which is damaged during the process of production or transportation, are grinded and used for floor elements, tennis courts, park walking ways, bicycle roads and garden arrangements.

2.2. Sample Production

In this study, 4 pumice aggregate samples are produced by adding brick flour to cement by weight of 10%, 20%, 30%. In mixtures, pumice is used as a fine aggregate then mixtures are waited for 24 hours in 40x40x160mm molds according to TS EN 13369 (2018) rules. After that molds are placed in curing pool. Flexural and compression tests are applied on 7th and 28th days samples. Reference sample is produced by only cement, aggregate and water without brick flour [29]. Materials that are used in experiment are given in Table 3.

Table 3 Materials and Sample names and weights in Experiment (gr)

Sample Name	Explanation	Aggregate	Water	Cement	Brick Flour
BF0	Reference	850	250	450	0
BF10	%10 BF added mortar	850	250	405	45
BF20	%20 BF added mortar	850	250	360	90
BF30	%30 BF added mortar	850	250	315	135

Spread values for each mixture were measured on the Flow Table of the mixtures. After the spread values were taken, the lubricated molds were placed on the cement shaking table and concrete mortar was poured into the molds in two stages [30].

2.3. Flow-Table Test

Flow-Table Test is carried out to determine the consistency and spread value of fresh mortar immediately after mixing of mineral binder and dense (normal) aggregate or light aggregates. The fresh mortar placed in the mold used in the test is taken by slowly pulling the mold vertically upwards in the test stage and the mass of the mortar remaining on the circular plate is fell to 15 times at a constant frequency and approximately 15 times per second. Flow-Table Test was applied to fresh mortar samples according to TS EN 1015-3 (2010) standard [31].

2.4. Water Absorption and Porosity Tests

Porosity and water absorption properties were determined by using Archimedes principle scales on all series. At the end of 28 days, the concretes were removed from the curing pool and put into the basket in the scale and the data were recorded by means of Archimedes Scales. The surfaces were then dried with a cloth and their weights in the air were taken. Samples were dried in oven at 110 °C for 24 hours. The samples from the oven were cooled until samples reaches room temperature and then the oven dry weights were weighed. Weight measurements were made on 3 samples for each series and their mean values were recorded [32].

2.5. Compressive and Flexural Tests

In all series, after 24 hours, it was cured for 7 and 28 days under standard curing conditions. Samples with high temperature applied and not applied after curing were subjected to bending and pressure tests with the device in Fig. 3 with the help of the device in Fig. 3 manufactured by Baz Makina with the capacity of 200 tons according to the Turkish standard [33]. In the study, TS EN 196-1 standard was used for determination of flexural-compressive strengths. Flexural-compressive determination of cements was carried out on 40x40x160 mm specimens in accordance with TS EN 196-1 as shown in Fig. 4 [34].



Fig. 4 Flexural and Compressive Strength Device

2.6. Ultrasound Test

The ultrasound pulse velocity measurements of the samples were made with the ultrasound test device (P-wave) in Fig. 5. The samples were kept in standard curing pool for 28 days and oven dried, ultrasound test was applied. The distance between the two surfaces of the samples was measured with the help of a calliper rule, and the surfaces to be measured were smooth with the ultrasound gel in order to avoid air gap. The sample was placed between the probes (donor-receiver) and aligned and the device was started. The transition time of the sound wave in the device is recorded. By using the intermediate distance between the probes and the sound transition velocity we recorded, ultrasound transition velocities were calculated by making the necessary calculations in the formula. The ultrasound test samples were then placed in a high temperature furnace and then stored at 200 °C, 400 °C, 600 °C and 800 °C temperatures according to standards [35].



Fig. 5 Ultrasound test device

2.7. Application of High Temperature on Samples

High temperature application was carried out in accordance with the principles specified in TS EN 13501-1 (2013) standard. According to the standards, the actual fire environment is between 20 - 1000 °C and occurs within 15 - 300 minutes. The average temperature increase rate corresponds to 27.4 °C / min. However, it is not possible to increase the heat increase rate to 27.4 °C / min in such a short time for resistance furnaces. The mortar samples were applied at 200 °C, 400 °C, 600 °C and 800 °C at a temperature of 10 °C / min in a laboratory oven with a capacity of 1800 °C and kept in the oven for 60 minutes at all temperatures. Samples were

then allowed to cool to the temperature of the laboratory conditions. The samples subjected to high temperatures were re-tested after bending, pressure and ultrasound after cooling [36].

3. Results and Discussion

3.1 Flow Test

Flow values of samples that were produced for experimental study, were given in Table 4. It is observed that with increasing of Brick Flour ratio, flow values decreased. Also, with increasing the use of Brick Flour ratio, it is observed that workability is decreased.

Table 4 Flow values of fresh state mortar samples

Sample Name	Flow Values (cm)
%0 BF	14.0
%10 BF	14.0
%20 BF	13.5
%30 BF	13.0

3.2 Porosity, Water Absorption and Weight per Unit of Volume

Experimental results of samples that are produced for study, were given in Fig. 6. According to these results below, maximum it is found that 20% BF sample has the maximum porosity as 25%. In comparison with Reference sample, it is observed that porosity has increased by 10%.

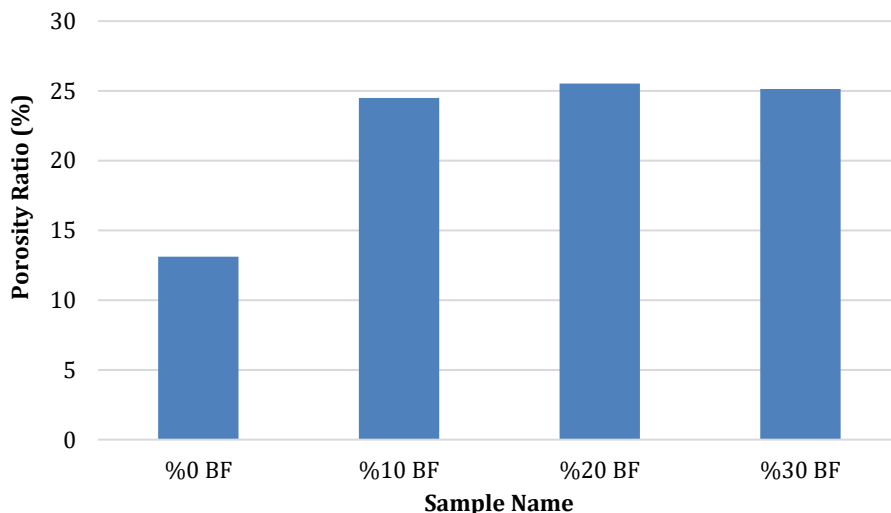


Fig. 6 Experimental Porosity Results

Water absorption ratios of samples that are cured for 28 days, are given in Fig. 7 as graph. When this graph is analysed, it is observed that 20%BF samples has the maximum water absorption ratio as 14.30%. In all series it is observed that with adding brick flour into cement, water absorption ratios were increased compare to reference sample.

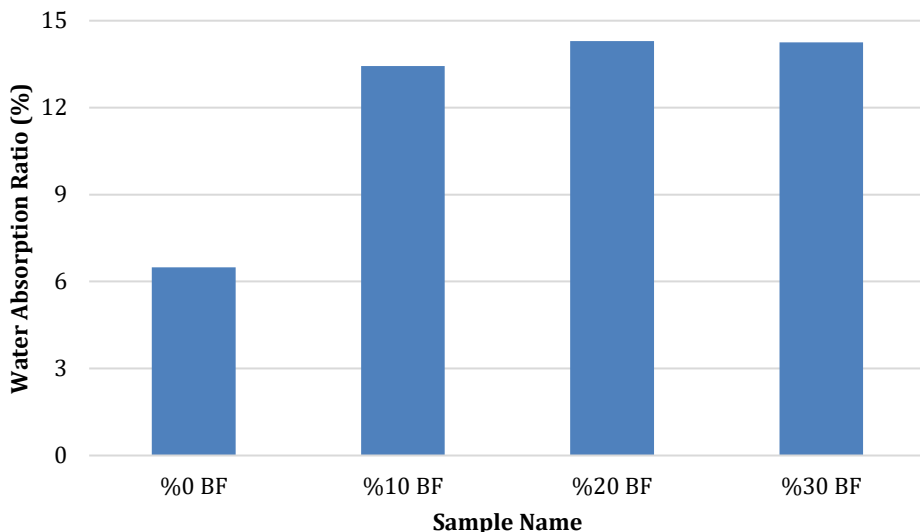


Fig. 7 Experimental Water Absorption Results

The relationship between porosity and water absorption is given in Fig. 8. The correlation coefficient between water absorption and porosity was found as $R^2 = 0.9981$. From this result, it was determined that a strong relationship between these two physical properties.

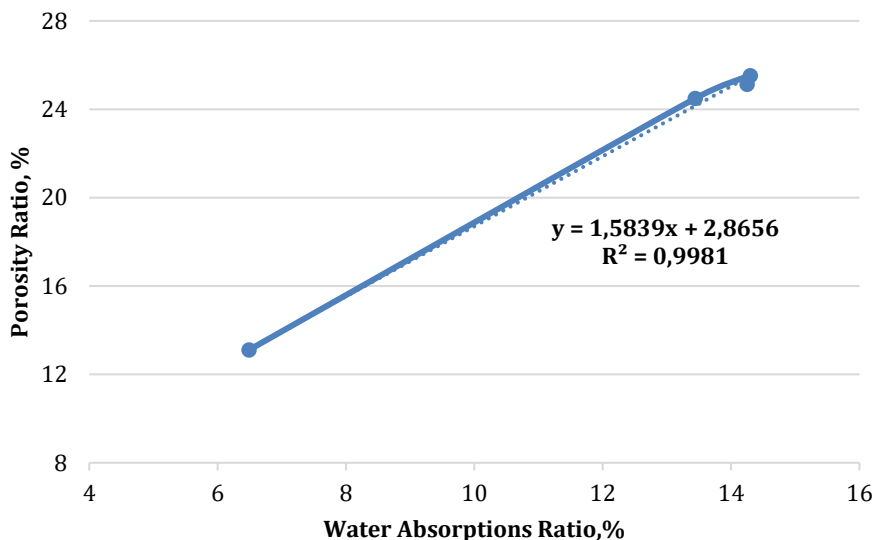


Fig. 8 The relationship between porosity and water absorption

Weight per unit of volume tests were done on produced samples and test results were shown in Fig. 9. According to these results, it is observed that the weight per unit of volume of samples has decreased with adding brick flour. In 20% BF sample unit volume weight was 1.78 gr/cm³ while it was 2.02 gr/cm³ in reference sample.

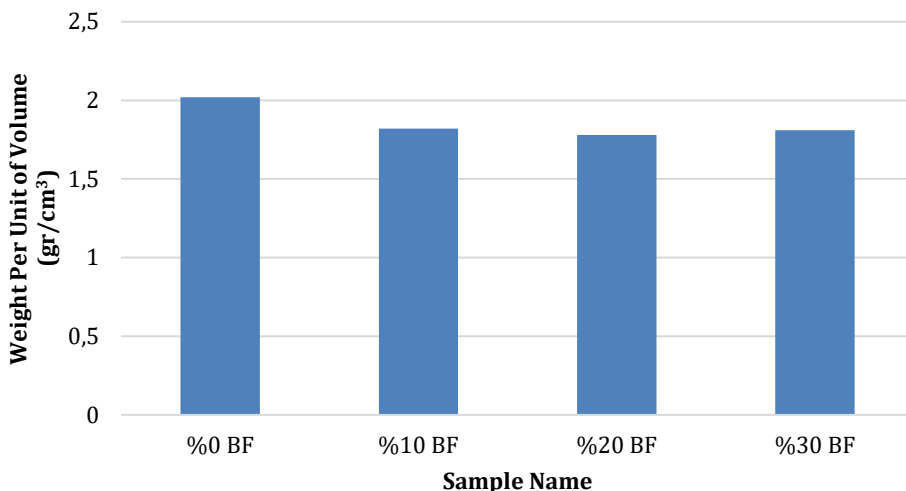


Fig. 9 Weight Per Unit of Volume Experimental Results

3.3 Flexural and Compressive Strength

7- and 28-days flexural strength test results are given in Fig. 10, is applied on produced samples. When these results are investigated, it is observed that flexural strength value in 10% BF sample is more than reference sample. Flexural Strength has increased up to 10% added BF however, it was observed that Flexural Strength was decreased at 20%BF and 30%BF added samples due to increasing of fine material amount. Also, increasing of fine material causes surface area. This situation leads mortar placement problems. It is found that on 7th day reference sample compressive strength was 4.72 MPa while 10%, 20%, 30% Brick Flour added samples were 5.83, 5.22 and 5.16 MPa respectively. While the 28 day pressure value of the reference sample was 6 MPa, these values were found to be 6.52, 6.05 and 5.73 MPa in the samples which were replaced with 10%, 20%, 30% cement and brick flour. When the compressive strength values of all series were examined, it was observed that the maximum value was in the substituted sample of 10% brick and the minimum value in the substituted sample of 30%.

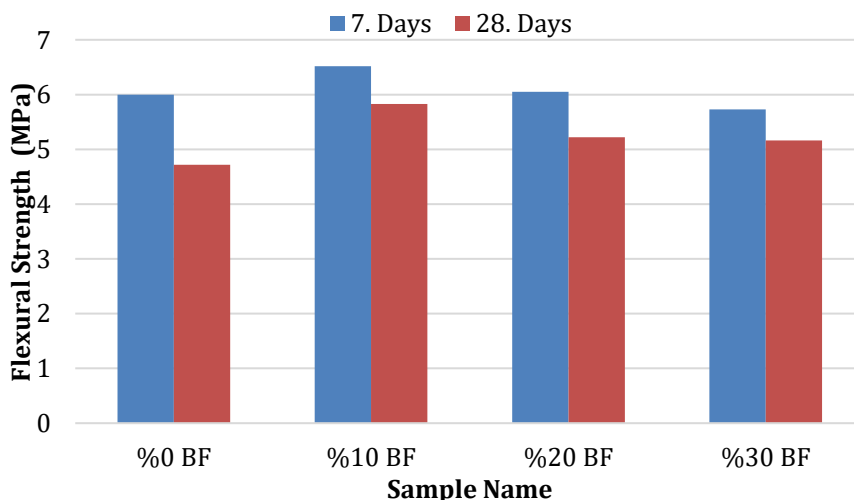


Fig. 10 Flexural Strength Values

Samples were applied to Flexural Strength Test before and after high temperature application. Test results were given in Fig. 11. It is observed that after high temperature application on samples, strengths were decreased. Also increasing with temperature value causes further sample strength decline.

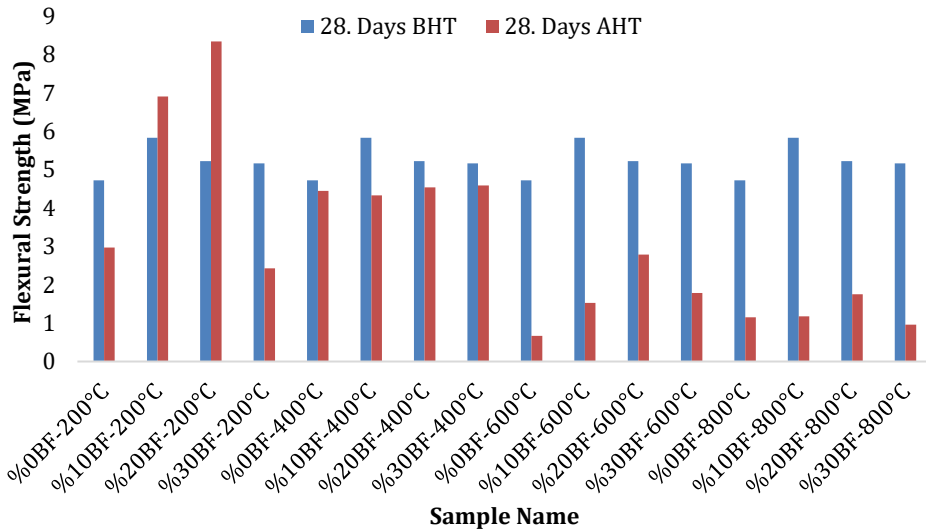


Fig. 11 Flexural Strength Before and After High Temperature Application

7 and 28 days compressive test results are given in Fig. 12, is applied on produced samples. When these results are investigated, it is observed that compressive strength of Brick Flour added is more than reference sample. It is found that on 7th day reference sample compressive strength was 35.58 MPa while 10%, 20%, 30% Brick Flour added samples were 34.68, 31.14 and 28.78 MPa respectively. While the 28 day pressure value of the reference sample was 45.56 MPa, these values were found to be 53.03, 46.51 and 39.53 MPa in the samples which were replaced with 10%, 20%, 30% cement and brick flour. When the compressive strength values of all series were examined, it was observed that the maximum value was in the substituted sample of 10% brick and the minimum value in the substituted sample of 30%.

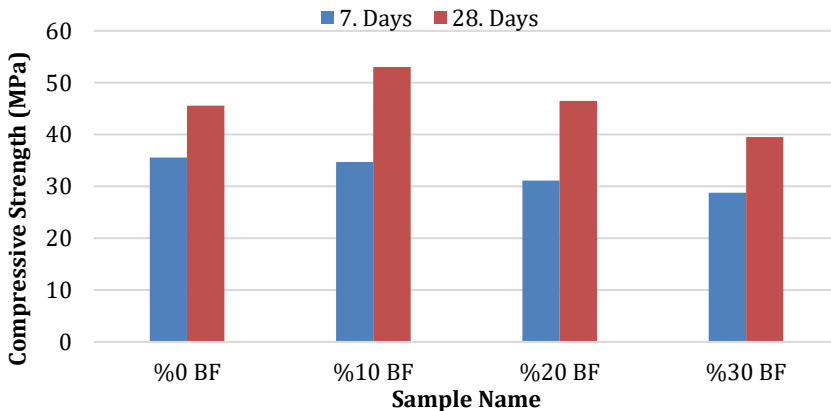


Fig. 12 Compressive Strength Experimental Results

Samples were applied to Compressive Strength Test before and after high temperature application. Test results were given in Fig. 13. It is observed that after high temperature application on samples, compressive strengths were decreased. Also increasing with temperature value causes further sample compressive strength decline.

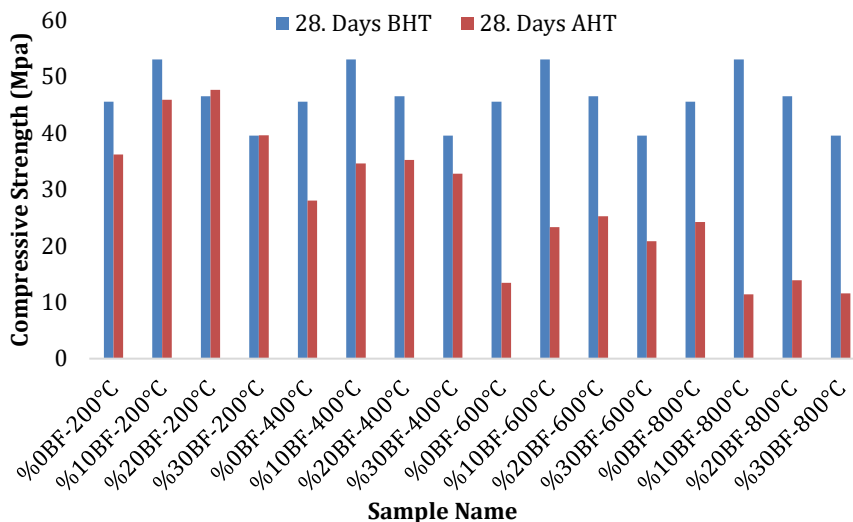
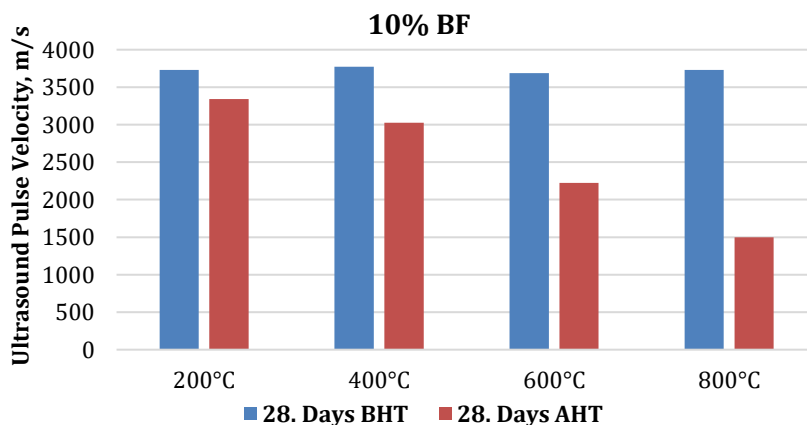


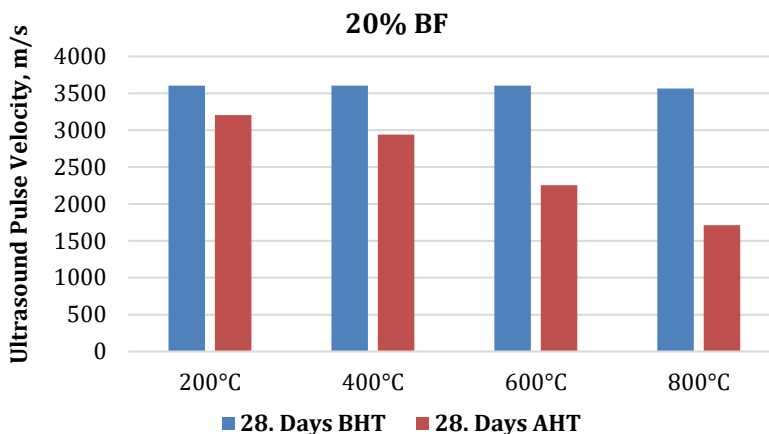
Fig. 13 Compressive Strength Before and After High Temperature Application

3.4 Ultrasound Pulse Velocity

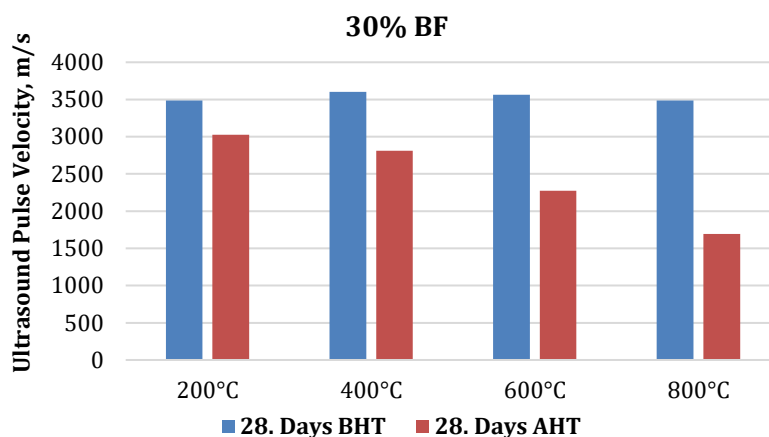
The results of ultrasound before and after temperature according to the ratio of each brick flour are given in Fig. 14. When the effect of temperature on Ultrasound Pulse Velocity is investigated, it is observed that Ultrasound Pulse Velocity was decreased at all temperatures for all samples. With increasing temperature Ultrasound Pulse Velocity values were decreased. Due to Brick Flour is a fine material, it makes filling effect. Increases the surface area when the brick flour is substituted, increases the binding demand of the sample. With increasing demand, binding material is insufficient. This leads a cavities structure. Ultrasound Pulse Velocity was decreased with strength declining. The velocity of the ultrasound passage was reduced due to the explosion of capillary cracks in the sample with a significant proportion of temperature.



(a)



(b)



(c)

Fig. 14 Ultrasound Values After High Temperature Application of Mortar Samples, a;10%BF, b;20%BF, c;30%BF

4. Conclusions

In this experimental and numerical study; physical and mechanical properties of pumice aggregate substituted with brick flour as mineral additive and light mortars were investigated. From the results of this study, the following conclusions can be drawn:

- When the flow values are investigated, it is observed that flow values were decreased with increasing BF ratio. This causes decreasing of workability.
- For mortar porosity values, it is found that 20% BF added mortar has the maximum porosity as 25%. There was 10% increase in comparison to reference sample.
- In all sample series, water absorption ratio was increased as a result of adding Brick Flour and cement into mixture.

- According to these results, weight per unit of volumes were decreased as a result of adding Brick Flour into mixture. The weight per unit of volume was 2.02 g/cm³ in the reference sample and 20% brick flour added sample was reduced to 1.78 g/cm³.
- When these results were investigated, it is observed that 10% BF added sample has more flexural strength in comparison to reference sample. At the end of the 28th day, according to reference 10% brick flour added sample showed the maximum increase in comparison to other samples.
- All series showed that flexural strength decrease after High Temperature Application, in comparison with reference sample. It is observed that with increasing temperature decreases flexural strength of samples.
- When the results were examined, it was found that the compressive strength was 10% higher than the reference sample. The 7-day pressure value of the reference sample was 35.58 MPa, while the values of 10%, 20%, 30% cement and brick flour added samples were 34.68, 31.14 and 28.78 MPa, respectively.
- While the 28-day pressure value of the reference sample was 45.56 MPa, these values were found to be 53.03, 46.51 and 39.53 MPa in the samples with 10%, 20%, 30% cement and brick flour added respectively. When the compressive strength values of all series were examined, it was observed that the maximum value was in the sample with 10% brick flour added and in the sample with 30% brick flour added, this value decreased to 39.53 MPa.
- It is observed that Post-High temperature application compressive strengths were decreased compared to the reference sample.
- The results and recommendations obtained from this study, in which the addition of brick flour in cement mortar by weight and then its effect on the strength after high temperature, are listed below:
 1. In the production of cement mortar, it is considered that the use of brick flour as a mineral additive will be suitable in terms of providing economic contribution by evaluating the wastes and reducing the consumption of cement which is an expensive material.
 2. Brick flour that used in this study has been found to be usable in the production of admixture cement within the standards. 10% admixture cement has a positive effect on strength after 7 and 28 days. This rate is around 5%.

References

- [1] W. Wang, C. Lu, Y. Li, Q. Li, An investigation on thermal conductivity of fly ash concrete after elevated temperature exposure, *Constr. Build. Mater.* 2017; 148-157. <https://doi.org/10.1016/j.conbuildmat.2017.05.068>
- [2] Yıldırım, E. Çorum'da Kullanılan Tuğla Atıklarının Tekrar Değerlendirilmesinin Araştırılması, Gazi Üniversitesi, Fen Bilimleri Enstitüsü, Yüksek Lisans Tezi, 2001; 78-83s, Ankara.
- [3] Yılmaz, B. Na-CMC Polielektrolik İlavésinin Puzolanlı Çimento Özelliklerine Etkisi. Dumlupınar Üniversitesi, Fen Bilimleri Enstitüsü Dergisi, 2006; 11, 143- 154.
- [4] Kırgız, M.S. Mermer ve Tuğla Endüstrisi Atıklarının Çimento Üretiminde Mineralojik Katkı Olarak Kullanılması. Gazi Üniversitesi, Fen Bilimleri Enstitüsü, Doktora Tezi, 2007; 228s, Ankara.
- [5] Hansen TC. Recycling of demolished concrete and masonry. London: E&FN SPON; 1992.

- [6] A.H. Akca, N. Özyurt, Effects of re-curing on microstructure of concrete after high temperature exposure, *Constr. Build. Mater.* 2018; 168, 431-441. <https://doi.org/10.1016/j.conbuildmat.2018.02.122>
- [7] X. Liang, C. Wu, Y. Su, Z. Chen, Z. Li, Development of ultra-high-performance concrete with high fire resistance, *Constr. Build. Mater.* 2018; 179, 400-412. <https://doi.org/10.1016/j.conbuildmat.2018.05.241>
- [8] I. Yüksel, R. Siddique, Ö. Özkan, Influence of high temperature on the properties of concrete made by industrial by-products as fine aggregate replacement, *Constr. Build. Mater.* 2011; 25 (2) 967-972. <https://doi.org/10.1016/j.conbuildmat.2010.06.085>
- [9] Çelik, K., (2005). Uçucu Kül, Yüksek Fırın Cürufu ve Traslı Çimentolarla Üretilen Aynı Mukavemet Sınıfındaki Harçların Dayanım ve Dayanıklılığının İncelenmesi. İstanbul Üniversitesi, Fen Bilimleri Enstitüsü, Yüksek Lisans Tezi, 62s, İstanbul.
- [10] Yetgin, Ş. ve Çavdar A., (2005). Doğal Puzolan katkı Oranının Çimentonun Dayanım, İşlenebilirlik, Katılma ve Hacim Genleşmesi Özelliklerine Etkisi. Fırat Üniversitesi Fen ve Mühendislik Bilimleri Dergisi, 17 (4), 687-692.
- [11] Dalkılıç, S., (2014). Tuğla Tozu Katkılı Harçlarda Donatı Korozyonunun Araştırılması. Süleyman Demirel Üniversitesi, Fen Bilimleri Enstitüsü, Yüksek Lisans Tezi, 2-15s
- [12] Görçiz, G. "Ülkemizde Tuğla ve Kiremit Endüstrisi", 2000'li Yıllarda Sağlıklı ve Güvenli Konutlar için Tuğla-Kiremit Paneli, TUKDER, Ankara, Ocak, 2000.
- [13] Aksin, E., (2007). Endüstriyel Atıklarının Tuğla ve Kiremit Üretiminde Değerlendirilmesi. Dokuz Eylül Üniversitesi, Fen Bilimleri Enstitüsü, Yüksek Lisans Tezi, 89s, İzmir.
- [14] Bıyık, M., (2007). BaCO₃ ve SrCO₃ Katkısıyla Tuğla Üretiminde Çiçeklenmenin Giderilmesi. Afyon Kocatepe Üniversitesi, Fen Bilimleri Enstitüsü., Yüksek Lisans Tezi, 155s, Afyonkarahisar.
- [15] Şahin, Ş.E., (2008). Ham ve Kalsine Kolemanit Atıklarının Tuğla Yapımında Kullanım Olanaklarının Araştırılması. Dumlupınar Üniversitesi, Fen Bilimleri Enstitüsü, Yüksek Lisans Tezi, 79s, Kütahya.
- [16] Çakar, B., (2009). Esnek Üst Yapılarda Tuğla Kırığı Atıkları Kullanımının Deneysel Olarak İrdelenmesi, Yüksek Lisans Tezi, Eskişehir Osmangazi Üniversitesi, Fen Bilimleri Enstitüsü, İnşaat Mühendisliği Anabilim Dalı, Eskişehir.
- [17] O. Arioğ, Effects of elevated temperatures on properties of concrete, *Fire Saf. J.* 2007; 42 (8), 516-522. <https://doi.org/10.1016/j.firesaf.2007.01.003>
- [18] D. Gavin, F. Pesavento, A. Schrefler, Modelling of deformations of high strength concrete at elevated temperatures, *Mater. Struct.* 2004; 37 (4), 218-236. <https://doi.org/10.1007/BF02480631>
- [19] S. Aydın, B. Baradan, Effect of pumice and fly ash incorporation on high temperature resistance of cement-based mortars, *Cem. Concr. Res.* 2007; 37, 988-995. <https://doi.org/10.1016/j.cemconres.2007.02.005>
- [20] W.M. Lin, T.D. Lin, L.J. Powers, Microstructures of fire-damaged concrete, *ACI Mater. J.* 1996; 93 (3), 199-205. <https://doi.org/10.14359/9803>
- [21] A. Mendes, J.G. Sanjayan, F. Collins, Effects of slag and cooling method on the progressive deterioration of concrete after exposure to elevated temperatures as in a fire event, *Mater. Struct.* 2011; 44, 709-718. <https://doi.org/10.1617/s11527-010-9660-2>
- [22] D.N. Crook, M.J. Murray, Regain of strength after firing of concrete, *Mag. Concr. Res.* 1970; 22 (72), 149-154. <https://doi.org/10.1680/mac.1970.22.72.149>
- [23] Y.F. Fu, Y.L. Wong, C.A. Tang, C.S. Poon, Thermal induced stress and associated cracking in cement-based composite at elevated temperatures - Part II: Thermal cracking around multiple inclusions, *Cem. Concr. Compos.* 2004; 26 (2), 99-111. [https://doi.org/10.1016/S0958-9465\(03\)00086-6](https://doi.org/10.1016/S0958-9465(03)00086-6)
- [24] TS EN 197-1, (2012). Cement- Stage 1: General cements - component, TSE, Ankara Turkey. using the orthogonal design method, *Constr. Build. Mater.* 2012; 31, 289-293 <https://doi.org/10.1016/j.conbuildmat.2012.01.002>

- [25] TS EN 1008, (2003). Beton-Karma suyu-Numune alma, deneyler ve beton endüstrisindeki işlemlerden geri kazanılan su dahil, suyun, beton karma suyu olarak uygunluğunun tayini kuralları TSE, Ankara Turkey.
- [26] Yaşar, E.& Erdoğan Y. 2005; Asidik (Nevşehir) ve Bazik (Osmaniye) Pomzuların Yapı Sektöründe Değerlendirilmesi, 409,413 s.
- [27] Khalaf, F.M. and DeVenny, A.S., 2004, Recycling of demolished masonry rubble as coarse aggregate in concrete: review, Journal of Materials in Civil Engineering, 16, 4, 33-340 [28] Z. Ge, Z. Gao, R. Sun, L. Zheng, Mix design of concrete with recycled clay-brickpowder. [https://doi.org/10.1061/\(ASCE\)0899-1561\(2004\)16:4\(331\)](https://doi.org/10.1061/(ASCE)0899-1561(2004)16:4(331))
- [29] TS EN 13369, (2018). Öndökümlü beton mamuller- Genel kurallar TSE, Ankara Turkey,
- [30] TS EN 1015-3, (2000). Kagir harcı-Deney metotları- Bölüm 3: Taze harç kıvamının tayini TSE, Ankara Turkey,
- [31] TS EN 1015-3, (2000). Kagir harcı-Deney metotları- Bölüm 3: Taze harç kıvamının tayini TSE, Ankara Turkey,
- [32] TS EN 1170-6, (1999). Ön yapımlı beton mamuller-Cam elyaf takviyeli çimento (ctc) deney metodu-Bölüm 6: Suya daldırma yoluyla su emme ve kuru yoğunluk tayini TSE, Ankara Turkey ,
- [33] TS EN 12390-4, (2002). Beton-Sertleşmiş beton deneyleri-Bölüm 4: Basınç dayanım Deney makinelerinin özellikleri TSE, Ankara Turkey.
- [34] TS EN 196-1, (2016). Çimento deney metotları-Bölüm 1: Dayanım tayini TSE, Ankara Turkey,
- [35] TS EN 12504-4 (2004). Beton deneyleri-Bölüm 4: Ultrases geçiş hızının tayini TSE, Ankara Turkey.
- [36] TS EN 13501-1+A1, (2013). Yapı mamulleri ve yapı elemanları, yangın sınıflandırması bölüm 1: Yangın karşısındaki davranış deneylerinden elde edilen veriler kullanılarak sınıflandırma TSE, Ankara Turkey.

Blank Page



Research Article

Tuning the properties of silica aerogels through pH controlled sol-gel processes

Fatoş Koç^a, Selay Sert Çok^b, Nilay Gizli^c

Department of Chemical Engineering, Ege University, Turkey

Article Info

Abstract

Article history:

Received 03 Dec 2019

Revised 15 Feb 2020

Accepted 25 Feb 2020

Keywords:

*Silica aerogel;
Sol-gel reactions;
pH effect;
Monolithic structure*

In this study, silica aerogels were produced by two-step sol-gel method to investigate the effect of pH on the physical, chemical and textural structure of aerogels. Tetraethyl orthosilicate (TEOS) used as a silica source. (3-aminopropyl) triethoxysilane (APTES) acted as a silica co-precursor. The quantity of sol precursors kept constant through the experiments and the pH of hydrolysis and condensation reactions were varied. As a result of the experimental studies, the optimum pH values to achieve monolithic aerogel were obtained when the pH of hydrolysis is 3 and the pH of condensation is 10. Physical, chemical and morphological characteristics of the samples were examined by performing FTIR and SEM and density analyses. Results showed that the sample SG-pH3/7 had also well-defined porous structure with homogenous pore distribution, a stable lightweight and monolithic form.

© 2020 MIM Research Group. All rights reserved.

1. Introduction

Silica aerogels are nano-structured materials with high porosity (80% - 95%), high surface area (500-1200 m²/g), low thermal conductivity, very low density (0.03-0.5 g/cm³) and very low dielectric constant (1-8). Silica aerogels are used mainly as thermal and acoustic insulators, catalyst carrier, adsorbent in separation processes, sensor in electronic industry, carrier material in pharmaceutical and agriculture, or as filler material in composite production (2,8,9).

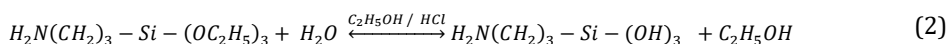
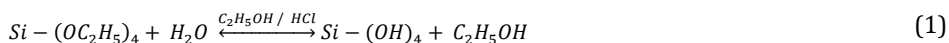
The silica aerogels are mainly synthesized via the traditional sol-gel method. Sol-gel method is generally preferred due to its ease of application in laboratory conditions. Sol-gel reaction is usually based on subsequent hydrolysis and condensation reactions of a sol precursor followed by an aging and a drying period. A general sol-gel process is outlined in Figure 1. This process consists of simultaneous hydrolysis and condensation reactions of a silicon alkoxide group in a liquid solvent with proper acid and/or base catalysis to form a colloidal solution called "sol". Gelation starts because of a condensation reaction, which creates siloxane bridges (Si-O-Si) between Si atoms delivered by precursor molecules that leads to three-dimensional (3D) open network structure. During the gelation, polymeric structure becomes distinct and viscosity of the sol increases (10-13). After complete gelation, the wet gel should be allowed to age over a period of time for the mechanical enhancement of the three-dimensional silica network. At the final step, aged gels are dried by several drying methods to remove the solvents from the pores and to obtain silica aerogels with three-dimensional porous network (14,15). Gel shrinkage, which is one of

*Corresponding author: fatoskoc@outlook.com

^a orcid.org/0000-0002-2996-110X; ^b orcid.org/0000-0001-7595-2151; ^c orcid.org/0000-0002-7591-1365;
DOI: <http://dx.doi.org/10.17515/resm2019.166ma1203>

the major drawbacks in obtaining monolithic silica aerogel, generally causes from organic solvent evaporation during the aging period. It can be avoided by replacing organic solvent with some other solvent that has a lower vapor pressure. Ionic liquids are organic salts with an extremely low vapor pressure over a large temperature range (-96 to 400 °C), hence, they do not evaporate during long aging periods (19). For that reason, including ionic liquids in the sol-gel reactions may yield a stable gel network and can preserve the structure against gel shrinkage. On the other hand, adding an amine containing silica source can be a good approach in satisfying the silica network in the process. Yang et al. prepared a silica aerogel by following a two-step method in which a silica co-precursor containing an amine group 3-aminopropyltriethoxysilane (APTES) was involved to the sol. They reported that amine-rich APTES behaved like both a basic catalyst and additional silica source and enhance the solid network (16).

Hydrolysis reactions can take place as follows:



Condensation reaction took place as follows:

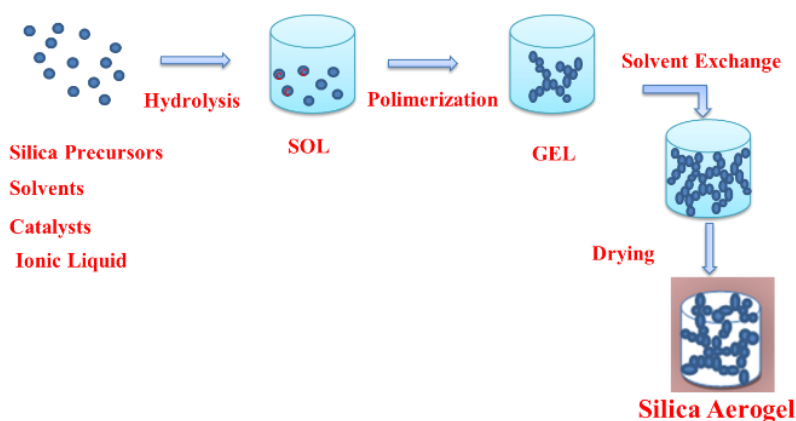
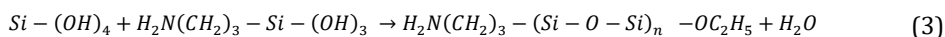


Fig. 1 Schematic presentation of sol-gel process.

The silica aerogels can be produced in various forms (i.e. powders, granular, or monolithic) according to specific target and altering the final form of these materials is possible only by changing the synthesis conditions. Producing silica aerogels in monolithic form has some advantages for particular applications as it allows controlling final shape of the product and has some superior physical properties (i.e. lower thermal conductivity) than the other forms. During the sol-gel method, any process parameters such as composition of the sol, reaction temperature, reaction pH, type of catalysts, drying conditions etc. have great importance on the final chemical, physical and morphological properties of the product. Among these parameters, pH value of the solutions in sol-gel reactions are of the essence on the formation of the 3D structural network and the final physical form of the aerogels (17-19). It directly affects the rates of the hydrolysis and

condensations reactions and the rates of these reactions are vital factors in achieving desired properties of aerogels.

During the sol-gel reaction, hydrolysis and condensation reactions take place simultaneously with different rates. When the sol is converted into a gel, the general variation of the hydrolysis and condensation reaction rates according to pH of the solution is shown in Figure 2. As seen from the Figure 2, the selected pH values can change the rates of these reactions and accelerating, or decelerating rate of these reactions completely change the reaction kinetics. The pH is a key parameter to control the microstructure of gels forming from the sol. The rate of hydrolysis and condensation reactions strongly depends on the acidity of the reaction media. Thus, reactions under acidic or basic conditions must be studied separately. The minimum reaction rate for hydrolysis is at pH 7 and for condensation at around pH 4-5. At pH lower than 5, hydrolysis reaction is favored, and condensation is the rate-limiting step. In this pH range, lots of monomers or small oligomers with reactive Si-OH groups are formed simultaneously. On the contrary, hydrolysis reaction becomes the rate-limiting step at pH higher than 5, and hydrolyzed species are instantly formed due to the faster condensation.

When pH range is between 4-7, the reaction rate of condensation is proportional to the concentration of the OH⁻ ions. When pH is less than 2, the silicic acid species becomes positively charged and the reaction rate of the condensation is proportional to the concentration of H⁺. Under strongly basic conditions, the solutions mostly include anionic species. Hence, the rate of Si-O-Si breaking or redissolution of particles is high at elevated pH (Figure.2) (11,20).

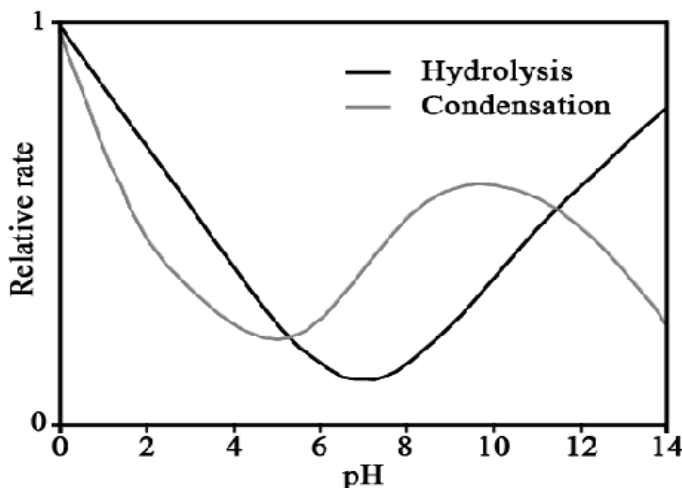


Fig. 2 Hydrolysis and condensation reaction rates depending on pH (21).

In this study, the effect of pH on the final physical and morphological properties of silica aerogels are comprehensively investigated. Achieving monolithic form of silica aerogels after drying period is another crucial target for the study. pH of the solutions was varied either in hydrolysis or condensation reactions as two parts. In the first part of the study, three samples prepared by changing the pH of the solution during hydrolysis reaction as 3, 4 and 5 while keeping the pH of the solution constant during the condensation period. By this way, the proper value of pH for the hydrolysis period was determined in order to

obtain a monolithic crack-free structure. In the second part of the study, pH value in hydrolysis reaction kept constant and the pH of the condensation reaction was varied as 8,9 and 10. Final physical and chemical form of the aerogels were analyzed to determine optimum condensation reaction pH as well. Samples obtained at favorable combination of reaction pHs were then physically, chemically and morphologically characterized.

2. Materials and Method

2.1. Materials

Silica aerogels were prepared by two-step sol-gel process followed by ambient pressure drying. Tetraethylorthosilicate (TEOS, 98%), 3-aminopropyl-triethoxysilane (APTES) used as silica precursors were purchased from Sigma Aldrich. Ethanol (EtOH) and n-Hexane were used as solvents; HCl, NH₄OH were involved in sol-gel process as catalyst. 1-ethyl-3-methylimidazolium bis(trifluoromethanesulfonyl)imide (EMIMTF2N) as imidazolium based ionic liquid (IL, 98%) was supplied from Sigma Aldrich and selected as drying control agent to give the final product a crack-free monolithic structure.

2.2. Preparation of silica aerogel

The silica aerogels were prepared by following two-step sol-gel process (Figure 3). This process consists of three main parts called as sol preparation and gelation, aging of the gel and drying.

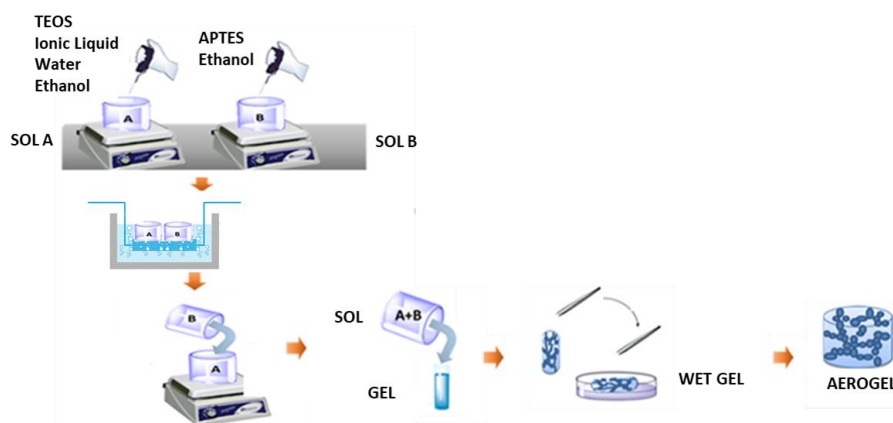


Fig. 3 Two step sol gel method.

During the sol preparation, two silane sources, TEOS and APTES were used. TEOS were hydrolyzed in the presence of IL and EtOH by using 0.01 M HCl for 30 min (sol A) whereas APTES were hydrolyzed only with EtOH for 30 min (sol B). After 30 min of mixing, the solutions were kept in a cold medium to satisfy a proper bonding between particles and hence to enhance the silica network. During the hydrolysis reactions, the silanol polar groups formed by hydrolysis attack each other to form covalent bonds, through simultaneously occurred condensation reaction. Sol A and Sol B are then combined for further continuation of the condensation reaction and fully completion of gelation. pH values of the solution which directly affects the rate of the formation reactions, were adjusted by using HCl. In the first step of this study (run 1), the pH value of hydrolysis in Sol A was adjusted as 3, 4 and 5 in Solution A, while pH of the Sol B was kept constant at 7.

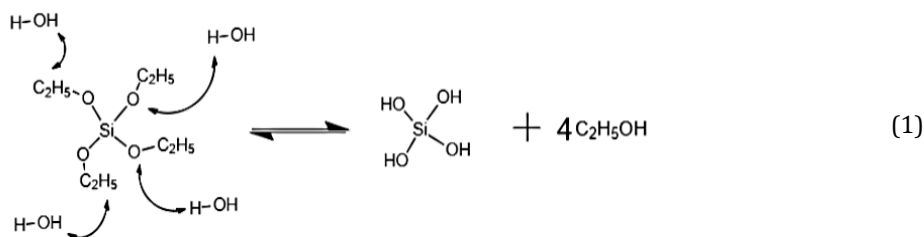
During the condensation period, the solution transformed from liquid state to gel form and ended up with the 3-dimensional network structure. The gelation rate of the sample is directly dependent on the kinetics of the condensation reaction. In the second part of the study (run2), the pH of the condensation reactions was adjusted as 8, 9 and 10 while keeping pH value of the hydrolysis reactions constant. The sol components in all samples and pH values of hydrolysis/condensation periods in run1 and run2 are shown in Table 1.

Table 1. Sol components of all samples in run 1 and run 2.

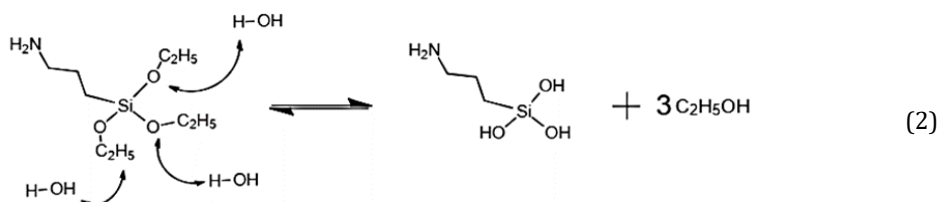
Run	ID	Molar ratios of sol components (mol/mol TEOS)	pH of Hydrolysis period	pH of Condensation period
		TEOS: APTES: IL: Water: EtOH		
Run 1	SG- pH 3/7	1: 0.141: 0.016: 5.167: 35.67	3	7
	SG- pH 4/7	1: 0.141: 0.016: 5.167: 35.67	4	7
	SG- pH 5/7	1: 0.141: 0.016: 5.167: 35.67	5	7
Run 2	SG- pH 3/8	1: 0.141: 0.016: 5.167: 35.67	3	8
	SG- pH 3/9	1: 0.141: 0.016: 5.167: 35.67	3	9
	SG- pH 3/10	1: 0.141: 0.016: 5.167: 35.67	3	10

Hydrolysis and condensation reactions of silica precursors take place as follows:

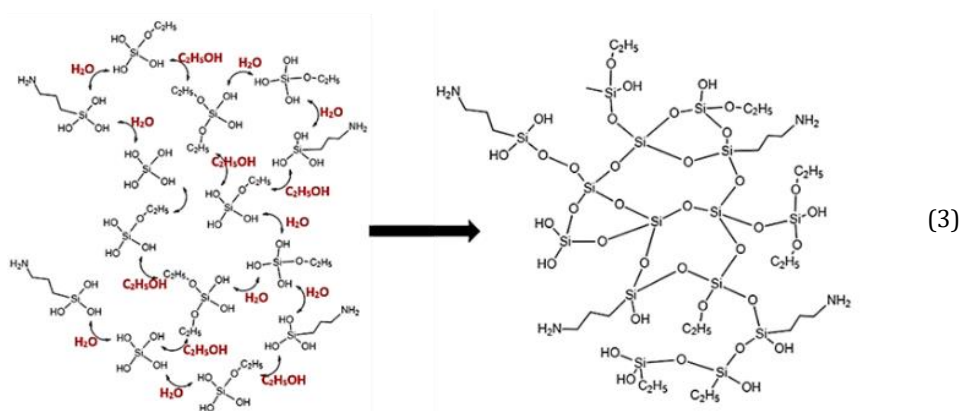
Hydrolysis reaction of TEOS:



Hydrolysis reaction of APTES:



Condensation reaction and the formation 3D structure:



After achieving complete gelation, the silica aerogels were exposed to an aging period of 24 h in a polypropylene cylindrical mold to allow further continuation of the condensation reactions. Afterward, silica aerogels were subjected to ambient pressure drying for 48 hours.

2.3 Characterizations

Bulk densities of dried gels were determined by using pycnometer. The percentages of porosity of the samples were estimated according to equation given below (Eq. 1);

$$\% \text{Porosity} = \left(1 - \frac{\rho}{2.1}\right) \times 100 \quad (1)$$

Where ρ is the bulk density of synthesized silica aerogel and 2.1 g/cm^3 is the density of solid skeleton (10).

The morphological characterizations of the prepared silica aerogels were evaluated by using Scanning Electron Microscope (SEM) (PHILIPS, XL 30S FEG) with a magnification rate of 10000. Fourier Transform Infrared Spectroscopy (FTIR) (PERKIN ELMER, Spectrum 100, ABD) analysis was performed between the wave number ranges of 500 to 4000 cm^{-1} to identify the chemical interactions within the samples.

Surface area, average pore volume and average pore diameters of silica aerogels were measured by physisorption of N_2 at 77 K by using Quantachrome Corporation, Autosorb6. Before the measurement, the samples were subjected to degassing operation at 120°C over night to remove residual moisture and adsorbed gases.

3. Results and Discussion

3.1 Physical Characterization of Aerogels

Visual observations and the density of the resulted material became our preliminary criteria to decide the optimum pH for hydrolysis. In the first part, three gels were hydrolyzed under the different media having various pH. The monolithic structure was only achieved with the one which has the hydrolysis pH of 3. When the pH of hydrolysis is increased to 4 or 5, samples are obtained in powder form as seen in Figure 4.

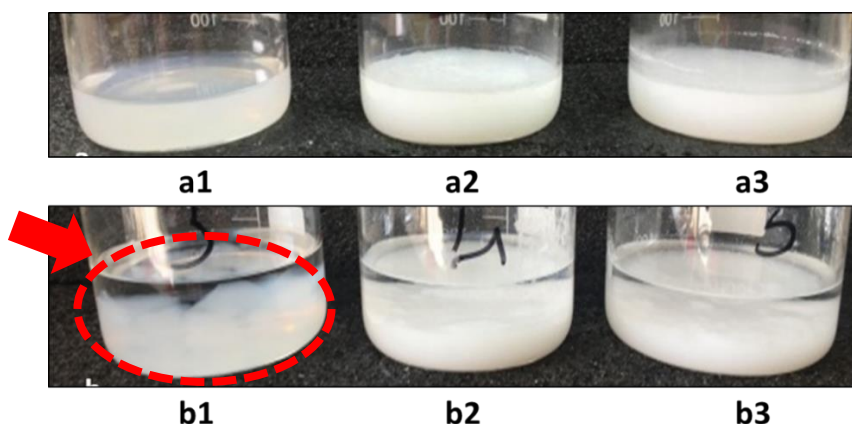


Fig. 4 Visual observations of prepared aerogels a1) SG-pH3/7, a2) SG-pH4/7, a3) SG-pH5/7 at gelation steps and b1) SG-pH3/7, b2) SG-pH4/7, b3) SG-pH5/7 at solvent extraction step.

In the hydrolysis mechanisms, a nucleophilic attack of oxygen ion pairs of the H_2O molecule on the Si atoms occurs firstly. Due to the polarized Si-O bonds, the silicon atoms carry a partially positive electronic charge, which in that case determines the kinetics of the nucleophilic attack and thus determines the overall hydrolysis reaction. In alkoxides, the Si atoms hold a partially moderate positive charge. Hence, the gelation kinetics of $Si(OC_2H_5)_4$ alkoxides get so slow unless the hydrolysis and condensation steps of Si are catalyzed either by bases that hold strong negative charges or by acids in which case the reaction mechanism changes drastically (11,21).

In the sol-gel reactions, the relative magnitudes of the hydrolysis and condensation rates are slow enough to allow an almost independent control. In general, silica gels with a texture closer to that of long silica chains in polymeric structures obtained if the hydrolysis rate becomes faster than the condensation rate. This was the case under acidic conditions in our study (SG-pH3/7). Therefore, more stable silica gel network was constructed at the pH value of 3. On the other hand, when the pH of the hydrolysis and condensation reaction are getting closer as in the case of sample SG-pH4/7 and sample SG-pH5/7, reactions can not be dominated by other reaction and it leads shorter silica chain length. Remained alkoxy groups due to the incomplete hydrolysis reaction hinder silica molecules from formation well defined SiO_2 structure. For these reasons, the second part of the study was conducted by adjusting the pH of the hydrolysis reaction 3 and the pH of the condensation reactions was varied from 8 to 10 by addition of 0.1 M base catalysts (NH_4OH). The same procedure was followed during synthesis and after drying in ambient condition, only one sample (SG-pH3/10) exhibited a high degree of monolithicity. At this pH in condensation reactions (pH=10) proton acceptors, i.e., bases accelerated the condensation reactions higher than hydrolysis reaction, which then promotes the formation of denser silica colloids (SG-pH3/10).

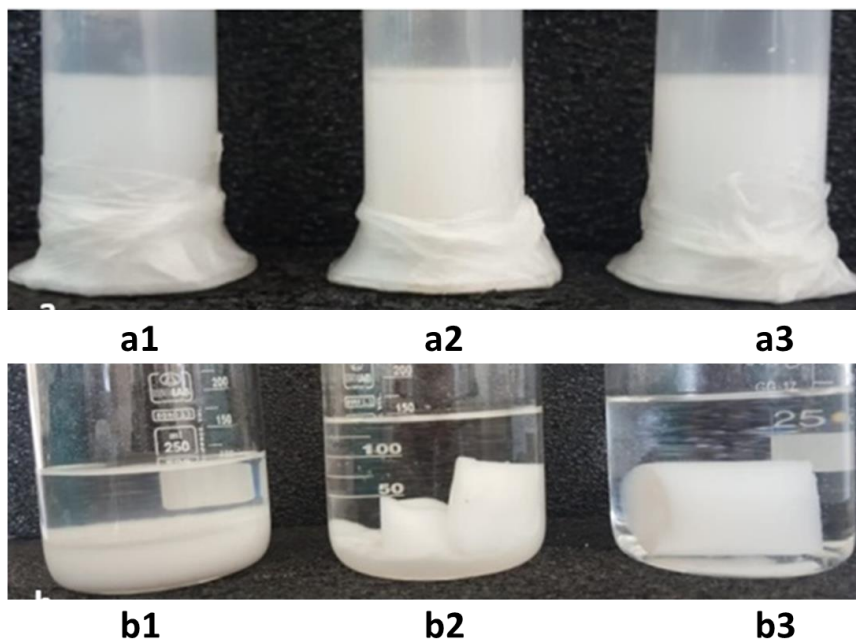


Fig. 5 Visual observations of prepared aerogels a1) SG-pH3/8, a2) SG-pH3/9, a3) SG-pH3/10 at gelation steps and b1) SG-pH3/8, b2) SG-pH3/9, b3) SG-pH3/10 at solvent extraction step.

The density and porosity for the samples are shown in Table 2.

Table 2. Physical properties of the all samples.

Run	ID	Density (g/cm ³)	Porosity (%)	Physical observations
Run 1	SG- pH 3/7	0.32	73.3	monolithic
	SG- pH 4/7	0.29	75.8	powder
	SG- pH 5/7	0.27	77.5	powder
Run 2	SG- pH 3/8	0.31	74.1	Powder
	SG- pH 3/9	0.24	80.0	granular
	SG- pH 3/10	0.35	70.8	monolithic

The density of each sample was measured by pycnometer and the percentage porosity were determined. A slight increase in the porosity observed with the increase in the pH in hydrolysis reactions. One possible reason for this situation can be the reduction in the superiority of the two reactions to each other owing to the adjustment of the pH at a moderate value. On the other hand, it would not be right to state this comment for the second part. The pH adjusted during the condensation period did not directly affect the porosity of the samples. When the pH of condensation reaction is increased up to 9 the porosity of the samples increased accordingly. On the other hand, when the pH of the condensation reaction adjusted at 10, reaction rate reached the maximal point and as the hydrolysis rate at this pH approached almost to the condensation rate, the porous structure deteriorated at this pH. The density value of the sample SG-pH3/10 was measured as 0.35 g/cm³ and the porosity value was determined as 70.8 percent. The final

sample had a slightly denser structure than the other samples, probably resulted from the monolithic form of the aerogel.

3.2 Chemical Characterization

FTIR analysis was performed to determine chemical structures of aerogels and the FTIR spectrums was given in Figure 6 and 7.

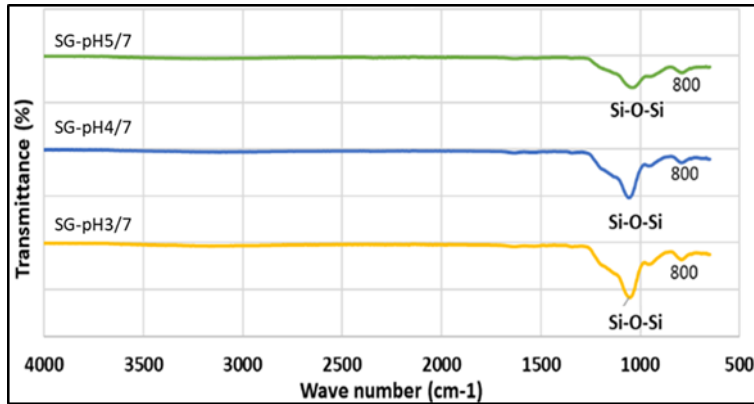


Fig. 6 FTIR spectrum of the prepared aerogels at the pH of 3, 4 and 5.

The values corresponding to peaks near 1080 cm^{-1} can be attributed to Si-O-Si bonding in the chemical structure of aerogels and indicates the how well the silica network is established (2). As shown in Figure 6, the depth of Si-O-Si bonds at 1081 cm^{-1} decreased as pH increased. Thus, the strongest Si-O-Si bond was obtained at a pH of 3. This indicates that the perfect hydrolysis was achieved at the pH value of 3.

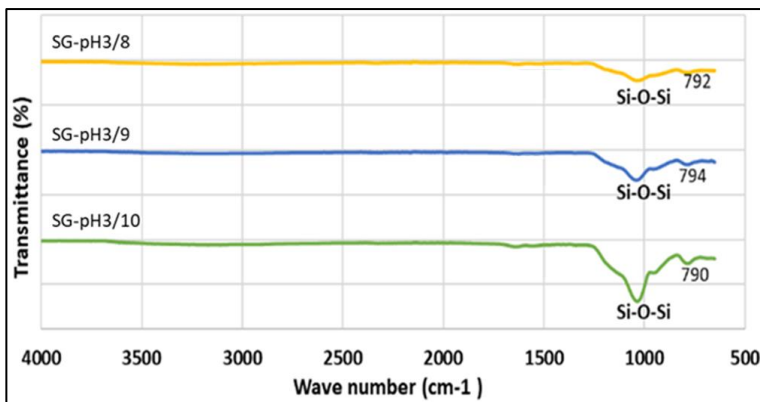


Fig. 7 FTIR spectrum of prepared aerogels at the pH of 8, 9 and 10.

Figure 7 represents the FTIR results of silica aerogels in which the condensation reactions occurs at the pH of 8, 9 and 10. Results have shown that as the pH increased, the condensation reaction accelerated and the intensity of the Si-O-Si bonding increased.

3.3 Gelation Behavior

Figure 8 shows the duration of the gelation during the preparation of the samples.

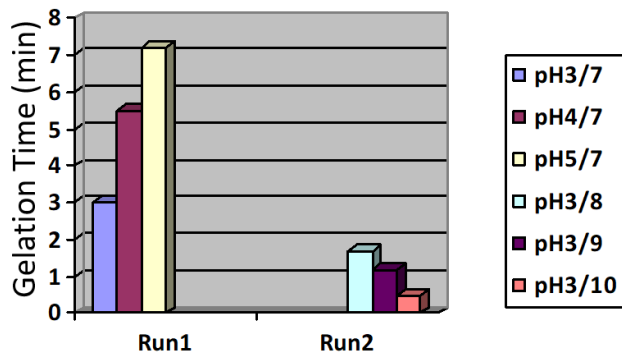


Fig. 8 Gelation time of run1 and run2.

It was observed that when the pH of the condensation reaction is about 7, it took relatively longer time to achieve complete gelation. However, the gelation times at pH higher than 7 occurs fast, which means that there was hardly any time for the system to condensate into a well-defined network. In such gelation times, the generation of larger pores also inevitable. These larger pores act as scattering centers for light in the visible range of the spectrum and caused opacity of the final aerogel, too. As shown in Figure 9, the sample SG-pH 3/10, which showed rapid gelation, had a more opac appearance than the SG-pH 3/7 that has slow gelation.



Fig. 9 Visual observation of the samples SG-pH3/7 and SG-pH3/10, respectively.

3.4 Morphological characterization

Microstructural patterns of the produced silica aerogels (SG-pH3/7, SG-pH4/7, SG-pH5/7 and SG-pH3/10) were examined via SEM analysis.

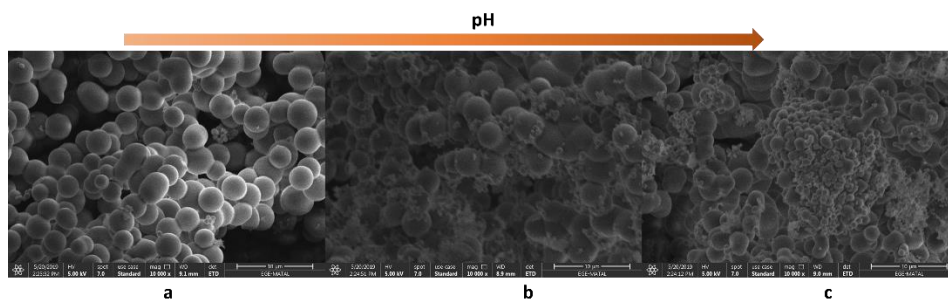


Fig. 10 SEM Image (x10000) of the samples a)SG-pH3/7, b)SG-pH4/7, c)SG-pH5/7.

SEM images confirmed the results about the existence of well-defined primary silica particles in SG-pH3/7 rather than other samples in run1. Due to completion of sufficient hydrolysis during the synthesis of the sample SG-pH3/7, there observed a homogenously distribution of the nearly same sized silica particles for this sample. When the pH in hydrolysis reaction increased, it yielded less homogenous pore network and non-uniform particle size as in Figure 10b and 10c.

On the other hand, when the condensation reaction increased to 10, regarding to severe Si-O formation and very fast condensation reaction, very small silica particles formed and agglomerated on each other as small clusters as in Figure 11. As a result, SG-pH3/10 yielded less porous form with denser solid structure comparing to SG-pH3/7.

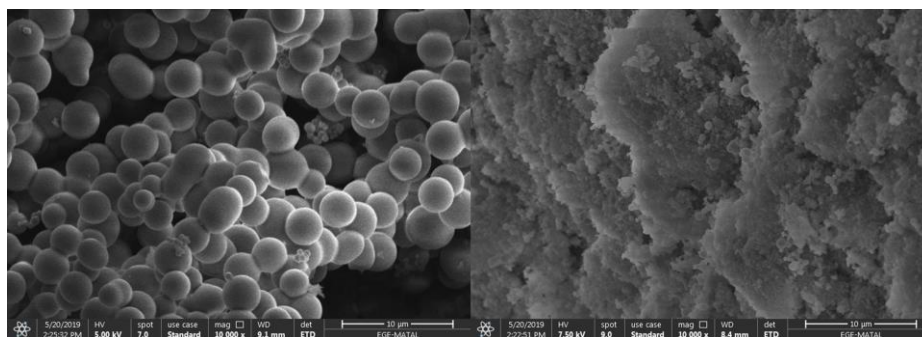


Fig. 11 SEM Image with 10000-magnification rate of the samples SG-pH3/7 and SG-pH3/10, respectively.

Surface area, pore volume and average pore diameter values after Nitrogen adsorption/desorption measurements were summarized in Table 3. BET surface area for SG-pH3/7 exhibited relatively high surface area ($65 \text{ m}^2/\text{g}$) than the SG-pH3/10. Accordingly, average pore volume value also higher for this sample. This outcome is compatible with homogenous distribution of the pores in this sample compared to that of SG-pH3/10. Results also confirm the existence of micropores in the structure for SG-pH3/7, too. Pore dimensions increased as the pH of the condensation reaction increase and for SG-pH3/10 scale of the pores was increased from micro to meso scale.

Table 3. Pore characteristics of silica aerogels

Sample ID	Specific Surface Area (m ² /g)	Pore Volume (cm ³ /g)	Average pore diameter (nm)
SG-pH3/7	65	0.147	1.73
SG-pH3/10	37	0.050	2.13

4. Conclusions

In this study, the effect of pH that is one of the most crucial parameter affecting the final properties and physical appearances of silica aerogels was investigated. For this purpose, various pH values are examined during the sol-gel reactions. In the first part of the study, three samples prepared by changing the pH of the solution during hydrolysis reaction while keeping the pH of the solution constant during the condensation period. In this way, the appropriate pH was determined as 3 for the hydrolysis period in order to obtain a monolithic crack-free structure (the sample SG-pH3/7). In the second part, pH was varied during the condensation period while keeping pH value constant as three with respect to the previous part. In this part, only one sample (SG-pH3/10) exhibited a high degree of monolithicity. At this pH value, the condensation reaction was accelerated more than the hydrolysis step, which then favors the formation of 3D colloidal silica particles and monolithic form of gels (SG-pH3/10).

It was visually observed that only two samples (SG-pH3/7 and SG-pH3/10) have preserved their monolithic structure after drying during this whole study. Although the chemical characteristics defined by FTIR analysis were similar, density measurements exhibited that the sample SG-pH3/7 had slightly lighter and more porous than the sample SG-pH3/10. At the same time, SEM and BET analyses have identified that the sample SG-pH3/7 had a well-defined and homogenous size of primary particles with higher specific surface area and pore volume.

References

- [1]Laskowski J, Milow B, Ratke L. Aerogel-aerogel composites for normal temperature range thermal insulations. *J Non Cryst Solids*, 2016;441:42-8. <https://doi.org/10.1016/j.jnoncrsol.2016.03.020>
- [2]Soleimani Dorcheh A, Abbasi MH. Silica aerogel; synthesis, properties and characterization. *J Mater Process Technol.* 2008;199(1):10-26. <https://doi.org/10.1016/j.jmatprotec.2007.10.060>
- [3]Maleki H, Durães L, Portugal A. An overview on silica aerogels synthesis and different mechanical reinforcing strategies. *J Non Cryst Solids*, 2014;385:55-74. <https://doi.org/10.1016/j.jnoncrsol.2013.10.017>
- [4]Pons A, Casas L, Estop E, Molins E, Harris KDM, Xu M. A new route to aerogels: Monolithic silica cryogels. *J Non Cryst Solids*. 2012;358(3):461-9. <https://doi.org/10.1016/j.jnoncrsol.2011.10.031>
- [5]Amonette JE, Maty J. Microporous and Mesoporous Materials Functionalized silica aerogels for gas-phase purification, sensing, and catalysis: A review. 2017;250. <https://doi.org/10.1016/j.micromeso.2017.04.055>
- [6]Maleki H, Durães L, García-gonzález CA, Mahmoudi M. Synthesis and biomedical applications of aerogels: Possibilities and challenges. 2016;236:1-27. <https://doi.org/10.1016/j.cis.2016.05.011>

- [7]Buratti C, Merli F, Moretti E. Aerogel-based materials for building applications: Influence of granule size on thermal and acoustic performance. *Energy Build.* 2017;152:472-82. <https://doi.org/10.1016/j.enbuild.2017.07.071>
- [8]Li Z, Cheng X, He S, Shi X, Gong L, Zhang H. Aramid fibers reinforced silica aerogel composites with low thermal conductivity and improved mechanical performance. *Compos Part A Appl Sci Manuf.*, 2016;84:316-25. <https://doi.org/10.1016/j.compositesa.2016.02.014>
- [9]Li M, Jiang H, Xu D, Hai O, Zheng W. Low density and hydrophobic silica aerogels dried under ambient pressure using a new co-precursor method. *J Non Cryst Solids*, 2016;452:187-93. <https://doi.org/10.1016/j.jnoncrysol.2016.09.001>
- [10]Wei TY, Chang TF, Lu SY, Chang YC. Preparation of monolithic silica aerogel of low thermal conductivity by ambient pressure drying. *J Am Ceram Soc.* 2007;90(7):2003-7. <https://doi.org/10.1111/j.1551-2916.2007.01671.x>
- [11]Shi F, Wang L, Liu J. Synthesis and characterization of silica aerogels by a novel fast ambient pressure drying process. *Mater Lett.* 2006;60(29-30):3718-22. <https://doi.org/10.1016/j.matlet.2006.03.095>
- [12]Hilonga A, Kim JK, Sarawade PB, Kim HT. Low-density TEOS-based silica aerogels prepared at ambient pressure using isopropanol as the preparative solvent. *J Alloys Compd.* 2009;487(1-2):744-50. <https://doi.org/10.1016/j.jallcom.2009.08.055>
- [13]Vioux A, Viau L, Volland S, Le Bideau J. Use of ionic liquids in sol-gel; ionogels and applications. *Comptes Rendus Chim.* 2010;13(1-2):242-55. <https://doi.org/10.1016/j.crci.2009.07.002>
- [14]Wu C, Lin S. Preparation and Fractal-Structure Characterization of Monolithic Silica Aerogel with a Short-Chain Ionic Liquid as the Solvent. 2010;126:123-6. <https://doi.org/10.14723/tmrj.37.123>
- [15]Smitha S, Shajesh P, Aravind PR, Kumar SR, Pillai PK, Warriar KKG. Effect of aging time and concentration of aging solution on the porosity characteristics of subcritically dried silica aerogels. *Microporous Mesoporous Mater.* 2006;91(1-3):286-92. <https://doi.org/10.1016/j.micromeso.2005.11.051>
- [16]Dourbash A, Motahari S, Omranpour H. Effect of water content on properties of one-step catalyzed silica aerogels via ambient pressure drying. *J Non Cryst Solids*, 2014;405:135-40. <https://doi.org/10.1016/j.jnoncrysol.2014.09.013>
- [17]Sinkó K. Influence of chemical conditions on the nanoporous structure of silicate aerogels. *Materials (Basel)*. 2010;3(1):704-40. <https://doi.org/10.3390/ma3010704>
- [18]Schubert U. Sol - Gel Chemistry and Methods. *Sol-Gel Handb Synth Charact Appl.* 2015;1-28. <https://doi.org/10.1002/9783527670819.ch01>
- [19]Wu CM, Lin SY, Chen HL. Structure of a monolithic silica aerogel prepared from a short-chain ionic liquid. *Microporous Mesoporous Mater.*, 2012;156:189-95. <https://doi.org/10.1016/j.micromeso.2012.02.039>
- [20]Juan Vivero. *Silica Nanoparticles; preparation, properties and uses.* Vol. 1, Nova Science Publisher, Inc. 2012. 53 p.
- [21]Bera S, Udayabhanu G, Narayan R, Rout TK. *Sol-Gel Process for Anti-Corrosion Coatings.* 2013;209-31.
- [22]Sachithanadam M, Chandrakant Joshi S. *Silica Aerogel Composites.* Engineering Materials. 2016. <https://doi.org/10.1007/978-981-10-0440-7>

Blank Page



Research Article

Tribological properties of PPS/PA46 polymer blends

Ferhat Yıldırım^{*1,a}, Mustafa Aydın^{2,b}, Hakan Yetgin^{3,c}

¹Machinery and Metal Technologies Department, Biga Vocational School, Çanakkale Onsekiz Mart University, Çanakkale, Turkey

²Mechanical Engineering Department, Hasan Ferdi Turgutlu Technologie Faculty, Manisa Celal Bayar University, Manisa, Turkey

³Mechanical Engineering Department, Simav Technologie Faculty, Kütahya Dumlupınar University, Kütahya, Turkey

Article Info

Article history:

Received 07 Aug 2019

Revised 01 Mar 2020

Accepted 02 Mar 2020

Keywords:

Fiber Glass

Reinforcement;

Hybrid Composite;

Polyamide 46;

Polyphenylene Sulfide;

Wear

Abstract

In this study, the tribological performance of originally 40 wt.% fiber glass reinforced polyphenylene sulfide (PPS-G), polyamide 46 (PA46) and their blends were studied at dry sliding conditions. The materials were mixed and extruded on the twin screw extruder. The blends were dried and tribological test specimens were manufactured by using the injection machine. Wear tests were performed with the configuration of a polymer pin on a rotating X40CrMoV5-1 steel disc. Test conditions were atmospheric conditions having 60, 90, 120 N loads and 0.5, 1.0, 1.5 m/s sliding speeds. The obtained results proved that the coefficient of friction for PPS-G, PA46 and their blends is decrease while the applied load and sliding speed values are increase. On the other hand, the specific wear rate is in increase while the applied load and sliding speed values are in increase.

© 2020 MIM Research Group. All rights reserved.

1. Introduction

Polyphenylene sulfide (PPS) is a semi crystalline high-performance engineering thermoplastic polymer with excellent properties such as high temperature performance, heat resistance, chemical resistance, electrical insulation, high dimensional stability, good mechanical properties and flame retardancy without additives [1-5]. This property of PPS makes it popular in various applications including electronics and electrical appliances, automobile, chemical sector and aerospace [6-10]. However, the application of PPS has been limited due to its relatively low glass transition temperature (~ 90 °C), rather brittle with a low elongation at break and high cost [1, 2, 5, 7, 8, 11, 12]. In order to overcome these problems, PPS was blended with other polymers or reinforced with rigid particles [5, 11]. Polyamides (PAs) such as PA6, PA46 and PA66 are generally investigated for their wear performance [4, 12-14]. Among them, the chemical structure of PA46 offers an advantage compared to PA6 and PA66 [15].

The tribological performance of polymers and polymer blends are directly related to the test parameters like loads, sliding speed and distance and transfer film properties [16, 17]. The effect of test conditions on friction and wear behavior properties of PA, PPS and their composites have been reported in earlier papers [4, 12, 18]. Chen et al. [12] investigated the mechanical and tribological properties of PA66 and PPS blends. Tribological test was performed under ambient conditions at a speed of 0.42 m/s and a normal load of 196 N.

*Corresponding author: ferhatyildirim@comu.edu.tr

^aorcid.org/0000-0002-0524-4050; ^borcid.org/0000-0002-9150-4081; ^corcid.org/0000-0002-6068-9204

DOI: <http://dx.doi.org/10.17515/resm2019.144ma0607>

Res. Eng. Struct. Mat. Vol. 6 Iss. 3 (2020) 271-282

They pointed out that the minimum wear volume was obtained in the case of PA66/PPS (80/20) blend and the wear volume of blends increased with PPS proportion after the PPS content exceeds 20 vol. %. Zhou et al. [4] investigated the effect of carbon fiber (CF) on mechanical and tribological performance of the PA6/PPS composites. The friction and wear tests were carried out under 10 N, 15 N and 20 N loads and 500, 1000 and 1500 rpm/min rotate speeds, for a duration of 40 min. Under the friction condition of high applied load or high sliding speed, friction coefficient of the PA6/PPS-CF composites tends to decrease, and wear rate tends to increase. Zhao and Bahadur [18] investigated the tribological behaviors of the particulates NiS and PbSe filled polyphenylene sulfide (PPS) composites under ambient conditions in a pin-on-disk configuration at a sliding speed of 1.0 m/s and a nominal pressure of 0.65 MPa. Cho [19] studied the role of transfer films formed during the sliding of PPS/CuO/CF/Kevlar polymer composites against the steel counter face. It was reported that as far as the transfer film became smooth and uniform, the wear rate decreased. Cho et al. [20] studied the tribological behavior of molybdenum-concentrate (MC) filled polyphenylene sulfide (PPS). They reported that MC, as the filler in particulate form, reduced the steady state wear rate of PPS, and the optimum reduction in wear was found to occur with the addition of polytetrafluoroethylene (PTFE) along with PPS. Cong et al. [13] investigated the tribological properties of PA46/HDPE poly blend with different component ratios. They reported that HDPE was effective in reducing the friction coefficient of PA46 and specific wear rate of PA46/HDPE poly blend decreased with increasing HDPE content. Scherge et al. [14] investigated the wear characteristics of aliphatic PA 46 on lubricated steel disk. They declared that under certain boundary parameters at transfer film forms and significantly improvement wear performance. Yu et al. [21] studied the friction and wear behaviors of polyamide 66 (PA 66) and rubber-filled PA 66 (PA 66/SEBS-*g*-MA) composites on a block-on-wheel model friction and wear tester under dry sliding and water lubricating conditions. The friction coefficients of PA 66 and PA 66/SEBS-*g*-MA composites under water lubricating condition were lower than those under dry sliding condition, but the wear mass losses were higher than those under dry sliding condition. It is seen from the literature that the majority of the investigations confined their discussions to dry sliding condition.

It is known that high thermal resistant polymer such as PPS and PA46 are used in automotive industry as products (such as fuel injection systems, air intake manifold, coolant systems, water pump impellers, thermostat holder, electric brakes, switches, bulb housing and so on) that work under the effects of temperature and pressure [22-25]. And, at the same time, they remain in constant friction with other metal and polymer materials with which they are in contact, both due to engine vibration and road shock. Although their usage is increasingly widespread there is no enough study about on the tribological properties of PA/PPS polymer blends. So, in this study these two high temperature polymers that are widely used in industry are selected and the influence of sliding speed and load values on the friction and wear characteristics of PA46, PPS-G (originally glass fiber reinforced PPS) and their blends were studied.

2. Material and Method

The selected materials polyamide 46 (Stanyl PA46) with 1.18 g/cm³ density was supplied from Royal DSM (Holland) and 40 wt.% glass fiber filled PPS (PPS S25G40) with 1.57 g/cm³ density was supplied from Kolon Plastic Inc. (China). PPS/PA46 blends were manufactured on AYS LAB30 model, was given in Fig. 1.a, co-rotating double screw extruder machine in the following volume ratios: 100/0; 90/10; 80/20; 50/50 and 0/100. The extruder temperatures from the feed zone of polymer to the exit die were 275, 280, 288, 295 and 300 °C, respectively. The extruder exit die diameter is 4 mm and the screw speed was 70 rpm. The polymers were dehumidified at 140 °C for 4 hours before extrusion. The extruded

polymer mix material pelletized in the crusher. Thereafter, the injected samples (Fig.1.c) for wear tests were produced using the injection machine Demag Stübbe S110, which was given in Fig. 1.b at 500 bar injection pressure. The injection temperatures from the feed zone to the exit nozzle were 275, 285, 295, 300 and 300 °C. The screw speed was 80 cm³/s and the mould temperature was 30 °C.

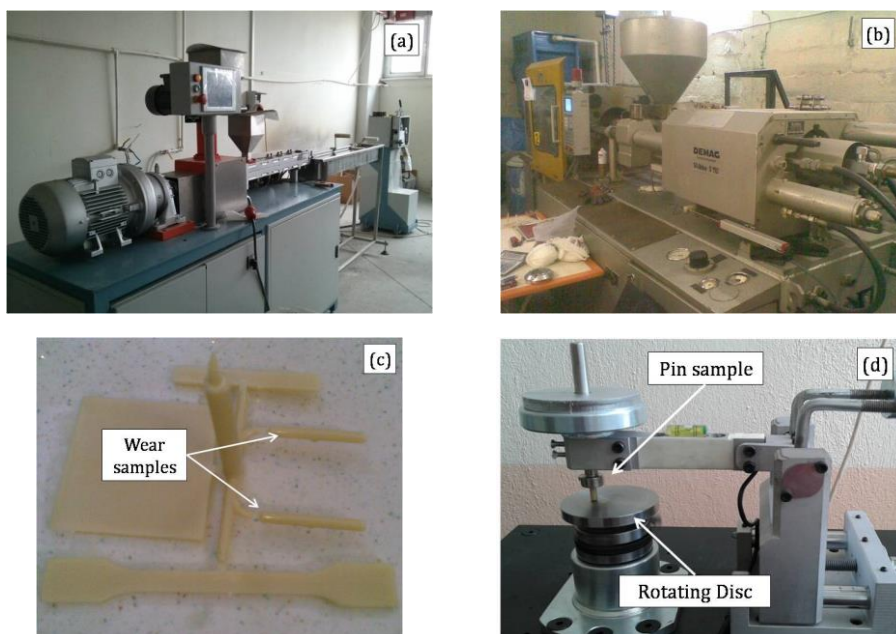


Fig.1.a) AYSA LAB30 co-rotating twin-screw extruder, b) DemagStübbe S110 injection-molding machine, c) Injected test samples, d) Pin-on-disc wear test rig.

Fig. 1.d shows the pin-on-disc wear test rig. The wear tests were performed at room temperature with non-lubrication or any wetting system. Materials and the specific test conditions (i.e. materials, ambient temperature, applied load, sliding speed and humidity) selected for this study were summarized in Table 1.

Table 1 Properties and specific test parameters of the PPS-40GF, PA46 and their blends.

Materials	Density (g/cm ³)	Applied load (N)	Sliding speed (mm/s)	Temperature (°C)	Humidity (%)
PPS-G	1.57				
PPS-G/10%PA46	1.51				
PPS-G/20%PA46	1.42	60, 90, 120	0.5, 1.0, 1.5	22±3	50±5
PPS-G/50%PA46	1.34				
PA46	1.18				

As is known, polymer materials generally work against metal materials in terms of their use. Therefore, in this study, medium carbon steel (AISI 1040) material was chosen as the counter disc surface. The disc of the wear test rig had 100 mm diameter and 5 mm thickness. The cylindrical polymer pin samples had 5 mm diameter and 50 mm length. Before the wear test, the samples contact surfaces were processed at 1000 grade paper. In addition, both disc and sample surfaces were cleaned with alcohol and then dried quickly.

All tests were performed in three times and their averages results were taken. The average mass loss in the pin was measured and the specific wear rates were calculated.

3. Results and Discussion

Table 2 gives the coefficient of friction results for PPS-G, PPS-G/10%PA46, PPS-G/20%PA46, PPS-G/50%PA46 and PA46 polymers according to the test parameters. The coefficient of friction is expressed as the ratio of lateral force to normal applied force and is calculated by Eq. 1.

$$\mu = \frac{F_S}{F_N} \quad (1)$$

Here; μ is friction coefficient, F_S is lateral friction force and F_N is normal applied force.

Table 2 Average coefficient of friction values for PPS-G, PPS-G/10%PA46, PPS-G/20%PA46, PPS-G/50%PA46 and PA46 polymers tested at different load and sliding speed values.

Materials	Load (N)	Sliding speed (m/s)		
		0.5	1.0	1.5
Coefficient of friction (μ)				
PPS-G	60	0.2853	0.2601	0.2495
	90	0.2784	0.2248	0.1956
	120	0.2566	0.2018	0.1822
PPS-G/10%PA46	60	0.3234	0.2916	0.2687
	90	0.3042	0.2413	0.2225
	120	0.2778	0.2239	0.2011
PPS-G/20%PA46	60	0.3467	0.3266	0.3033
	90	0.3294	0.2824	0.2571
	120	0.3018	0.2591	0.2375
PPS-G/50%PA46	60	0.4144	0.3786	0.3484
	90	0.3866	0.3274	0.2966
	120	0.3412	0.3024	0.2856
PA46	60	0.4823	0.4461	0.4192
	90	0.4266	0.3808	0.3515
	120	0.3908	0.3644	0.3264

The variation of the coefficient of friction with sliding distance for PPS-G, PPS-G/10%PA46, PPS-G/20%PA46, PPS-G/50%PA46 and PA46 polymers performed under 90 N load and 1.0 m/s sliding speed is given in Fig. 2. It is clearly seen from this graph, that the coefficient of friction curves for PPS-G, PA46 and their blends increases rapidly beginning the test at running-in period and reaches more stable course within the steady state period. During the running-in period, wear debris are formed between the contact surface, and the wear debris become compacted and adhered on the disc surface lowering coefficient of friction in the steady-state period [26]. Similar results were obtained by Chen et. al [12] and Zhou et. al [4].

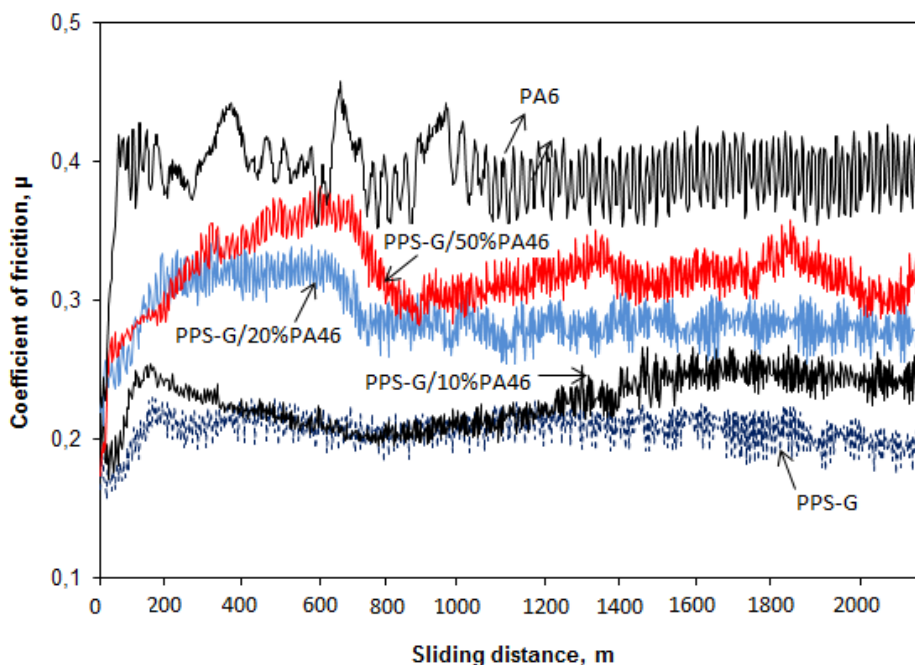


Fig. 2 Variation of coefficient of friction with sliding distance for PPS-G, PPS-G/10%PA46, PPS-G/20%PA46, PPS-G/50%PA46 and PA46 polymers (sliding speed: 1:0 m/s, Applied load: 90N).

If the chart is carefully considered, the overall trend for the coefficient of friction of PA46/PPS-G blends is similar, but coefficient of friction of PA46 is quite high than the PPS-G and PPS-G/PA46 blends, especially in the steady state. It was found that the coefficient of friction for PPS-G and PA46/PPS-G blends and for PA46, was between 0.2-0.35 and was 0.4 respectively.

Figs. 3 and 4 gives the variation of the coefficients of friction for PPS-G, PPS-G/10%PA46, PPS-G/20%PA46, PPS-G/50%PA46 and PA46 polymers accordance to the applied load and sliding speeds, respectively. In Fig. 3 for PPS-G, PPS-G/10%PA46, PPS-G/20%PA46, PPS-G/50%PA46 and PA46 polymers at 1.0 m/s sliding speeds, the coefficient of friction decreases linearly while the load increases. These results are adjusted with the past studies which had been completed by Unal [27], Yuji [28], Jiang [29], Zhou [4] and Wang [16]. In the case of PPS-G, PPS-G/10%PA46, PPS-G/20%PA46, PPS-G/50%PA46 and PA46, there is an average decrease result 22%, 23%, 21%, 20% and 18% in the coefficient of friction values while the applied load increases, respectively. The contact temperature between polymer and steel disc surfaces increased because of the increase in the applied load, which resulted in two different effects on the coefficient of friction. The first one, the real contact area increased between surfaces and then the coefficient of friction increased. The second, the shear strength decreased and thus the coefficient of friction decreased [16].

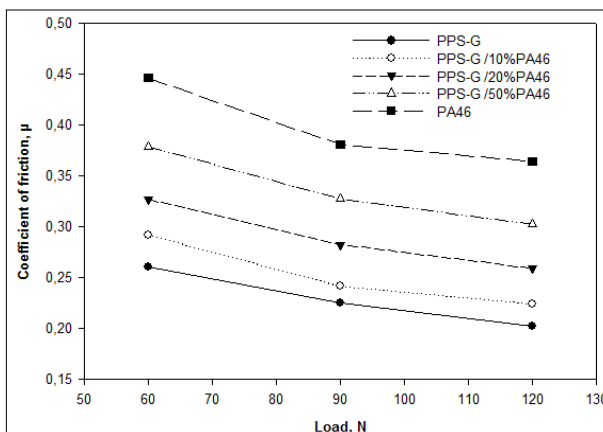


Fig. 3 Variation of coefficient of friction with applied load for PPS-G, PPS-G/10%PA46, PPS-G/20%PA46, PPS-G/50%PA46 and PA46 polymers (Sliding speed: 1.0 m/s).

In Fig. 4 for PPS-G, PA46 and their blends at 90 N applied load, the coefficient of friction decreases linearly while the sliding speed increases. For PPS-G, PPS-G/10%PA46, PPS-G/20%PA46, PPS-G/50%PA46 and PA46, there is an average decrease of approximately 30%, 26%, 21%, 23% and 17% in the coefficient of friction values while the sliding speed increase from 0.5 m/s to 1.5 m/s. It is clear from these graphs that the sliding speed influence is much higher than the applied load. The similar results were obtained by Zhou [4] and Zhang [24]. Furthermore, with the increase of the content of PA46 polymer, the coefficient of friction of PPS-G/PA46 blends increases.

Table 3 shows the specific wear rate and weight loss values in PPS-G, PPS-G/10%PA46, PPS-G/20%PA46, PPS-G/50%PA46 and PA46 polymers tested under 60, 90 and 120 N load, at 0.5, 1.0 and 1.5 m/s speeds and for 2000 m sliding distance. To determine the wear rate of the materials, the samples are weighed with a precision scale before and after the wear test. By calculating the difference between the initial weight and the final weight, the wear loss value of the sample is found for the determined conditions. The wear loss value is used to find the specific wear rates of materials by using the formulation in Eq. 2.

$$W_a = \frac{\Delta_m}{S \cdot \rho \cdot F_N} \tag{2}$$

Here, W_a is wear rate, Δ_m is wear loss, S is slide distance, ρ is density of materials and F_N is normal force.

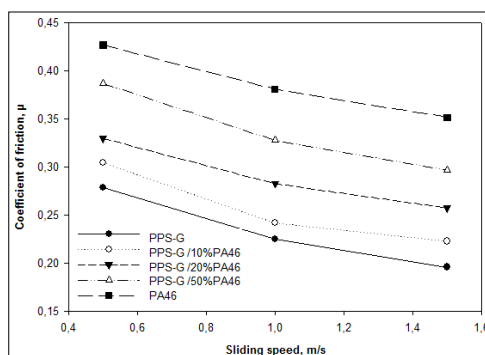


Fig. 4 Variation of coefficient of friction with sliding speed for PPS-G, PPS-G/10%PA46, PPS-G/20%PA46, PPS-G/50%PA46 and PA46 polymers (Applied load: 90 N).

Table 3 Specific wear rates and weight loss values for PPS, PPS/10%PA46, PPS/20%PA46, PPS/50%PA46 and PA46 polymers tested at different load and sliding speed values.

Materials	Load (N)	Speed (m/s)					
		0.5			1.5		
		Weight loss (g)			Specific wear rate (m ² /N)		
PPS-G	60	0,0017	0,0019	0,0021	9.023E ⁻¹⁵	1.008E ⁻¹⁴	1.114E ⁻¹⁴
	90	0,0031	0,0042	0,0049	1.096E ⁻¹⁴	1.486E ⁻¹⁴	1.733E ⁻¹⁴
	120	0,0044	0,0061	0,0071	1.167E ⁻¹⁴	1.618E ⁻¹⁴	1.884E ⁻¹⁴
PPS-G/10%PA46	60	0,0027	0,0029	0,0034	1.490E ⁻¹⁴	1.600E ⁻¹⁴	1.876E ⁻¹⁴
	90	0,0043	0,0049	0,0056	1.582E ⁻¹⁴	1,802E ⁻¹⁴	2.060E ⁻¹⁴
	120	0,0061	0,0072	0,0084	1.683E ⁻¹⁴	1.986E ⁻¹⁴	2.317E ⁻¹⁴
PPS-G/20%PA46	60	0,0035	0,0037	0,0041	2.053E ⁻¹⁴	2.171E ⁻¹⁴	2.406E ⁻¹⁴
	90	0,0054	0,0058	0,0066	2.112E ⁻¹⁴	2.269E ⁻¹⁴	2.582E ⁻¹⁴
	120	0,0078	0,0091	0,0104	2.288E ⁻¹⁴	2.670E ⁻¹⁴	3.051E ⁻¹⁴
PPS-G/50%PA46	60	0,0039	0,0046	0,0051	2.425E ⁻¹⁴	2.860E ⁻¹⁴	3.171E ⁻¹⁴
	90	0,0062	0,0073	0,0085	2.570E ⁻¹⁴	3.026E ⁻¹⁴	3.524E ⁻¹⁴
	120	0,0084	0,0103	0,0117	2.611E ⁻¹⁴	3.202E ⁻¹⁴	3.638E ⁻¹⁴
PA46	60	0,0041	0,0051	0,0059	2,895E ⁻¹⁴	3.601E ⁻¹⁴	4.166E ⁻¹⁴
	90	0,0063	0,0079	0,0092	2.961E ⁻¹⁴	3.719E ⁻¹⁴	4.331E ⁻¹⁴
	120	0,0086	0,0108	0,0124	3.036E ⁻¹⁴	3.813E ⁻¹⁴	4.378E ⁻¹⁴

Figs. 5 and 6 illustrate the variation of specific wear rate accordance to the applied load and sliding speed, respectively. In general, the specific wear rate for PPS-G, PPS-G/10%PA46, PPS-G/20%PA46, PPS-G/50%PA46 and PA46 polymers were in the order of 10^{-14} m^2/N . The lowest wear rate is for PPS-G with a value of 9.02×10^{-15} m^2/N while the highest wear rate is for PA46 with a value of 4.37×10^{-15} m^2/N . The wear rates of PA46, PPS-G/10%PA46, PPS-G/20%PA46 and PPS-G/50%PA46 are 60, 51, 38 and 18 times lower than that of PPS-G at 1.0 m/s sliding speed and 90 N applied load, respectively. For PPS-G and its blends performed in this study within the applied load range of 60–120 MPa, the specific wear rates are increased with the increase in the applied load.

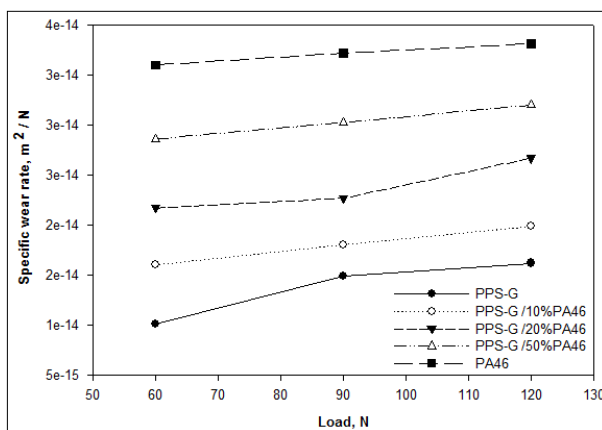


Fig. 5 Variation of specific wear rate with applied load for PPS-G, PPS-G/10%PA46, PPS-G/20%PA46, PPS-G/50%PA46 and PA46 polymers (Sliding speed: 1.0 m/s).

In Fig. 6 the specific wear rate values for PPS-G, PPS-G/10%PA46, PPS-G/20%PA46, PPS-G/50%PA46 and PA46 polymers increase linearly while the sliding speed increases. In case of PPS-G, PPS-G/10%PA46, PPS-G/20%PA46, PPS-G/50%PA46 and PA46, there are about 36%, 23%, 18%, 27% and 31% increase in specific wear rate from 0.5 m/s to 1.5 m/s in the sliding speed at 90 N applied load, respectively. All the findings clearly match with the earlier studies results obtained by Unal [30], Zhang et al. [26] and Wang et al. [16].

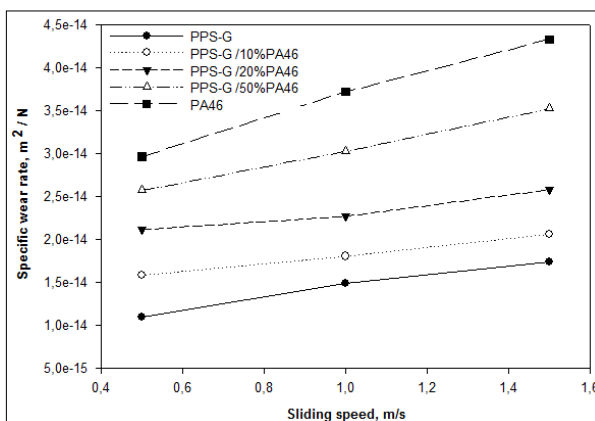
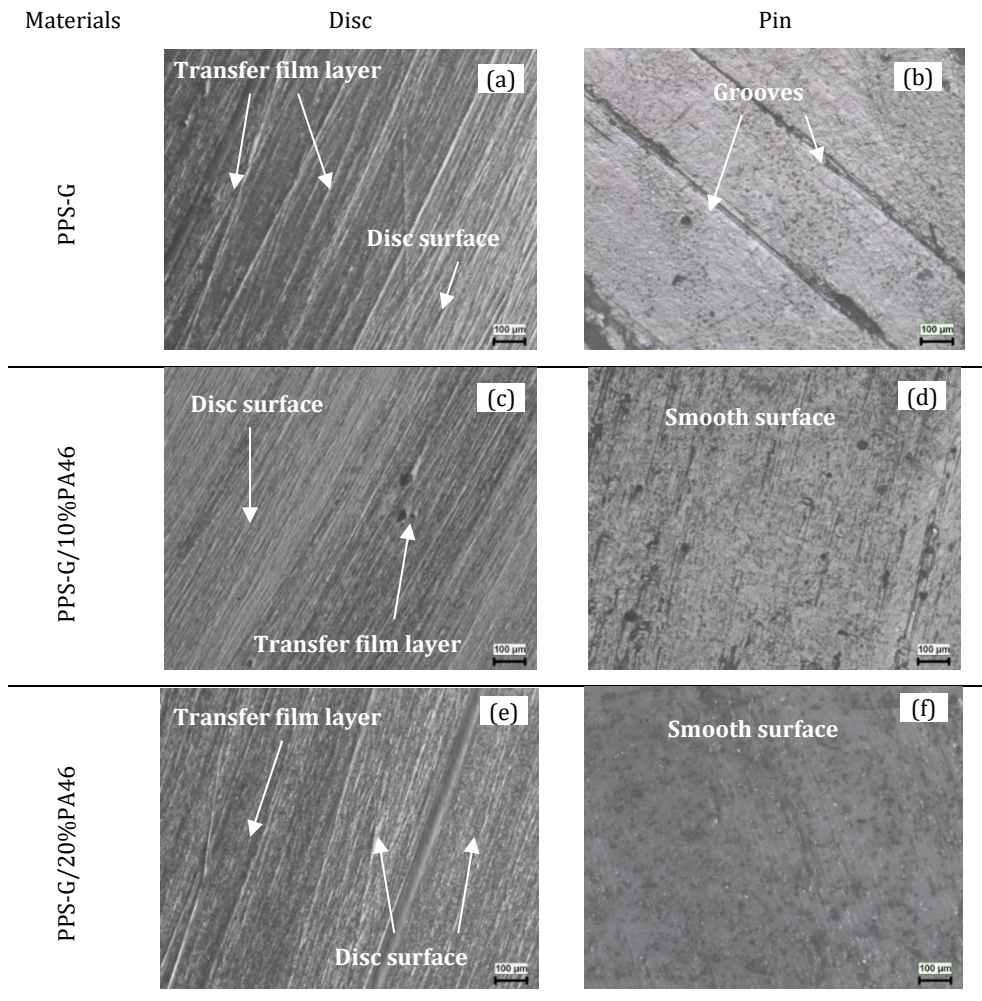


Fig. 6 Variation of specific wear rate with sliding speed for PPS-G, PPS-G/10%PA46, PPS-G/20%PA46, PPS-G/50%PA46 and PA46 polymers (Applied load: 90N).

The optical microscopy examination, as seen on Fig. 7 of the pin and disc surfaces of PPS-G, PA46 and their blends in dry conditions, at 60 N load and at 1.0 m/s sliding speed are given in Fig. 7. It is clear from the disc surface (in Fig. 7.a) that a good transfer film layer was formed for PPS-G polymer while the transfer film layer got worse with the increase of the content of PA46 (in Fig. 7.h). In the PPS-G polymer, the transfer film layer was effective on the entire surface, whereas in the PA46 added PPS-G blends; the transfer film layer was irregularly and locally shaped. This is thought to be due to the high specific wear rate of the PA46 polymer and increases the PPS-G blends specific wear rate with the addition increasing amount of PA46. For PA46 pin materials (in Fig. 7.j), the tested surface of the samples showed that the slip was occurred with wider and deeper grooves. However, these grooves were reduced in the PPS-G polymer due to the homogeneous transfer film layer. While a softer surface was obtained in the PPS-G/10%PA46 and PPS-G/20%PA46 blends, it was determined that numerous grooves were formed in the shear direction due to the increasing amount of PA46. The increased friction heat and deformed transfer film layer may deteriorate the tribological properties of PPS-G/PA46 blends. Consequently, the formation of the transfer film layer on the counter disc affected the wear and friction mechanism of PPS-G/PA46 blends.



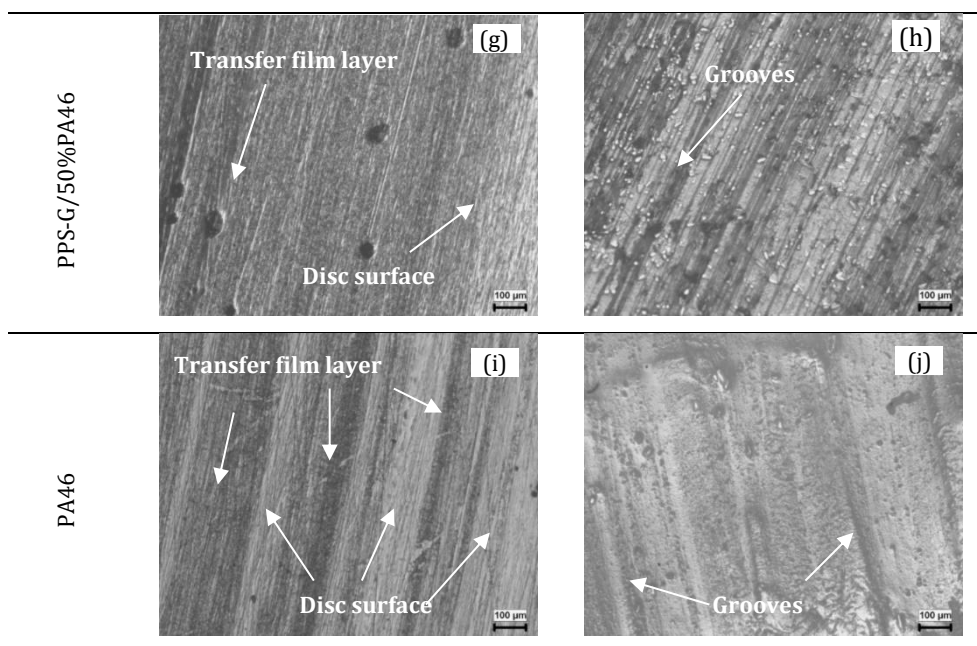


Fig. 7 Microscopy of pin-and disc surfaces of PPS-G, PA46 and their blends.

4. Conclusions

The tribological performance test of originally 40 wt.% fiber glass reinforced polyphenylene sulfide (PPS-G) and polyamide 46 (PA46) blends reveals the following conclusions:

The wear rates of PA46, PPS-G and their blends were in the order of 10^{-14} m²/N.

According to the applied load and sliding speed parameters, the friction coefficient values decrease while specific wear rates of PA46, PPS-G and their blends increase. Although the coefficient of friction is decrease, the high coefficient of friction of PA46 polymer and its negative effects on the PPS-G blends are clearly seen.

The highest specific wear rate was with a value of 4.37×10^{-14} m²/N for PA46 and the lowest wear rate was with a value 9.02×10^{-15} m²/N for PPS-G polymer. As the amount of PA46 increases, the specific wear rates of PPS-G blends also increase.

When the general tendencies investigated, changes in sliding speed had the greatest effect on friction coefficient and specific wear rate, that is, the biggest impact factor was the sliding speed.

All the coefficient of friction and specific wear results of the produced polymer blend varies between the values of neat PPS-G and PA46 materials according to the addition percentage.

The transfer film layer affects the wear and friction mechanism of PPS-G/PA46 blends.

Acknowledgements

This study was carried out with the contributions of Kütahya Dumlupınar University Scientific Research Projects Program. Project number: 2013/11.

References

- [1] Zhang M, Zeng H, He Y, Mai K. Effect of a polyaryletherketone-bearing bulky substituent on the non-isothermal crystallization kinetics of polyphenylene sulfide. *Thermochim Acta*, 1995; 257: 183 - 188. [https://doi.org/10.1016/0040-6031\(94\)02206-4](https://doi.org/10.1016/0040-6031(94)02206-4)
- [2] Choi J, Lim S, Kim J, Choe CR. Studies of an epoxy-compatible poly (phenylene sulfide)/polycarbonate blend. *Polymer*, 1997; 38: 4401 - 4406. [https://doi.org/10.1016/S0032-3861\(96\)01032-4](https://doi.org/10.1016/S0032-3861(96)01032-4)
- [3] Gopakumar TG, Ghadage RS, Ponrathnam S, Rajan CR, Fradet A. Poly (phenylene sulfide)/liquid crystalline polymer blends: 1. Non-isothermal crystallization kinetics. *Polymer*, 1997; 38: 2209 - 2214. [https://doi.org/10.1016/S0032-3861\(96\)00777-X](https://doi.org/10.1016/S0032-3861(96)00777-X)
- [4] Zhou S, Zhang Q, Wu C, Huang J. Effect of carbon fiber reinforcement on the mechanical and tribological properties of polyamide6/polyphenylene sulfide composites. *Material Design*, 2013; 44: 493 - 499. <https://doi.org/10.1016/j.matdes.2012.08.029>
- [5] Yang J, Xu T, Lu A, Zhang Q, Tan H, Fu Q. Preparation and properties of poly (polyphenylene sulfide)/multiwall carbon nanotube composites obtained by melt compounding. *Composite Science and Technology*, 2009; 69: 147 - 153. <https://doi.org/10.1016/j.compscitech.2008.08.030>
- [6] Schuster M, Araujo CCD, Atanasov V, Andersen HT, Kreuer KD, Maier J. Highly sulfonated poly (phenylene sulfone): preparation and stability issues. *Macromolecules*, 2009; 42: 3129 - 3137. <https://doi.org/10.1021/ma900333n>
- [7] Wang J, Li KX, He HW, Wang JL, Sun GH. Kinetic and thermodynamics analysis of water absorption in unidirectional fiber reinforced composites by polyethersulphone and polyphenylene sulfide. *Colloids Surfaces A*, 2011; 377: 330 - 335. <https://doi.org/10.1016/j.colsurfa.2011.01.009>
- [8] Zou H, Ning N, Su R, Zhang Q, Fu Q. Manipulating the phase morphology in PPS/PA66 blends using clay. *Journal of Applied Polymer Science*, 2007; 106: 2238 - 2250. <https://doi.org/10.1002/app.26880>
- [9] Ana M, Pascual D, Naffakh M. Towards the development of poly (phenylene sulphide) based nanocomposites with enhanced mechanical, electrical and tribological properties. *Material Chemistry and Physics*, 2012; 135: 348 - 357. <https://doi.org/10.1016/j.matchemphys.2012.04.057>
- [10] Ana M, Pascual D, Naffakh M. Enhancing the thermo mechanical behaviour of poly(phenylene sulphide) based composites via incorporation of covalently grafted carbon nanotubes. *Composites Part A-Applied Science*, 2013; 54: 10 - 19. <https://doi.org/10.1016/j.compositesa.2013.06.018>
- [11] Deng S, Cao L, Lin Z, Qiu W, Liang K, Li W. Nanodiamond as an efficient nucleating agent for polyphenylene sulfide. *Thermochim Acta*, 2014; 584: 51 - 57. <https://doi.org/10.1016/j.tca.2014.03.017>
- [12] Chen Z, Li T, Yang Y, Liu X, Lv R. Mechanical and tribological properties of PA/PPS blends. *Wear*, 2004; 257: 696 - 707. <https://doi.org/10.1016/j.wear.2004.03.013>
- [13] Cong P, Xiang F, Liu X, Li T. Effect of crystalline form on the tribological properties of PA46/HDPE polyblends. *Wear*, 2008; 265: 1106 - 1113. <https://doi.org/10.1016/j.wear.2008.03.005>
- [14] Scherge M, Kramlich J, Böttcher R, Hoppe T. Running-in due to material transfer of lubricated steel/PA46 (aliphatic polyamide) contacts. *Wear*, 2013, 301: 758 - 762. <https://doi.org/10.1016/j.wear.2012.11.035>
- [15] Elsner P, Eyerer P, Hirth T. *Polymer Engineering*, Berlin, VDI-Book Springer, 2008.
- [16] Wang Q, Zhang X, Pei X. Study on the synergistic effect of carbon fiber and graphite and nano particle on the friction and wear behavior of polyimide composites. *Material Design*, 2010; 31: 3761 - 3768. <https://doi.org/10.1016/j.matdes.2010.03.017>

- [17] Laigui W, Yang S, Liu W, Xue Q. An investigation of the friction and wear behaviors of polyphenylene sulfide filled with solid lubricants. *Polymer Engineering and Science*, 2000; 40: 1825 - 1832. <https://doi.org/10.1002/pen.11314>
- [18] Zhao Q, Bahadur S. The mechanism of filler action and the criterion of filler selection for reducing wear. *Wear*, 1999; 225: 660-668. [https://doi.org/10.1016/S0043-1648\(99\)00023-X](https://doi.org/10.1016/S0043-1648(99)00023-X)
- [19] Cho MH. The role of transfer film and back transfer behavior on the tribological performance of polyoxymethylene in sliding. *Journal of Mechanical Science and Technology*, 2009; 23: 2291-2298. <https://doi.org/10.1007/s12206-009-0354-z>
- [20] Cho MH, Bahadur S, Pogosian AK. Friction and wear studies using Taguchi method on polyphenylene sulfide filled with a complex mixture of MoS₂, Al₂O₃ and other compounds. *Wear*, 2005; 258: 1825 - 1835. <https://doi.org/10.1016/j.wear.2004.12.017>
- [21] Yu S, Hu H, Yin J. Effect of rubber on tribological behaviors of polyamide 66 under dry and water lubricated sliding. *Wear*, 2008; 265: 361 - 366. <https://doi.org/10.1016/j.wear.2007.11.006>
- [22] <https://www.eurotec-ep.com/daha-verimli-ve-akilli-arabalara-hazirlik/>
- [23] <https://www.pagev.org/pps>
- [24] <https://omnexus.specialchem.com/news/industry-news/polyplastics-pps-bump-off-molding-of-automotive-engine-cooling-system-000215941>
- [25] http://www.tpacomponents.com/uploads/pdf/en/0205_EN.pdf
- [26] Zhang XR, Pei XQ, Wang QH. Friction and wear studies of polyimide composites filled with short carbon fibers and graphite and micro SiO₂. *Material Design*, 2009; 30: 4414 - 4420. <https://doi.org/10.1016/j.matdes.2009.04.002>
- [27] Unal H, Mimaroglu A, Serdar V. Dry sliding performance of thermoplastics against reinforced unsaturated polyester (BMC): In use in electrical contact breakers components. *Wear*, 2006; 261: 841 - 847. <https://doi.org/10.1016/j.wear.2006.01.021>
- [28] Yamamoto Y, Hashimoto M. Friction and wear of water lubricated PEEK and PPS sliding contacts Part 2. Composites with carbon or glass fibre. *Wear*, 2004; 257: 181 - 189. <https://doi.org/10.1016/j.wear.2003.12.004>
- [29] Jiang Z, Gyurova LA, Schlarb AK, Friedrich K, Zhang Z. Study on friction and wear behavior of polyphenylene sulfide composites reinforced by short carbon fibers and sub-micro TiO₂ particles. *Composite Science and Technology*, 2008; 68: 734 - 742. <https://doi.org/10.1016/j.compscitech.2007.09.022>
- [30] Unal H, Sen U, Mimaroglu A. Dry sliding wear characteristics of some industrial polymers against steel counterface. *Tribologie Int.* 2004; 37: 727 - 732. <https://doi.org/10.1016/j.triboint.2004.03.002>



Technical Note

Applicability investigation of alumina-titania based plasma spray coating on cast iron brake discs for battery electric vehicles

Ekrem Altuncu ^{*1,a}, Recep Akyüz ^{2,b}

¹ Sakarya App. Sci. Uni., Sakarya, Turkey.

² TOFAŞ Turkish Automotive Company R&D Center, Bursa, Turkey

Article Info

Article history:

Received 10 Nov 2019

Revised 24 Dec 2019

Accepted 29 Jan 2020

Keywords:

Plasma spray;

Ceramic coating;

Wear;

Brake Discs.

Abstract

Automobile brake disc are subjected to cyclic thermal, mechanical and corrosive effects. In general, gray cast iron grades are preferred as disc brake materials. Lamellar cast iron disc brakes have a limited lifetime and are replaced periodically during the maintenance-service process. With the growing interest in the number of Battery Electric Vehicles (BEV), there is a need for disc brake with longer service life on discs. Therefore, in the automotive sector, in line with increasing competition and user demands, there is an interest in new coating types and materials with corrosion free properties, a longer service life and high brake performance. Wear and corrosion resistant plasma spray coatings are the key to increasing the service life and braking performance of cast iron discs. In this study, the discs (GG20) are coated with Alumina- Titania based ceramic material by atmospheric plasma spray method. The ceramic coated disc brakes were installed on the road driving test vehicle and disc brake thickness reduction were measured periodically according to wear test plan throughout 20.000 km. The test results show that the ceramic coating provides 18 times more wear resistance compared to uncoated disc brake. In addition, coated disc brakes exhibited superior performance in corrosion tests. As a result of the investigations carried out on disc brakes, it is understood that plasma spray ceramic coatings can be used alternatively in brake disc systems.

© 2020 MIM Research Group. All rights reserved.

1. Introduction

The basic principle of the automobile braking system is to convert the kinetic energy of the vehicle into thermal energy as output of brakeage. To stop the vehicle, friction is created between two mechanical components (brake disc-pad), giving rise to heat generated between those two components and reduction in kinetic energy of vehicle which decreases vehicle velocity [1-3]. Due to the increase temperature in the interface of disc brakes and pads, high melting point materials are preferred. The brake discs must resist the atmospheric conditions and have the appropriate thermal properties. Cast iron materials have both technical and economic use potentials for brake discs. Grey cast iron (GG15-25) disc brake (rotor) and pad (friction materials) couples are one of the critical safety components in motor vehicles. High friction forces are formed from the moment the disc brake comes into contact with the brake pads. In variable road conditions, friction forces turn into heat in a short time. Therefore, the disc brake is exposed to both

*Corresponding author: altuncu@subu.edu.tr

^a orcid.org/0000-0002-1395-9013; ^b orcid.org/0000-0003-3310-6437;

<http://dx.doi.org/10.17515/resm2019.161ma1110>

high mechanical stresses and thermal loads. Wet corrosion is also generated depending on the atmospheric road conditions on the discs. Factors such as rain, snow, salt and other road sprays can cause in corrosion on disc surfaces. That means, exposed parts, such as disc brakes can quickly become rusty, which is not satisfied for aesthetical expectations. In severe driving conditions, braking may cause the temperature on the disc brake-pad interface to rise up to 800 °C. At such a temperature, polymeric compounds of pad are disrupted, coefficient of friction (CoF) decreases between pad and disc brake, and the rate of counter wear increases exponentially [4,5,6]. In the new generation of brake system designs (regenerative brake systems), the interest in coated disc brake has increased to improve the disc brake service life and braking performance. Thermal spray coating methods are an effective surface engineering solution to improve the performance of disc brakes [7-11]. Coated with high velocity oxy fuel (HVOF) spray method, cermet (metal-carbide) based disc brakes are high-cost applications in luxury vehicles. Alumina - Titania based ceramics can be used for coating machinery components where very dense and smooth deposits with high wear resistance are required under corrosive media [9-10]. In this study, it is aimed to investigate the applicability of plasma spray coatings on automobile discs in detail. In this direction Alumina-Titania based coatings were deposited on the gray cast iron discs by plasma spray process, and the brake performance and salt spray corrosion performance were evaluated.

2. Experimental Procedures: Materials and Methods

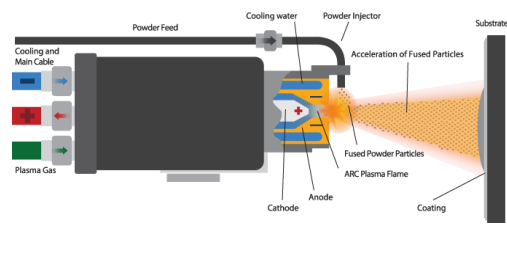
Grey cast iron (GG20/ EN-GJL-200) brake discs have been used in these experimental studies. Plasma spray coating method was preferred because of its superiority over other coating and heat treatment methods. Plasma spraying is a coating process in which powders of the coating materials are fed into the plasma jet at around 10000K. Any material with the capability of melting without experiencing decomposition is suitable for thermal spraying. Plasma spraying has been successfully applied in numerous fields, such as corrosion and oxidation resistance, high-temperature protection, wear and erosion resistant coatings. The high cost efficiency and good quality of the coatings obtained by using APS have led to a successful implementation in automotive industry. The coating operation generally has three stages. These are surface preparation before coating, coating process and post-coating processes. Surface preparation is the most critical step in a plasma spraying operations. Coating adhesion quality is directly related to the cleanliness and roughness of the substrate surface, especially when spraying onto preheated metal surface. The brake discs were sandblasted and cleaned from any oxide and grease with acetone. Grit blasting was carried out with a highly efficient sand blaster with alumina grit size of 10-20 mesh, a sand blaster with a 10 mm nozzle, operating at a blasting pressure of >0.5 MPa. The distance between the substrate and nozzle was 120 mm at a 90° angle. The grit blasting is used prior to depositing in order to improve coating adhesion to substrate. The mechanical adhesion of the plasma spray coating depends mainly on substrate surface morphology and cohesion between the deposited particles. When the heated particles are accelerated towards the substrate, they flatten upon impact in a disc shape splats, followed by rapid cooling and mechanical anchorage to the irregularities of the surface.

In this study, two layered coating was produced onto brake disc using atmospheric plasma spray (APS) system with F4MB spray gun equipment (Fig 1.). Firstly, NiCr (Ni+wt.%20Cr) based bond layer (BC) was coated on grit blasted disc surface through atmospheric plasma spray (APS) process and then Al₂O₃-TiO₂ (Al₂O₃-wt%10-13 TiO₂) based ceramic top layer (TC) was deposited by APS (Fig 1b). Spray deposition parameters

are presented in Table 1. Microstructural characterization was carried out with scanning electron microscopy (SEM-EDX). Vickers microhardness ($HV_{0,3}$) tests were performed on polished surfaces of the ceramic coatings with a 300gr normal load and a dwell time of 15 s. The surface roughness was measured with the profilometer.

In order to determine the resistance of the coated disc brake to atmospheric corrosion conditions, salt spray test was performed and then the disc brake surface was visually examined. Corrosion test was carried out in accordance with ASTM B117 (ISO-9227) standard. Brake disc friction performance tests were carried out with dynamometer test in accordance with the OEM specifications in different temperature and braking regimes. The total thickness change and disc thickness variation (DTV) was monitored over 20,000 km.

Table 1. Plasma spraying process and spray parameters

 <p>Schematic plasma spray gun</p>	Process	APS	
	Spray Gun	F4-MB	
Layer	BC	TC	
Current, Ampere	550	550-600	
Plasma Gases	Ar /H2		
Gas flow rates n/lpm	40/8	40-50/6-12	
Spray Dist. mm	100	90-125	
Feed Rate gr/min.	30	25-40	

The plasma sprayed ceramic based surface of the brake disc (brake disc thickness: 26 mm) is presented in the Fig.1. After coating deposition, the coated surface is machined, and the surface roughness (R_a) is measured 0.8 μm .



a) Before coating

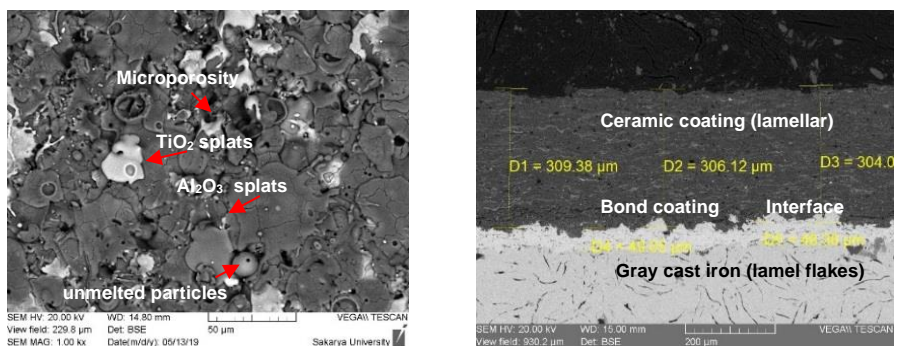
b) After coating

Fig. 1 Brake discs photographs before and after plasma spraying

3. Experimental Results and Discussions

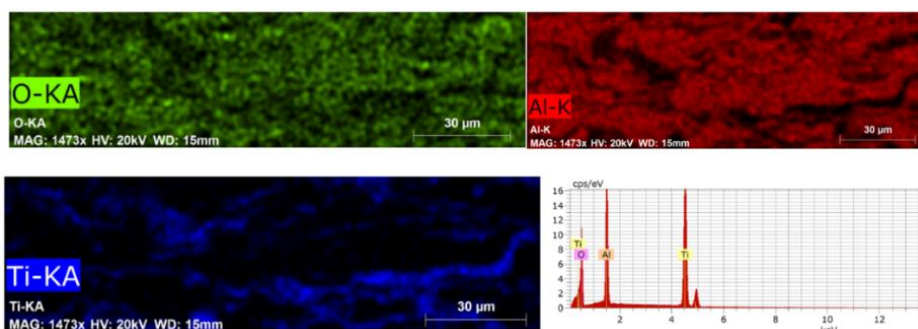
During the plasma spray coating formation, splat layers of impacted and accelerated particles are formed on top of the previously molten particles which spread and flatten

on the disc surface. The process continues with an increasing number of spray passes. Spray pass number determine the coating layer thickness. The quality of plasma-sprayed coating depends on the substrate/coating interface adhesion strength and the cohesion of buildup layers. By optimizing the spray parameters, mechanical properties and microstructure can be controlled. Technically, optimum spray distance is important to ensure good adherence of coating. Too short spraying distance will produce lower adherence due to overheating and resulting internal stress inside the coating. In contrast, too long spraying distance will decrease the adherence bonding due to cooling and deceleration of the particles flying in the plasma jet. In ensuring homogenous and less porosity ceramic coating layers, the plasma current also should be increased to ensure the powders is melted properly when the powder flow rate was increased. Spray parameters are optimized by experimental design (plasma current 580A, Ar/ H₂:44/8 gas flow rates, 115mm spray distance, feedstock rate 32 gr/min.). Microstructure of the plasma spray coating cross section investigations were carried out after standard metallographic sample preparations. After precise sectioning without damaging the coating structure, cold mounting, grinding (200-400-800-1000 mesh for 4 min., water coolant) and polishing (9-6-3 μ m diamond paste for 2 min.) steps were completed respectively. When the microstructure of the top surface (Fig 2a) is examined by scanning electron microscope (SEM), two different colored structures are seen. In the EDX analysis (Fig. 2c), it was found that the light-colored structure (TiO₂ rich phase) included Ti, O elements, dark structure (Al₂O₃ rich phase) has Al, and O elements. It can be seen that the splats on the surface of the coating is well formed. The morphology of the splat is very important in the coating layer. Homogeneous and well-spread splat formation reduces porosity and increases adhesion strength. As can be seen from the Figure 2a, the desired coating properties could be achieved with optimized parameters. SEM micrographs of the cross section of coatings showed a lamellar layered structure. Typically, unmelted or semi-melted particles, small sized micro cracks and low porosity is observed in the coating structure. It can be clearly seen that the lamellars adhere very well (Fig 2b). Coating thicknesses were measured in cross - sectional examinations. NiCr based bond coat layer in thickness range 30-50 μ m, Alumina- Titania based top coat layer in thickness 340 \pm 25 μ m (in Fig 2b). As can be seen, the desired coating thickness can be achieved. In general, the coating layer thickness is not desired to be too high. Increased coating thickness increases internal stresses and may cause the delamination. The structural properties and discontinuities of the coating control the mechanical properties of the coating. Microhardness and adhesion strength are the most important mechanical properties of the coatings. The average micro hardness of the top coating is 900 \pm 15 HV_{0.3}, 255 \pm 20 HV_{0.3} for bond coating and the gray cast iron is 240 \pm 15 HV_{0.3}. Improper coating process parameters may result in fluctuations in hardness values. This has a negative effect on the wear performance of the coated disc. The hardness of the coating is directly related to the wear resistance. Increased hardness reduces wear loss. The ceramic coating obtained by plasma spray process contributed to increase the surface resistance and wear resistance of cast iron disc.



a)top surface

b)cross section



c) EDX mapping analysis of the coating

Fig. 2 SEM images and EDX analysis of coating

The wear performance of the brake disc was monitored by 20.000 km intervals on the vehicle and the thickness changes were measured periodically (Fig. 3). The coated disc surface becomes metallic appearance after friction losses over time. Numerous brakes of varying intensity have been applied over 20.000 km. Even after 20.000 km, the coating is still on the disc surface. When disc surface was examined, no delamination or cracking was observed on the coating. It is understood that the coating provides sufficient adhesion strength and heat resistance. Under the test conditions the coating has heat resistant and corrosive. There is no distortion and deformation on the disk.

During the test, disc thickness measurements were taken each of 5000 km and the driver's reports on the brake performance were evaluated. It should be noted that the braking efficiency and disc brake-pad compatibility is very critical. In this respect, DTV (Disc Thickness Variation) measurements should be evaluated. When the thickness variation of the disc brake exceeds 20 μm, the pads oscillate back and forth causing a pulsation in the hydraulic circuit back to the brake pedal. This brake pad osculation also causes a variation in brake torque as the brake pads grab and release over the higher portion of the disc brake thickness. It is typically noticed in the steering wheel as the brake torque from the left and right axles is different and out of sequence.



Fig. 3. On vehicle test: plasma spray coated disc images and measurement method

The wear test results and thickness loss of the coated and uncoated disc brakes were compared to the thickness change on different four points of brake disc surfaces. Brake disc runout and DTV (Disk Thickness Variation) are important measurements in understanding braking performance and disc wear life. Disc runout and DTV can give valuable insights into how brakes are performing and can be used to diagnose faults and even design issues. Brake disc thickness variation (DTV) causes uneven wear on brake discs, brake disc -shaped automotive parts that are squeezed between brake pads to slow or stop a vehicle's wheels. When a disc brake has areas of different thickness, the amount of clamping force that's applied across the disc brake's surface varies. These differences in clamping force lead to differentiation in torque which may cause brake juddering, pulsating or vibration. DTV test is one of the most important performance criteria for brake discs. Table 2. shows the total thickness change of the disc in the service life test. Measurements made from 4 different points do not show a significant change in brake disc (left or right side) thickness. When ceramic coated disc compared with uncoated cast iron disc, it has approximately 18 times longer service life in terms of minimum thickness criteria.

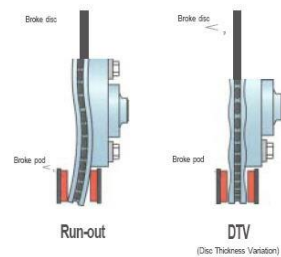
Table 2. Coated brake disc thickness change measurements in service life test

Vehicle mileage (km)	Right brake disc thickness (mm)				Left brake disc thickness (mm)			
	Point 1	Point 2	Point 3	Point 4	Point 1	Point 2	Point 3	Point 4
0	26,45	26,46	26,46	26,45	26,5	26,5	26,5	26,49
300	26,44	26,45	26,45	26,45	26,5	26,5	26,5	26,49
500	26,45	26,46	26,45	26,45	26,5	26,5	26,5	26,48
1600	26,45	26,46	26,46	26,45	26,5	26,5	26,5	26,49
5000	26,45	26,44	26,45	26,45	26,5	26,51	26,5	26,49
7500	26,44	26,45	26,45	26,44	26,49	26,51	26,5	26,49
10000	26,44	26,45	26,44	26,44	26,49	26,49	26,49	26,49
15000	26,425	26,43	26,44	26,43	26,48	26,49	26,49	26,48
20000	26,425	26,43	26,43	26,425	26,48	26,48	26,48	26,475
Total thickness change	-0,015	-0,03	-0,03	-0,025	-0,02	-0,020	-0,020	-0,015

Table 3. presents DTV and runout generation test results. The measurements were done by signified three circles. Also, it is observed that, runout values improved according to starting condition on braking surface.

Table 3. DTV and runout comparison in ceramic coated and uncoated discs

Ceramic coated disc		DTV (µm)			Runout (µm)
Right	0 km	17	21	29	55,5
	20000 km	8	10	19	35
Left	0 km	16	20	21	20
	20000 km	8	8	9	20,5
Uncoated disc		DTV (µm)			Runout (µm)
Right	0 km	1,6	3,5	2,9 3	8,80
	20000 km	21	31	25, 7	32
Left	0 km	2,9	2	2,8	11
	20000 km	24,3	27	41, 5	37,7



Another important control parameter regarded with customer cycle is vibration occurrence in the on-road test. The vibration occurrence was not observed during on-

road tests both with coated and uncoated disc brake. During execution of test, original friction material (pad) has been used. The pad surface was deformed, and binding elements were burnt because of the undissipated heat between pads and disc brake (Fig 4). Besides, occurrence of amorphous (glassy) structure was observed on the interface of disc brake and pad because of coming out high and undissipated heat. In this case, the requirement for the development of specific friction material for coated disc brake has emerged.



Fig. 4 Disc and pad surface photographs after vehicle road test

Salt spray test. The salt spray (or called as salt fog) test is a standardized and popular corrosion test method, used to check corrosion resistance of materials and surface coatings. The appearance of corrosion products (red rust or other oxides) is evaluated after a pre-determined period. In order to determine corrosion resistance, the disc brakes were tested in a salt spray (in %5 NaCl solution) cupboard and checked red rust occurrence periodically. Coated disc brakes exhibited superior performance in salt spray corrosion tests (Fig 5). No red corrosion was observed on the coating surface after 720 hours. Uncoated discs can withstand up to 48 hours under corrosive media and red rust (heavy corrosion products) are observed.



Fig. 5 Coated disc brake surface after salt spray corrosion test

4. General Conclusions

In experimental studies, Alumina-Titania (Al_2O_3 -wt%10-13TiO₂) coatings can be deposited successfully on cast iron disc brake surface with an intermediate bond coat of Ni20Cr by optimized atmospheric plasma spray parameters. The plasma spray gun parameters such as powder flow rate, plasma gases flow rate, plasma current, and stand-off-distance has directly influenced the mechanical properties and structure of the coating. After many experimental trials for coating optimization, coatings with suitable properties and thickness were obtained. The plasma spray coating structure can be controlled with effective process parameters. The reproducibility of the coatings is very

high and for mass production potential is very convenient. The validation testing process required for automobile disc applications has long and very strict requirements due to reliability. Alumina–Titania coated discs have tested on vehicles and passed all the brake pre-performance tests successfully. Dynamometry tests, even at high temperatures, the coefficient of friction is within a reliable range. The dynamometer tests showed good stability in CoF of the coated disc (0.39) compared with the uncoated disc (0.42). Results of on-road service life test on coated discs show superior performance compared to uncoated ones. Coated discs exhibited high performance (above 720 hr.) in salt spray corrosion tests. Salt spray test results showed negligible weight loss in case of plasma coating systems. Also, ceramic coated disc brakes were exhibited preferable performance in terms of DTV and runout occurrence in road test. Plasma spray process (APS) offers high coating quality and wear performance for brake discs. Coated disc displayed a significantly reduced weight loss than the uncoated disc with the pad wear remaining largely unchanged, as shown in Figure 6. It is understood that plasma spray ceramic coatings can be used effectively in automotive disc brake systems.

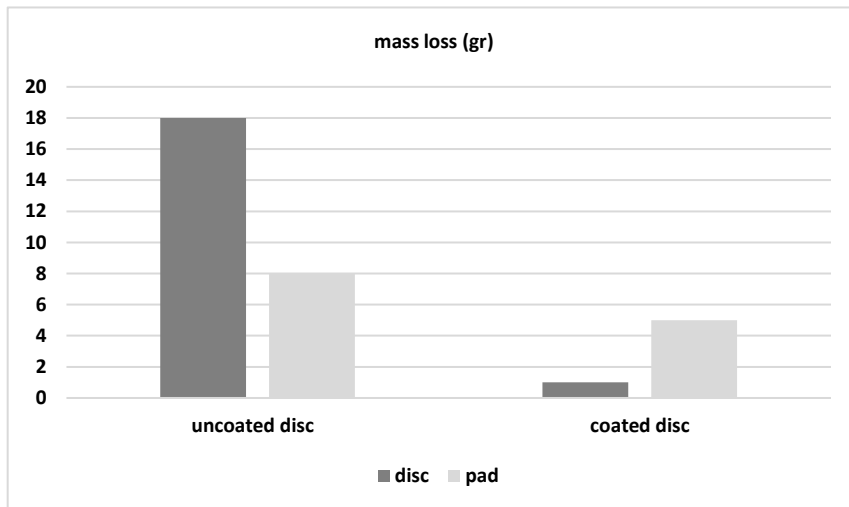


Fig. 6 Comparative mass loss of APS Al₂O₃-TiO₂ coated and uncoated brake discs and corresponding pad mass loss

Acknowledgement

The authors acknowledge that this study is financially supported by TOFAŞ Turkish Automotive Company. The authors would like to thank Zekeriya Kolbasar (Sakarya Uni. Applied of Sciences) and Ömer Demirkurt, Suna Aksel Atıhan (DEKA), Ozan Demirdalmış (Kale balata) for their contribution to the experimental work.

References

- [1] Pourmovahed A. *International Journal of Vehicle Design*, 1991,12(4), 378-403
- [2] Deshpande S, Kamat A, Dalvi R, Deshpande Y. Review on Thermal Cracking Phenomenon in Brake Disc, *International Journal of Engineering Research & Technology (IJERT)*, 2017; 6:6 233 - 236. <https://doi.org/10.17577/IJERTV6IS060119>
- [3] Rajput RK. *A Textbook of Automobile Engineering*, Laxmi publications, 2014; 559 - 588.

- [4] Demir A, Samur R, Kılıçaslan I. Investigation of The Coatings Applied onto Brake Discs On Disc-Brake Pad Pair, *Metalurgija*, 2009; 48:3 161 - 166.
- [5] Blau PJ, Jolly BC, Qu J, Peter WH, Blue CA. Tribological Investigation of Titanium-Based Materials for Brakes, *Wear*, 2007; 263: 1202 - 1211. <https://doi.org/10.1016/j.wear.2006.12.015>
- [6] Herman H. *Thermal Spray Coatings, Metallurgical and Ceramic Protective Coatings*, Chapman & Hall, London England, 1996. https://doi.org/10.1007/978-94-009-1501-5_10
- [7] Kim SJ, Cho MH, Cho KH, Jang H. The role of raw material ingredients of brake linings on the formation of transfer film and friction characteristics, *Tribology International*, 2007; 40: 15 - 20.
- [8] Wang Y, Jiang S, Wang M, Wang S, Xiao TD, Strutt PR. Abrasive wear characteristics of plasma sprayed nanostructured alumina-titania coatings, *Wear*, 200; 237: 176 - 185. [https://doi.org/10.1016/S0043-1648\(99\)00323-3](https://doi.org/10.1016/S0043-1648(99)00323-3)
- [9] Normand B, Fervela V, Coddeta C, Nikitine V. Tribological properties of plasma sprayed alumina-titania coatings: role and control of the microstructure, *Surface and Coatings Technology*, 2000; 123:2 - 3 278 - 287. [https://doi.org/10.1016/S0257-8972\(99\)00532-0](https://doi.org/10.1016/S0257-8972(99)00532-0)
- [10] Trache R, Berger LM, Leyens C. Comparison of Alumina-Titania Coatings Deposited by Plasma and HVOF Spray Techniques, *Int. Thermal Spray Conference*, Barcelona, Spain, May, 2014.
- [11] Odhiambo JG, Li W, Zhao YT, Li CL. Porosity and Its Significance in Plasma-Sprayed Coatings, *Coatings*, 2019; 9:460 1- 19. <https://doi.org/10.3390/coatings9070460>



Research on Engineering Structures & Materials

In This Issue

Research Article

197

Melik Ziya Yakut, Sinem Esen

Impact of energy efficient design parameters on energy consumption in hot-humid climate zones

Research Article

207

Adeshina Adegoke, Akin Fashanu, Olayinka Adewumi, Ayowole Oyediran

Nonlinear vibrations of a cantilevered pipe conveying pulsating two phase flow

Research Article

229

Hayri Baytan Ozmen, Mehmet Inel, Yunus Demirtas

Evaluation of different cases of soft story formation for mid-rise RC buildings

Research Article

241

Behçet Dünder, Emriye Çınar, Ahmet Necip Çalışkan

An investigation of high temperature effect on pumice aggregate light mortars with brick flour

Research Article

257

Fatoş Koç, Selay Sert Çok, Nilay Gizli

Tuning the properties of silica aerogels through pH controlled sol-gel processes

Research Article

271

Ferhat Yıldırım, Mustafa Aydın, Hakan Yetgin

Tribological properties of PPS/PA46 polymer blends

Technical Note

283

Ekrem Altuncu, Recep Akyüz

Applicability investigation of alumina-titania based plasma spray coating on cast iron brake discs for battery electric vehicles

C
O
N
T
E
N
T



Research on
Engineering
Structures & Materials

